学位論文

A study of temporal and spatial structure of edge turbulence in the TST-2 spherical tokamak

(TST-2球状トカマク装置における周辺部乱流の時空間構造の研究)

平成27年12月博士(理学) 申請

東京大学大学院理学系研究科

物理学専攻

曽根原 正晃

Doctor Thesis

A study of temporal and spatial structure of edge turbulence in the TST-2 spherical tokamak

Graduate School of Science

The University of Tokyo

Masateru Sonehara

December 24, 2015

Abstract

In fusion plasma research, the study of anomalous transport induced by plasma turbulence is important for achieving fusion relevant high temperature and high density plasmas. In magnetically confined plasmas, various types of fluctuations are induced due to plasma instabilities. These fluctuations cause anomalous transport flux, and the plasma confinement is deteriorated as a result. In conventional tokamak plasmas, these transports are thought to be caused mainly by drift waves driven by pressure and temperature gradients, and the contribution of magnetic fluctuations is believed to be negligible. A spherical tokamak (ST) can confine high pressure plasma with a relatively weak magnetic field strength and is very attractive as a fusion reactor from an economic point of view. However, magnetic fluctuations could be large in ST plasmas, where the high pressure, the weak magnetic field strength (i.e. the low safety factor) and the large plasma current may enhance magnetic fluctuations through instabilities. At the edge region, we should also consider the effect of resistivities due to a relatively low temperature. When the magnetic fluctuations are strong, the field lines become stochastic and the transport along the field lines deteriorates the confinement. In addition, such stochastic field would affect the other intrinsic instabilities. Therefore, understanding not only the drift wave like fluctuations but also the magnetic fluctuations and their effects on plasma turbulence is important.

In this thesis, the temporal and spatial structures of the edge turbulence in TST-2 ST plasmas are measured by using Langmuir probes and magnetic pickup coils. TST-2 has a short inter-discharge time, which is necessary to obtain a large number of data sets and to perform ensemble averaging in order to reveal the structure of the plasma turbulence and higher order non-linear processes associated with the plasma turbulence.

It was found that the observed fluctuations can be classified into two types: (i) the MHD type fluctuation characterized by a global structure and low frequencies (< 20 kHz), and (ii) the drift wave like fluctuations characterized by a smaller spatial scale and higher frequencies (> 20 kHz). The discharges in TST-2 are characterized by a large MHD type fluctuation. The relative fluctuation level is $\tilde{B}_r/B_T = 10^{-2}$ inside the last closed flux surface (LCFS), and the level is much higher than those in conventional tokamaks. It should be noted that the phase difference between $\tilde{B}_r$, $\tilde{n}_e$ and $\tilde{T}_e$ indicates that the magnetic fluctuations are dominated by an ideal MHD mode. Since ideal MHD modes do not induce transport, the other modes play important role in the frequency range < 20 kHz. The parallel wavenumber $k_\parallel$ of the MHD type fluctuation is less than 0.0001 mm^{-1}, while the perpendicular wavenumber is $k_\perp = -0.004$ mm^{-1}. $k_\perp$ at 20 - 100 kHz shows a constant phase velocity of about 4000 m/s in the electron diamagnetic drift direction inside the LCFS. These two different types of turbulence in wavenumber spectrum have not been observed in conventional tokamaks.

The electrostatic particle flux is dominated by the MHD fluctuation component. However, the fluctuation in the frequency range < 20 kHz is mainly an ideal MHD mode, and it does not induce transport. This fact suggests that resistive modes and/or other non-MHD modes which induce transport are mixed with the ideal MHD mode. The total flux is $\Gamma_r = 5 \times 10^{20}$ m^{-2}s^{-1}. The estimated radial diffusion coefficient is $D_r = 10$ m^{2}s^{-1}. This value is comparable to D_{Bohm}, which is a theoretical reference value for turbulent lossy plasma. The correlation length of the MHD fluctuation along a field line is about 5 m, and the Rechester-Rosenbluth type diffusion coefficient is estimated as $D_{st} = 10$ m^{2}s^{-1}. While the effect of magnetic fluctuations to plasma transport has been considered to be negligible in conventional tokamaks, the estimated diffusion coefficient suggests that the effect of magnetic fluctuations can be significant in ST plasmas. Note that the estimated coefficient probably represents the upper limit, since the correlation length of the MHD fluctuations is long and resultant magnetic field structure may not be so stochastic.

The high coherence of floating potential fluctuations $\tilde{V}_f$s along the field line up to 100 kHz leads to the possibility that the fluctuations are frozen to the magnetic field line and oscillate with the MHD fluctuation. In order to clarify the possibility, the spatial structure of fluctuations is reconstructed by tracing the trajectory of the field lines. The profile of the coherence at 50 kHz shows decay lengths of $\delta R = 30$ mm and $\delta Z = 12$ mm. The inverses of these values agree roughly with the local wavenumber spectral width $\sigma_k = 0.05$ mm^{-1}. This agreement implies that the fluctuations are frozen to a field line. While these measurements and analysis revealed the structure perpendicular to the field lines, we also obtained parallel structure, which is characterized by parallel wavenumbers and parallel correlation lengths. The parallel correlation lengths $l_\parallel$s of both MHD ($l_\parallel \sim 2$ m) and drift wave fluctuations ($l_\parallel \sim 1$ m) are shorter than the connection length $L_C \sim 10$ m, which represents the effective system size along the parallel direction. The relationship between these lengths implies that we

should consider the parallel structure in addition to the perpendicular structure. As a result, the 3D nature of the turbulence should be studied both experimentally and theoretically for understanding the anomalous transport driven by turbulence.

Two dimensional turbulence measurements revealed that the radial profiles of the fluctuations in TST-2 are also different from those in conventional tokamaks. In conventional tokamaks, potential fluctuation $e\tilde{V}_p/k_B T_e$ has a peak just inside the LCFS, while that in TST-2 increases monotonically with the radius at the edge. In contrast, $\tilde{V}_f$ of 20-150 kHz has a peak around the LCFS, which is similar to the profile in conventional tokamaks.

The Langmuir probe at the high field side (HFS) showed that $\tilde{V}_f$ is one order of magnitude smaller than that at the low field side (LFS), and their coherence is less than 0.2, suggesting that the long connection length between the HFS and the LFS leads to the poor coherence.

In summary, we have experimentally revealed the detailed temporal and spatial structure of the edge turbulence in ST plasmas for the first time. In the time domain, the turbulence can be classified into slow MHD fluctuations and fast drift wave type fluctuations. The former has large amplitudes and its effect on transport is significant. In the perpendicular directions, the drift wave type fluctuations are frozen to the slow MHD fluctuations. The structures in the parallel direction (i.e. the parallel wavenumber and the parallel correlation length) were measured for the first time inside the LCFS in tokamaks. The revealed structures imply that the turbulence in STs are complicated and we should take into account the 3D effect in future ST research. Several differences between conventional tokamak plasmas and the TST-2 plasmas are found in the features of turbulence, and the differences seem to be related to the large MHD fluctuations. Because its effect on transport is significant, further research is required to design an ST fusion reactor, where the suppression of turbulence induced transport is inevitable.

Contents

List of Figures

List of Tables

Chapter 1

Introduction

1.1 Plasmas

As the temperature of a material increases, its state changes from solid to liquid, and to gas. If the temperature is raised further, the atoms of gas are ionized, that is, they are separated into electrons with negative charges and ions with positive charges. These freely moving charged particles interact through Coulomb force, and form a high temperature gaseous matter, in which the charge densities of ions and electrons are almost the same and charge neutrality is sustained in macroscopic scale. This state is called plasma [1]. Coulomb force is long range force, which means the force decays only in inverse square of the distance between the charged particles. When the charged particles move collectively, they create current flow and interact through Lorentz force due to the generated magnetic field. Thus, many charged particles interact with each other by the long range forces and various collective phenomena occur. The typical examples are various kinds of instabilities and waves.

When the temperature of the plasma is T[K], the average velocity of the particles can be defined by

$$mv_T^2/2 = k_B T/2\,, \tag{1.1.1}$$

where k_B is the Boltzmann constant $k_B = 1.380658(12) \times 10^{-23}$ J/K. A more commonly used unit of energy is one electron volt [eV], which is the energy necessary to move an electron, whose charge is $e = 1.60217733(49) \times 10^{-19}$ C, against a potential difference of 1V.

$$1 \text{ eV} = 1.60217733(49) \times 10^{-19} \text{J}, \tag{1.1.2}$$

which corresponds to the thermal energy of 1.16×10^4K.

One of the fundamental properties of plasma is the shielding of the external electric potential, called Debye shielding. When positive or negative potential is externally applied, the potential attracts (or repulses) electrons and thus the attracted electrons compensate for the electric disturbance. The potential disturbance decays with the characteristic length called Debye length. The Debye length λ_D can be derived from Poisson's equation and is defined as

$$\lambda_D = \sqrt{\frac{\epsilon_0 k_B T_e}{e^2 n_e}}\,, \tag{1.1.3}$$

where ϵ_0 is the permittivity of free space $\epsilon_0 = 8.85 \times 10^{-12}$ F/m. Furthermore, plasma has a characteristic frequency, which is called plasma frequency,

$$\omega_{\text{pe}} = \sqrt{\frac{ne^2}{m\epsilon}}\,. \tag{1.1.4}$$

When plasma loses its electric neutrality an electrostatic field is generated, and the electrons start to move to preserve the neutrality. The time scale of this phenomenon is $1/\omega_{\text{pe}}$.

1.2 Nuclear fusion

Energy production at present depends on natural resources such as fossil fuels, hydroelectric generation, nuclear fuels, and sunlight. Especially, fossil fuels are our primary energy resources. However, these are not only the limited reserves, but they emit greenhouse gases when combusted. Currently, solar energy and other renewable energies do not provide sufficient electricity to sustain our current lifestyle, and it is unlikely that they will be the ultimate solution for the world's energy problem from some fundamental reasons. Nuclear fission can be an alternative option in the view of CO_2 and other harmful emissions. However, as we can see from the accident in Fukushima, a nuclear power plant can cause deadly disasters. Even if not so extreme, it releases radioactive nuclear waste and affects the nature for tens of thousands years.

Nuclear fusion can be an ultimate solution for these various problems. Fusion denotes merging of light atoms: mainly hydrogen (H) and its isotopes deuterium (D) and tritium (T). The fusion of hydrogen is the main reaction that powers the sun. Deuterium can be extracted from ocean water and tritium is obtained by breeding with lithium isotopes Li^6 included in the fusion blanket. The nuclear fusion reaction can be written as follows (Fig. 1.2.1).

$$D + T \rightarrow n\,(14.06\text{MeV}) + {}^4\text{He}\,(3.52\text{MeV}). \tag{1.2.1}$$
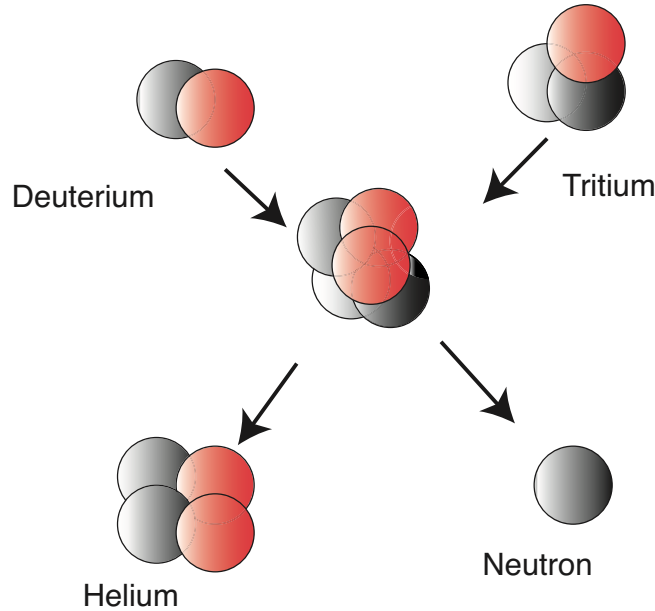
Figure 1.2.1: Diagram of D-T reaction.

Both deuterium and tritium have positive charges, and they repel each other due to the Coulomb force. In order to overcome the Coulomb barrier and attain the fusion, the reaction requires a temperature of more than 10 keV, hotter than the center of the sun. Since there is no solid material to confine this high temperature plasma, a method to isolate the plasma from the material wall is required.

1.3 Tokamak

In this section, we introduce a tokamak, which is one of the most promising confinement schemes for nuclear fusion. In order to achieve a reacting situation and economic feasibility, it is necessary to confine high temperature plasma for a certain period. A well known confining method is the use of strong magnetic field. Plasma is composed of charged particles, and is affected by Lorentz force under the presence of a magnetic field. With Lorentz force $q\boldsymbol{v} \times \boldsymbol{B}$, a charged particle has a nature to circulate around a magnetic field line called Larmor motion.

A tokamak is a device to confine a plasma in the shape of a torus (doughnut) using the Larmor motion. In a torus plasma, however, it is impossible to confine the plasma only with the toroidal fields along the torus (Fig.

1.3.1). The reason is that the plasma runaways in the radial direction, because the curvature and gradient of magnetic field lines cause vertical (Z-direction) movements, which are called curvature and ∇B drifts, and they induce charge separation and an electric field in the Z-direction, which bring about plasma motion in the radial direction called $E \times B$ drift motion. In order to avoid this plasma motion and to achieve a stable plasma force equilibrium, magnetic field lines that move around the torus with a helical perturbation are necessary. Such helical field lines can be generated by adding a poloidal field (traveling in circles orthogonal to the toroidal field) to the toroidal field (traveling around the torus in circles). In a tokamak, the toroidal field is produced externally by the coils that surround the torus, and the poloidal field is generated by a toroidal electric current that flows inside the plasma.
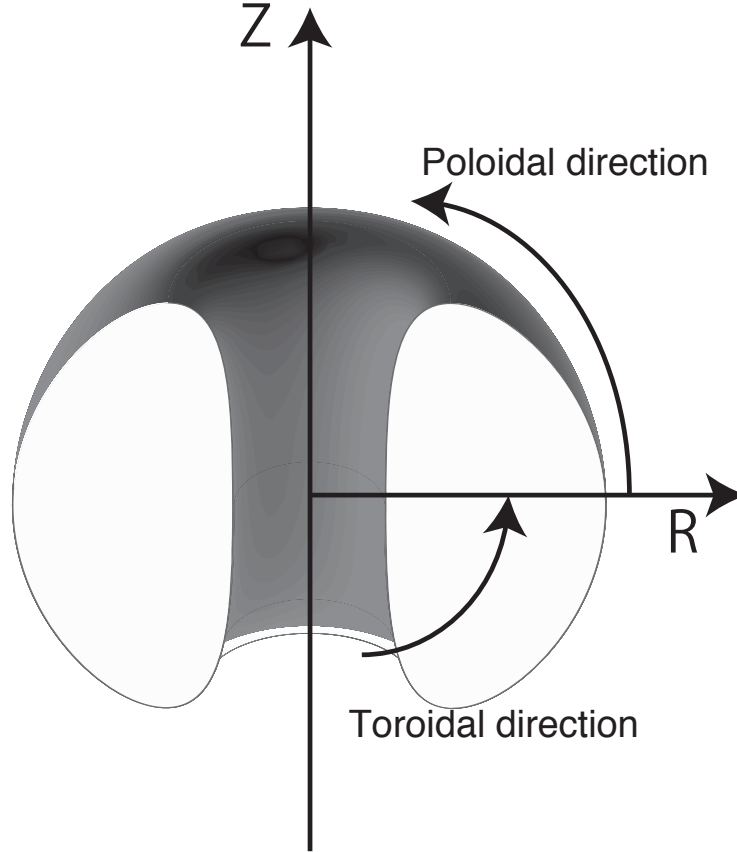
Figure 1.3.1: Schematic of toroidal coordinate system.

1.3.1 Spherical tokamak

The efficiency of confinement of plasma pressure by magnetic fields is given by the ratio

$$\beta = \frac{p}{B^2/2\mu_0} \quad . \tag{1.3.1}$$

This represents the ratio of the plasma pressure to the magnetic pressure. If β is low, larger amount of magnetic energy is needed to confine a plasma of the same pressure. A spherical tokamak has a small aspect ratio ($R_0/a < 1.6$) compared to a standard (i.e., conventional) tokamak's aspect ratio $R_0/a \sim 3$ [2]. Here, R_0 and a are the major and minor radii of the torus. The maximum limit of β is given by Troyon limit [3]

$$\beta_{max} = \beta_N \frac{I}{aB_0} = 0.072 \left(\frac{1+\kappa^2}{2} \frac{a}{R_0} \right), \tag{1.3.2}$$

where I is the plasma current, B_0 is the toroidal field strength at the center of the plasma and κ is the ratio of the vertical minor radius to the horizontal minor radius. Thus, STs (with small aspect ratios) can confine plasma with a relatively small magnetic energy and are very attractive for fusion reactors from an economic point of view.

1.4 Importance of turbulence study

In fusion plasma research, the study of anomalous transport by turbulence is important for controlling the transport and is also important for plasma operation [4]. Recent researches on turbulence are mainly focused on the new paradigm of plasma turbulence, i.e., nonlinear, non-local, non-stationary properties of multi-scale turbulence in the view of suppressing the amount of transport and obtaining optimized discharge conditions (e.g. a high confinement mode called H-mode) [5]. On the basis of the new paradigm, many experimental works have been performed intensively in linear plasmas, simple tori, helical, and tokamak plasmas [6].

It is pointed that the relatively low field B_T for a given plasma current I_p in a spherical tokamak usually leads to high current density, and drives strong magnetic fluctuations at the edge [7]. On the other hand, experimental investigations of edge turbulence in the spherical tokamak (ST) over a wide range of poloidal cross sections are not thoroughly carried out [8]. Thus, in order to elucidate the influence of this strong magnetic fluctuation to the turbulence and transport, measurements of both the magnetic field fluctuation and the edge turbulence are necessary. The TST-2 device is suitable for edge turbulence experiments. First, TST-2 has a short inter-discharge time, which is necessary to obtain a large number of data sets and to perform ensemble averaging in order to reveal the structure of plasma turbulence. In addition, TST-2 has good accessibility for Langmuir probes. For edge turbulence measurements, Langmuir probes are very useful because they have a better spatial resolution compared to the other diagnostics, and they can measure a wide variety of plasma quantities. Because of these benefits, Langmuir probes are suited for basic physics experiments on edge turbulence.

In this paper, we present the results of edge turbulence experiments on TST-2. We aim to contribute to the understanding of fusion physics by exploring the 3-dimensional structure of plasma edge turbulence. Since measurements on edge turbulence in STs have not been performed as thoroughly as other plasma confinement devices [9], it is important to investigate the structure of edge turbulence. Especially, measurements on the long range correlation along a magnetic field are very limited [10].

1.5 Structure of edge plasma

The static, single fluid Magneto-HydroDynamic (MHD) equilibrium is obtained by solving the force balance equation and Ampere's law,

$$\nabla p = \boldsymbol{j} \times \boldsymbol{B} \, , \tag{1.5.1}$$

$$\mu_0 \boldsymbol{j} = \nabla \times \boldsymbol{B} \, . \tag{1.5.2}$$

The flux surface is defined as a surface such that magnetic fields are parallel to the surface. In the case of tokamaks, a helical field line forms a surface on a torus as it travels toroidally. The force balance equation implies that p is constant along any field line, since ∇p is perpendicular to the field $\boldsymbol{B}$. The force balance equation also implies that p is constant on the flux surface. This force balance equation is valid only on scales greater than the gyro radius, and it is not the case in microscopic scales.

In tokamak research, it is convenient to introduce the poloidal flux function ψ. This function is determined so that the poloidal flux lying within each magnetic surface is constant on the surface. Thus,

$$\boldsymbol{B} \cdot \nabla \psi = 0 \, . \tag{1.5.3}$$

The Last Closed Flux Surface (LCFS) is the boundary between the closed flux surface region and the open field line region, separating the toroidally confined region from the region where field lines are connected to material surfaces (Fig. 1.5.1).

The Scrape off Layer (SOL) is the plasma region characterized by open field lines (beginning or ending on a material surface) and is located outside the LCFS. Transport in the SOL is very different from that in the confined region due to the open field lines. The transport in the SOL is predominantly convective rather than diffusive. Usually, the density decays exponentially away from the LCFS in the SOL, and radial convections of coherent plasma structures called 'blobs' are often observed. Blobs enhance the plasma interaction with the surrounding material boundaries [11].
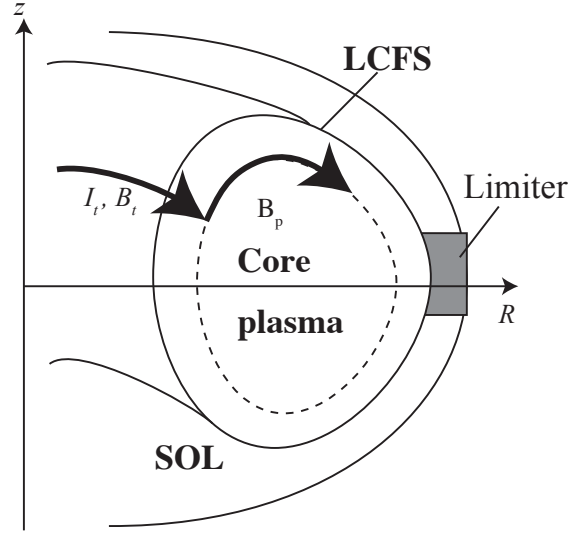
Figure 1.5.1: Schematic poloidal cross-section of a limiter configurations.

Inside the LCFS, plasma is confined with closed magnetic field lines. This confined plasma region is referred to as the core region, where the confinement is good, and usually the temperature, the density and the pressure profiles show peaks at the center of the core region. The profiles of the core plasma are determined by the interaction between the core and the edge plasmas, and suppression of transport in the edge leads to an improvement of the confinement in the core region [12].

1.6 Equations for plasmas

1.6.1 MHD equation

Plasma dynamics can have various characteristic time scales and spatial scales. Therefore, the choice of the equation is not unique for plasma turbulence. Instead, characteristic scales are chosen to simplify the complicated plasma dynamics.

Magnetohydrodynamics, or MHD, is the name usually given to a single fluid description of plasma. In this model, the different identities of ions and electrons do not appear.

The equation of mass conservation is

$$\frac{\partial}{\partial t}\rho + \nabla \cdot (\rho \boldsymbol{V}) = 0 \quad , \tag{1.6.1}$$

where ρ is the mass density, $\boldsymbol{V}$ is the fluid velocity. The equation of motion is given by

$$\rho \left(\frac{\partial \boldsymbol{V}}{\partial t} + \boldsymbol{V} \cdot \nabla \boldsymbol{V} \right) = \boldsymbol{j} \times \boldsymbol{B} - \nabla p \quad . \tag{1.6.2}$$

In order to calculate the pressure gradient force, an equation for pressure is required. The simple, non-dissipative and adiabatic model gives the equation,

$$\frac{\mathrm{d}}{\mathrm{d}t}(p\rho^{-\gamma}) = 0 \quad , \tag{1.6.3}$$

where γ is the adiabatic index. If the density is eliminated using Eq. (1.6.1), then Eq. (1.6.3) becomes

$$\frac{\partial p}{\partial t} + \boldsymbol{V} \cdot \nabla p = -\gamma p \nabla \cdot \boldsymbol{V} . \tag{1.6.4}$$

In the MHD model, the displacement current is neglected, The set of Maxwell equations is as follows,

$$\nabla \times \boldsymbol{B} = \mu_0 \boldsymbol{j} \quad , \tag{1.6.5}$$

$$\frac{\partial}{\partial t}\boldsymbol{B} = -\nabla \times \boldsymbol{E} \quad . \tag{1.6.6}$$

In the model of ideal MHD, the plasma is assumed to be perfectly conductive,

$$\boldsymbol{E} + \boldsymbol{V} \times \boldsymbol{B} = 0 \quad . \tag{1.6.7}$$

1.7 Background for the research of plasma turbulence

1.7.1 Transport

In the absence of instabilities, confinement of magnetically confined plasma is determined by Coulomb collisions and the orbits of charged particle motion. This is called classical transport, or neoclassical transport, when the magnetic mirror effect is considered. In reality, the actual transport does not agree well with the theoretical prediction, and the transport of particles can be up to two orders of magnitude higher than the predicted one. Such enhanced transport is called anomalous transport [1]. This is due to instabilities in plasma, and the transport is caused either by the perturbations which allow transport across the magnetic surfaces, or by break-up of the magnetic structure, followed by stochastization of particle trajectories. Although various sorts of instabilities are observed in tokamaks, the relationships between these are not yet clear [13]. Thus, we often use some empirical scaling laws, which are obtained by fitting functions to various data under various conditions, and we extrapolate the laws to the target conditions of plasma. Major part of anomalous transport is caused by electric field fluctuation $\tilde{E}$. The electric field results in $\boldsymbol{E} \times \boldsymbol{B}$ drift, and the induced particle transport is expressed as

$$\Gamma_\perp = \left\langle \tilde{n}_e \tilde{V}_\perp \right\rangle = \left\langle \tilde{n}_e \frac{\tilde{E}_\theta}{B} \right\rangle \equiv D_\perp \frac{\partial n_0}{\partial r}, \tag{1.7.1}$$

where $\tilde{V}_\perp$, $D_\perp$, $\tilde{n}_e$ and $\tilde{E}_\theta$ are the velocity perpendicular to the magnetic surface, perpendicular diffusion coefficient, density fluctuation and poloidal electric field fluctuation, respectively. Here we express the transport as a diffusion, because we believe the gradients in field quantities induce the instabilities and the transport. It should be noted that such an expression may not be true in the actual plasma where various non-linear interactions and collective phenomena play important roles. However, there is no other convenient form, and we often calculate the diffusion coefficient to express the amount of normalized transport.

Electrostatic fluctuation also induces a heat flux

$$q_\perp = \left\langle \tilde{p}_e \tilde{V}_\perp \right\rangle = \left\langle \tilde{p}_e \frac{\tilde{E}_\theta}{B} \right\rangle \equiv \chi_\perp \frac{\partial T_e}{\partial r}, \tag{1.7.2}$$

where $q_\perp$ is the heat flux perpendicular to the magnetic field, $\tilde{p}_e$ is the pressure fluctuation, $\chi_\perp$ is the perpendicular heat conductivity.

Random magnetic fluctuations also contribute to the net heat flux as described in Sec. 1.8.4.

1.7.2 Drift turbulence and flow

A drift wave is a phenomenon driven by the universal instability, where plasma pressure $p_e = n_e(T_e + T_i)$ contributes to expand the plasma, and the expansion is slowed by the magnetic pressure B^2/μ_0. The wave has finite wave lengths in both the poloidal and parallel directions. The wave propagates in the direction perpendicular to both ∇n and $\boldsymbol{B}$, which almost corresponds to the poloidal direction. The past decades of research in plasma confinement have shown that the plasma transport across magnetic surfaces is dominated by drift-wave fluctuations [14]. It should be noted that when a plasma flow exists, the effect of Doppler shift should be added to the intrinsic dispersion relation between k and ω, and the observed frequency can be different from the the prediction [15]. Strong modulations in plasma potential and other parameters appear [16]. In the presence of MHD turbulence and drift wave, which is the same situation in TST-2, a comparison of turbulence measurements and numerical turbulence simulations has been conducted[17]. However, satisfactory reproduction of the wavenumber spectra and the cross phases at the edge is not established yet.

1.8 Types of diffusion

In this section, several transport processes are described. Since collision between charged particles is a basic process in plasma, the particles always suffer from random walk due to the collision. The diffusion due to collision is referred to as classical or neoclassical diffusion, and their expression and features are well known. These diffusions are believed to set the lower limit to the transport perpendicular to magnetic flux surfaces. In actual plasmas, however, the contribution of turbulence is often much larger than the classical or neoclassical diffusions. Bohm diffusion is a semi-empirical expression for the turbulent transport, and is often used to compare with experimental results. While these three types of transport are used to express the transport across the magnetic surface, transport along field lines could be significant when the magnetic surfaces become stochastic, because the transport along field lines is usually much faster than the perpendicular transport and it can induce a net perpendicular transport. Rechester and Rosenbluth obtained an expression for the transport in such cases.

1.8.1 Classical diffusion

Classical diffusion is the type of diffusion determined only by the collision between electrons and ions. In order to realize such an ideal state, where the collisional diffusion is dominant, particles must collide each other before hitting the wall and move freely along a magnetic field line. Thus, the connection length $2\pi Rq$, which is the length of a field line to make a poloidal turn must be longer than the mean free path for this type of diffusion. Here, $q = (r/R)(B_T/B_\theta)$ is the safety factor, and B_θ and B_T are the poloidal and toroidal field components respectively. Thus, the particle diffusion coefficient $D_{classical}$ is

$$D_{classical} = (\rho_{\Omega_e})^2 \, v_{ei} = \frac{nT_e}{\sigma_\perp B^2} = \frac{\beta_e \eta_\parallel}{\mu_0} \, , \tag{1.8.1}$$

where $\sigma_\perp = n_e e^2/(m_e v_{ei})$, $\quad \eta_\parallel = 1/2\sigma_\perp$. v_{ei} is electron to ion collision frequency, ρ_{Ω_e} is a radius of the electron orbit of Larmor motion.

In the case of toroidal plasma, the step length of diffusion becomes

$$\Delta \approx \rho_{\Omega_e} \frac{2\pi}{\iota} \, , \tag{1.8.2}$$

where ι is the rotational transform angle given by

$$\frac{\iota}{2\pi} = \frac{R}{r} \frac{B_\theta}{B_T} = \frac{1}{q} \, . \tag{1.8.3}$$

Consequently, the diffusion coefficient becomes

$$D_{P.S} = \left(\frac{2\pi}{\iota}\right)^2 (\rho_{\Omega e})^2 \, v_{ei} \, . \tag{1.8.4}$$

This diffusion coefficient is called Pfirsch-Schlüter diffusion coefficient.

1.8.2 Neoclassical diffusion

Larmor motion is a periodic motion, and it has an adiabatic invariance called magnetic moment $\mu_m = IS$, where I is the current, S is the area encircled by the current. If magnetic field strength B increases along the field line and a charged particle is traveling along the field line, $mv_\perp^2 = \mu_m B$ also increases. Since its total kinetic energy $mv^2/2 = mv_\parallel^2/2 + mv_\perp^2/2$ is also a constant of motion, $mv_\parallel^2/2$ should decrease. Eventually, the parallel movement of the particle is reversed as a mirror reflects light. The ratio of the maximum field strength to the minimum is called the "mirror ratio"

In a uniform magnetic field, charged particles gyrate around a magnetic field line with a constant velocity. However, the magnetic field strength in a tokamak is not uniform, and leads to drifts of the guiding centers. The outboard side of the torus forms a weak field region, while the inboard side forms a strong field region. Therefore, a helical field line in a tokamak connects both regions, and it make a magnetic mirror configuration. As a result, some particles are trapped in the outboard side region, where the magnetic field strength is weak.

Such an orbit is called a banana orbit. Since the fraction of such trapped particles is $\epsilon_t^{1/2}$, where ϵ_t is the inverse aspect ratio r/R_0, the trapped particles heavily contribute to the diffusion due to their wide orbit widths (i.e., banana widths), and the diffusion coefficient is written as

$$D_b = \epsilon_t^{1/2} \Delta_b^2 \nu_{eff} = \epsilon_t^{-3/2} \left(\frac{2\pi}{\iota}\right)^2 (\rho_{\Omega_e})^2 \nu_{ei}, \tag{1.8.5}$$

where D_b is the diffusion coefficient for neoclassical diffusion with banana orbit and Δ_b is the banana width.

This diffusion coefficient is $\epsilon_t^{-3/2}$ times larger than that of Pfirsch-Schlüter diffusion case in Eq. (1.8.4).

Whether diffusion process follows the above neoclassical theory or the Pfirsch-Schlüter diffusion is determined by collision frequency. If the electron-ion collision frequency is larger than the frequency $\nu_{P.S}$ given by

$$\nu_{ei} > \nu_{P.S} = \frac{1}{R}\frac{2\pi}{\iota}\upsilon_{T_e}, \tag{1.8.6}$$

the connection length becomes longer than the mean free path, and MHD treatment, but Pfirsch-Schlüter diffusion is applicable. When the electron to ion collision frequency ν_{ei} is smaller then the frequency

$$\nu_b = \epsilon_t^{3/2}\nu_{P.S}, \tag{1.8.7}$$

the electron can complete a banana orbit, and the neoclassical diffusion with banana orbit can be applied.

In summary, the diffusion coefficient for collisional plasma is

$$D_{P.S.} = \left(\frac{2\pi}{\iota}\right)^2 (\rho_{\Omega_e})^2 \nu_{ei}, \qquad \nu_{ei} > \nu_{P.S}, \tag{1.8.8}$$

where $\rho_{\Omega e}$ is the Lamor radius of electron. When the mean free paths of the electrons and ions are long enough to complete a banana orbit, the diffusion coefficient is

$$D_b = \epsilon^{-3/2} \left(\frac{2\pi}{\iota}\right)^2 (\rho_{\Omega_e})^2 \nu_{ei}, \qquad \nu_{ei} < \nu_b = \epsilon_t^{3/2}\nu_{P.S}. \tag{1.8.9}$$

In the intermediate region of these two collisionalities, the diffusion coefficient is written as

$$D_p = \left(\frac{2\pi}{\iota}\right)^2 (\rho_{\Omega_e})^2 \nu_{P.S}, \qquad \nu_{P.S} > \nu_{ei} > \nu_b = \epsilon_t^{3/2}\nu_{P.S}. \tag{1.8.10}$$

If ν_{ei} is in the intermediate range ($\nu_b < \nu_{ei} < \nu_{P.S}$), drift approximation of Vlasov's equation can be applied. This region is called the "plateau region". In this case, the diffusion coefficient is not sensitive to the collision frequency [18]. The region $\nu_{ei} > \nu_p$ is called the "collisional region", and the region $\nu_{ei} < \nu_b$ is called the "banana region". The combination of these three types of diffusion is called neoclassical diffusion (Fig. 1.8.1) [18].

1.8.3 Bohm diffusion

The neoclassical diffusion we mentioned above is derived from collision of charged particles. In reality, plasma has various types of instabilities. The resultant fluctuations drive collective motions and they lead to anomalous losses. These fluctuations can couple with density and pressure gradient, and excite electrostatic waves. The excited wave is expressed as

$$\frac{\tilde{n}_k}{n_0} = \frac{\omega_k^*}{\omega_k}\frac{e\tilde{\Phi}_{p,k}}{k_B T_e}, \tag{1.8.11}$$

where $\tilde{n}_k$, $\tilde{\Phi}_{p,k}$ and ω_k are the density and the potential fluctuation with wavenumber k and frequency ω_k. The drift frequency ω_k^* satisfies the dispersion relation of the drift wave and can be expressed as

$$\omega_k^* = k_\theta \frac{k_B T_e}{e B n_0}\frac{dn_0}{dr}. \tag{1.8.12}$$

15
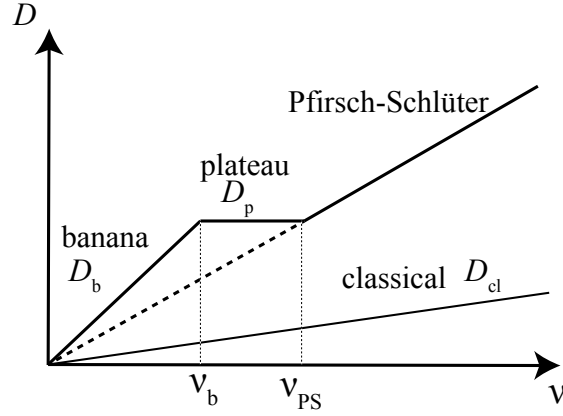
Figure 1.8.1: Dependence of the diffusion coefficient on collision frequency in a tokamak [13].

When ω_k is complex and can be written as $\omega_k = \omega_{r,k} + i\gamma = \omega_k^* A_k \exp(i\alpha_k)$, the electrostatic wave expressed by Eq. (1.8.11) causes particle transport (A_k is a positive constant and α_k is the phase difference). The diffusion coefficient due to this wave is [1]

$$D_\perp = \left(\sum_k k_\theta \frac{n_0}{dn_0/dr} A_k \sin \alpha_k \left| \frac{\tilde{n}_k}{n_0} \right|^2 \exp 2\gamma_k t \right) \frac{k_B T_e}{eB} . \tag{1.8.13}$$

The term inside the parenthesis is taken as 1/16 empirically and the diffusion coefficient becomes

$$D_B = \frac{1}{16} \frac{k_B T_e}{eB} . \tag{1.8.14}$$

This type of the transport derived by D. Bohm is called Bohm diffusion [19]. Bohm diffusion coefficient is much greater than those from neoclassical theories, and it was often used to evaluate low temperature plasmas. However, this value is not valid in modern high temperature tokamak plasma [20]. Even though it cannot be applied to the core, it is still useful to compare the experimental diffusion coefficient and the Bohm diffusion at the edge, where the temperature is low and fluctuations are large.

1.8.4 Rechester Rosenbluth diffusion

Rechester-Rosenbluth type diffusion (RR diffusion) is the type of diffusion caused by stochastization of magnetic fields [21]. In this case, the static magnetic perturbation is assumed, and the condition $\omega < v_{T_e}/R$ should be satisfied, where ω is the frequency of the magnetic field fluctuation. When there are various harmonics in magnetic perturbations, each of the harmonics destroys or deforms the flux surfaces around the corresponding rational surface. They often generate magnetic islands on the rational surfaces. With the increase in the perturbation amplitudes, the affected regions (e.g. magnetic islands) grow in size, and the perturbed regions of neighboring rational surfaces overlap. Then the magnetic surfaces are destroyed and stochastization occurs. Since particles move almost freely along a field line, such stochastic magnetic field line structure induces a net (radial) diffusion even though the stochastic structure is static. Let us think the situation where a magnetic field moves radially by Δr when we trace the magnetic field by a distance of L. When we adopt a correlation length L_c for the distance L, the movement of the magnetic field can be considered as a random walk process, where radial step size is Δr.

According to the random walk theory, the diffusion coefficient is given by

$$\langle (\Delta r)^2 \rangle = 2D_{st}\tau , \tag{1.8.15}$$

where τ is the time interval of movement of particles before the stochastization of the magnetic field line. In the case of RR diffusion, we introduce the correlation length, which corresponds to the time step of the random walk. The correlation length is written as

$$l_{corr} = \frac{\left\langle \int_{-\infty}^{\infty} \tilde{B}_r(l)\tilde{B}_r(0)dl \right\rangle}{\left\langle \tilde{B}_r^2(0) \right\rangle} . \tag{1.8.16}$$

16

where l is the distance along the direction of correlation.

This diffusion by the stochastization of magnetic fields occurs even in collisionless plasma. RR diffusion has not been considered to be significant in tokamak plasmas, while in reversed field pinch (RFP) plasmas, and in the edge of helical plasmas RR diffusion is significant [22]. In the case of RFP plasmas, it is inferred that the condition of stochastization of magnetic field is $|B_{st}|^2/B_z^2 \sim 10^{-8}$ [21].

1.9 Review of edge plasma measurements

Edge plasma turbulence is widely studied because it determines the radial transport and affects the global confinement. In addition, heat and particle fluxes from plasma to a material wall are crucial topics in the ITER device [12]. Thus, research of edge turbulence has been the key element in plasma fusion research. Radial particle flux is determined by the product of density and radial velocity. It is usually evaluated as $\Gamma_r = \tilde{n}\tilde{v}_r = \tilde{n}\tilde{E}_{pol}/B$, assuming the radial velocity is given by $v_r = E_{pol}/B$. The radial profile of particle flux driven by turbulence is roughly consistent with the particle loss rate inside the LCFS. However, the discrepancy between turbulent flux and particle loss becomes large in the SOL, because the effects of intermittent particle transport and poloidal asymmetry become significant [23].

In magnetically confined plasmas, the plasma turbulence at the edge is known to have a quasi two-dimensional structure. The correlation length and the scale length of turbulence perpendicular to the magnetic field are in the order of millimeters, while the correlation length parallel to the magnetic field is in the order of meters. Spectrum-averaged poloidal correlation length in tokamaks was $l_{pol} \sim 0.5 - 5$ cm and radial correlation length was $l_r \sim (0.5 - 1)\, l_{pol}$ [23]. Direct measurement of the parallel correlation length $l_\parallel$ is limited, but several experiments showed $l_\parallel$ is very long. In the Joint European Torus experiment, $l_\parallel$ longer than 100 m was reported [24]. Since $l_\parallel \gg l_{pol}$, it is often assumed that the turbulent structure along the field line is completely uniform, but this is not appropriate since there is a poloidal asymmetry in the edge density fluctuation on the same magnetic flux surface [25]. There is also difference in wavenumbers perpendicular and parallel to the magnetic field line. In all experiments, $k_\parallel/k_{pol} < 10^{-2}$ is observed. In a TEXT experiment for example, $k_\parallel = 0.08 \pm 0.04\,\mathrm{m}^{-1}$ is measured with two Langmuir probes separated by 12 m fixed at the limiter location [26]. In addition, finite $k_\parallel$ has been found when there are two Langmuir probes on the same magnetic field line, and bias voltage is imposed on the Langmuir probe at the downstream side [27]. These data are consistent with an Alfven-type wave propagating along the magnetic flux tube.

Radial profiles of edge turbulence show fairly universal characteristics among conventional tokamaks. The density and temperature fluctuation levels at the edge increase smoothly with radius across the LCFS [28]. Figure 1.9.1 shows the radial profiles of relative fluctuation levels of various parameters in TEXT. The relative electron density fluctuations at the outboard midplane are $\tilde{n}/n \sim 0.05$ inside the LCFS and $\tilde{n}/n \sim 1$ in the far SOL in the D III-D experiments [23]. If sufficient electrons are supplied along the field line and if polarization drift and finite Larmor radius effects are neglected, electrons reach thermal equilibrium and exactly follow the Boltzmann relation $\tilde{\phi}/kT_e = \tilde{n}_e/\overline{n}_e$, and the density and potential perturbations are in phase [29]. However, in various experiments, the Boltzmann relation is not satisfied in the plasma edge, neither in the amplitudes nor in the phase between $\tilde{n}_e$ and $\tilde{\phi}$. In ohmically heated plasmas in TEXT, the electrostatic potential fluctuations ϕ decrease with the radius while both density and temperature fluctuations increase. The magnetic fluctuation level in conventional tokamaks is typically $\tilde{B}_r/B_T \sim 10^{-5}$ at the edge, and increase to $\sim 10^{-4}$ inside the LCFS.

The power spectrum of the edge turbulence is often flat in the range of 10-100 kHz, and the dominant component in this frequency range is considered to be a drift wave. It is widely known that electrostatic drift wave turbulence is responsible for the anomalous transport at the plasma edge [14]. However, there is no conclusive theory to explain the whole turbulence and edge transport until now. Some simulations and experiments suggest that the radial electron pressure gradient can destabilize drift waves [30], and also magnetic fluctuations could be an ingredient of the destabilization mechanism of drift waves [31] [19].

Another motivation of the research of plasma turbulence is to understand the origin of the H-mode. In tokamaks, there is two types of confinement modes, called the low confinement mode (L-mode) and the high confinement mode (H-mode). The H-mode is characterized by a presence of steep gradients of temperature and density at the edge, called a transport barrier. The transition from an L-mode to an H-mode was found in a divertor configuration with a sufficiently high heating power [13]. This transition is correlated with the presence of edge $\boldsymbol{E} \times \boldsymbol{B}$ flows. Various experiments suggest strong edge flow inhibits the plasma transport [23]. In TST-2, there is no H-mode since it has neither a divertor nor additional heating, but there is still

importance in elucidating the relation between $E \times B$ flow and edge turbulence.

The characteristics of edge turbulence and transport in STs are not intrinsically different from that of conventional tokamaks [32]. However, high β plasma of STs can lead to larger Lamor radius and greater electromagnetic fluctuations like kinetic ballooning mode and micro tearing mode [33]. Furthermore, it is also pointed out that high pressure gradient and current density at the edge can lead to strong MHD fluctuations like a peeling ballooning mode [34]. Previous researches in ohmically heated plasmas of MAST and TST-2 suggest the presence of a large MHD fluctuation, which is considered to be an internal reconnection event (IRE) [35]. IREs in MAST are accompanied by $m = 2/n = 1$ and $m = 5/n = 2$ tearing modes at $q = 2$ rational surface, here m and n are poloidal and toroidal mode numbers, respectively. A similar structure is observed in TST-2. IREs in TST-2 are followed by $n = 1$ mode which propagates from $\rho = 0.3$ ($\rho = r/a$ is the normalized plasma radius). The information of radial fluctuation profile in STs is limited compared to that of conventional tokamaks. In spite of the large amplitude magnetic fluctuations in STs, information on the radial distribution of magnetic fluctuations has been scarce.
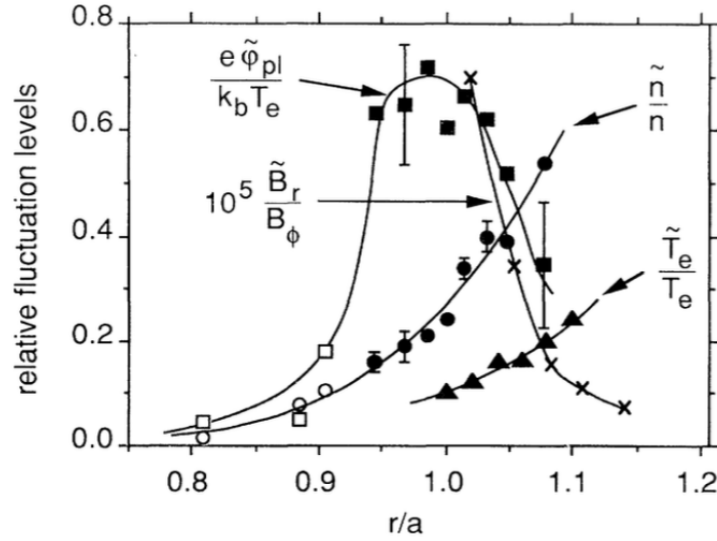
Figure 1.9.1: Relative fluctuation levels of density, plasma potential, temperature and radial magnetic field in TEXT [29].

The fluctuation levels in the edge of STs are summarized in table 1.9.1. Most STs have magnetic fluctuation measurement systems fixed at the wall, but they usually do not measure the radial distribution of magnetic fluctuations directly. For example, MAST has an extensive set of magnetic diagnostics installed inside the vacuum vessel [36]. However, the radial distribution of magnetic fluctuations and their amplitudes have not been reported [37]. PEGASUS installed a hall probe system to measure poloidal magnetic field inside the LCFS, however the radial magnetic fluctuation profile has not been measured [38]. SUNIST measured the radial distribution of $\tilde{T}_e$, $\tilde{n}_e$, $\tilde{\phi}$ and $\tilde{B}_r$ [39], but $\tilde{B}_r$ is not measured simultaneously with the other parameters, and the magnetic fluctuation amplitude level is relatively low compared to other STs [40]. TST-M has also measured $\tilde{B}_r$ inside the LCFS with insertable pick-up coils. However, simultaneous measurements with $\tilde{\phi}$, $\tilde{n}_e$, $\tilde{B}_r$ and $\tilde{T}_e$ have not been conducted. A strong magnetic fluctuation is observed in HIST, but the discharge duration is too short to achieve a steady state turbulence, thus it may be inappropriate to compare the result to those of other STs. The radial correlation length l_r and the poloidal correlation length l_{pol} are measured by beam emission spectroscopy in MAST and NSTX, and Langmuir probes in SUNIST. However, the parallel correlation length $l_{\parallel}$ has not been measured in STs until now. The radial positions of measurements in each machine is presented by the normalized radius r/a in table 1.9.1.

1.10 Objective of the thesis

In order to elucidate the characteristics of plasmas in TST-2, it is necessary to know the edge turbulent structure and its contribution to transport. Comparison between the turbulent structures in TST-2 and those

	$\tilde{V}_{\mathrm{p}}/eT_e$	$\tilde{n}_e/\bar{n}_e$	$\tilde{B}_r/B_T$	$\tilde{T}_e/\bar{T}_e$	l_r	l_{pol}	$l_{\parallel}$	r/a
PEGASUS[41]	–	10-30 %	1% [1]	10-30 %	–	–	–	0.5-1.0
MAST[42]	–	20-60 %	–	–	4-8 cm	10-20 cm	–	0.6-1.0
HIST [43]	–	–	1.5 % [1]	–	–	–	–	0-1.3
NSTX[44][45][46]	–	1-5 %	0.2% [2]	–	3-6 cm	15 cm	–	0.85-0.95
SUNIST [47]	20-80 %	20-60 %	0.02-0.05 %	10-30 %	1.5 cm	2-2.5 cm	–	0.85-1.2
Globus-M[48]	–	–	0.5 % [2]	–	–	–	–	–
TST-M [49]	5-20 %	–	0.01-0.05 %	–	–	–	–	0.5-1.5

[1] poloidal magnetic field
[2] signals from coil fixed at the wall

Table 1.9.1: The fluctuation levels at the edge and correlation length in spherical tokamaks.

in conventional tokamaks is also needed. These are possible only by high spatial and temporal resolution measurements by Langmuir probes and magnetic coils. Our objectives in this thesis can be divided into the following four major parts.

1. Comparison of the structures of edge turbulence in conventional tokamaks and STs: Structure of edge turbulence in conventional tokamaks is dominated by drift waves, characterized by the presence of plasma potential and electron density fluctuations. However, this is not necessarily the case in high β and high edge current density ST plasmas like TST-2.

2. Clarification of the spatial dependence of turbulence characteristics in the low field side region : Strong magnetic field fluctuation is observed in ohmic discharges in TST-2. Thus we try to clarify the structure of magnetic fluctuation, wavenumber and correlation length, and compare the structure with ballooning mode fluctuations observed in other tokamaks.

3. Evaluation of the particle transports due to electrostatic fluctuation and magnetic fluctuation.

4. Investigation of the structures of MHD fluctuation and drift wave along a magnetic field line : Structures along a field line, including the parallel wavelength and the parallel correlation length, are investigated for various frequencies.

Furthermore, since the wavelength and frequency of MHD fluctuation and drift wave are much different, interplay between them can happen. Thus, we investigate the effects on the drift wave like turbulence, including nonlinear effects.

Chapter 2

Principles of measurement and analysis

2.1 Langmuir probe

A Langmuir probe is one of the simplest ways to diagnose plasma. Using a small electrode inserted into plasmas, we can measure electron density, electron temperature, space potential, and energy distribution function from its voltage-current characteristics. Since the probe is immersed in harsh environment, this method is applicable only for low temperature edge plasmas to protect the electrodes.

The problem in using a Langmuir probe is that they can significantly perturb the plasma or vice versa. The main issue affecting the Langmuir probe measurement is the influx at the probe surface. Measurements of the plasmas with and without Langmuir probes suggest that the level of fluxes is unchanged even when a Langmuir probe was inserted into the SOL region [50]. Similar observation is reported in TEXT, HL-1 and ATF [51]. However, some clear differences are observed; that is, the radial outward fluxes increase when probes are inserted inside the LCFS [52] [53]. Even if the global parameters of the plasmas are unchanged, the fluctuation induced flux appears to be much larger inside the LCFS than the actual value without probe insertion. Thus, radial fluxes show discrepancy between the particle continuity equation and the fluctuation induced flux. It is pointed that the plasma region shadowed by the probe body becomes a presheath region, and the plasma shows different characteristics in that region [54]. B. LaBombard suggested that the flux $\Gamma_{\perp\text{probe}}$ caused by the presence of the probe itself is written as [52]

$$\Gamma_{\perp\text{probe}} \approx \frac{D_{\perp\text{ps}} n}{2a}, \tag{2.1.1}$$

where a is the size of the probe, $D_{\perp\text{ps}}$ is particle diffusivity at the presheath. If $D_{\perp\text{ps}}$ is comparable to that of SOL, $\Gamma_{\perp\text{probe}}$ becomes comparable to the actual particle flux. The actual value of $D_{\perp\text{ps}}$ in presheath is unknown, but experiments in C-Mod suggest that $\Gamma_{\perp\text{probe}}$ is comparable to the actual particle flux. On the other hand, experiments in TJ-II stellarator showed the particle flux measured in and out of the probe sheath is consistent, even when the mean values of ion saturation current and the floating potential are different [55] .

In typical parameters in TST-2, electron density is one order smaller than that of TJ-II. Because $\Gamma_{\perp\text{probe}}$ is proportional to the density (Eq. (2.1.1)), it is considered that the disturbance of the probe is also comparable or smaller than that of TJ-II. This implies that the effect of shadowing by the probe body can be negligible in TST-2, as long as the global parameters of the plasmas are unchanged.

Figure 2.1.1 shows the basic configuration of the probe circuit. The Langmuir probe collects ion or electron current that flows to it in response to the applied voltages. The current vs. voltage trace, called the V-I characteristic, can be analyzed to reveal the information on the plasma. The probe electrodes are connected to a variable voltage source through a vacuum feedthrough and then terminated to the ground by a resistor *R*. To measure the probe current, the voltage across *R* is recorded by a digitizer.
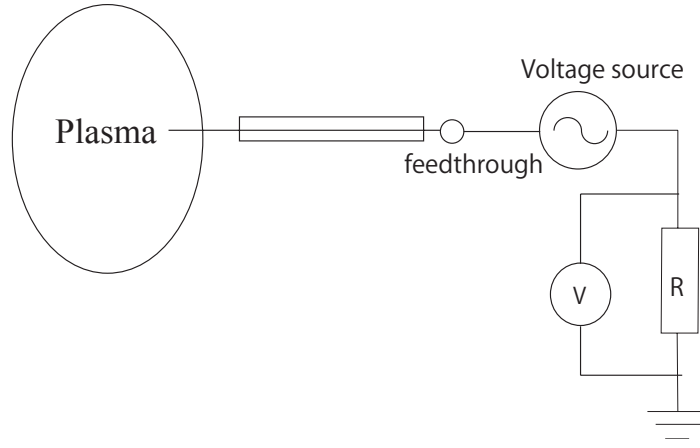
Figure 2.1.1: Basic configuration of the probe circuit.

2.1.1 V-I characteristic of probes

Figure 2.1.2 shows a schematic probe characteristics (i.e., V-I curve) that how the probe current I_{probe} varies with probe voltage V_{probe}. I_{probe} is positive in the direction of electron current for the sake of convenience. The V-I curve has three distinct parts. In the region where V_{probe} is sufficiently negative , I_{probe} is comprised of a constant value called ion saturation current I_{is}. As V_{probe} increases, I_{probe} becomes zero due to the electron current. This voltage is called floating potential V_{f}. As V_{probe} increases further, the electron current increases rapidly, and V-I curve shows an exponential behavior, because the lowered Coulomb barrier allows slower electrons in the Maxwellian distribution to penetrate the barrier. As V_{probe} approaches to the space potential V_{p}, the curve shows a bend, and saturates at the electron saturation current I_{es}. Actual V-I curves in magnetized plasmas are distorted by various fluctuations, as shown in Fig. 2.1.3.

The exponential part of the V-I curve can be expressed as

$$I_{\text{probe}} = I_{es} \exp\left[\frac{e(V_{\text{probe}} - V_{\text{p}})}{k_B T_e}\right] - I_{\text{is}} . \tag{2.1.2}$$

When I_{probe} is plotted in logarithm scale, the V-dependence appears as a straight line. Since the slope in the $\ln I_{\text{probe}} - V_{\text{probe}}$ plane is $1/T_e$, we can measure the electron temperature. Ion saturation current I_{is} and electron saturation current I_{es} can be obtained as

$$I_{\text{is}} = \frac{1}{2} e n_i A \sqrt{\frac{k_B T_e}{m_i}} , \tag{2.1.3}$$

$$I_{es} = \frac{e A n_e \bar{v}}{4} = e n_e A \sqrt{\frac{k_B T_e}{2\pi m_e}} , \tag{2.1.4}$$

where A is the area of the electrode surface. The measurement of I_{is} is the simplest way to determine the plasma ion density n_i.

The factor $\frac{1}{2}$ in Eq. (2.1.3) varies due to the secondary electron emission from the probe and the plasma sheath thickness and the shape of the probe. The space potential satisfies

$$V_{\text{p}} - V_{\text{f}} = (k_B T_e/2e) \cdot \ln\left(\frac{\epsilon M_i}{2\pi m_e}\right) , \tag{2.1.5}$$

where ϵ is the base of natural logarithm. Thus, the floating potential V_{f} is strongly influenced by electron temperature.

When a probe is inserted into a plasma, the potential near the electrode drops sharply. This is called the sheath, of which thickness is the order of the Debye length, and the probe potential is shielded from the plasma. When the applied voltage to the probe is too high (in the negative or in the positive directions), the large sheath voltage difference may invoke a spark, and V-I curves would be distorted.
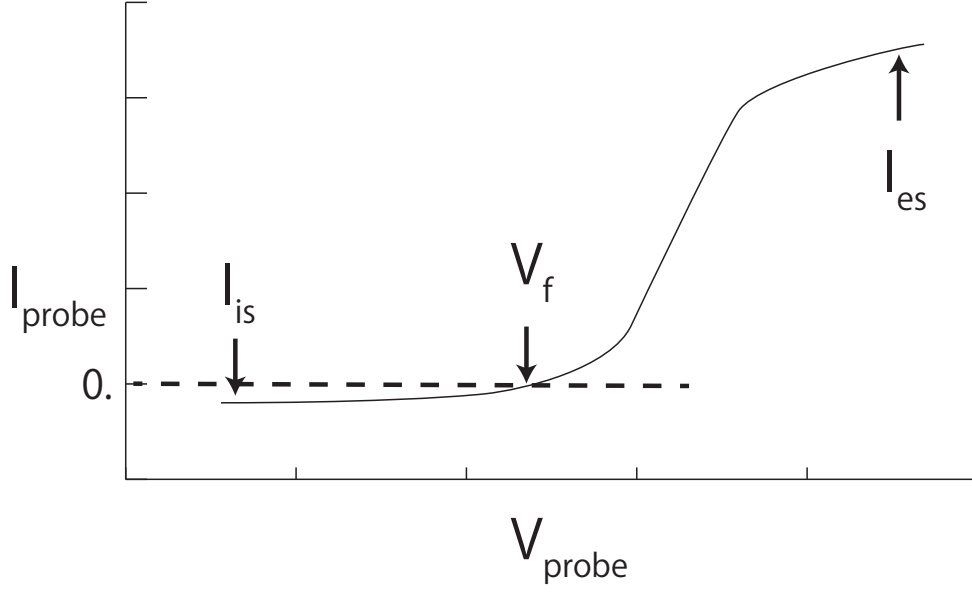
Figure 2.1.2: Schematic V-I curve.
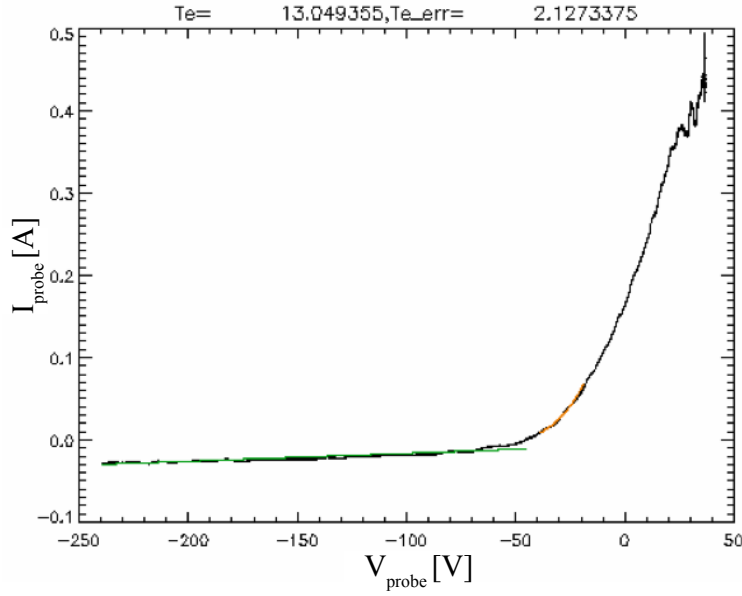
Figure 2.1.3: An example of a V-I curve in a TST-2 plasma.

2.1.2 Electronic circuit for Langmuir probes

In order to acquire V-I curves, we can apply a voltage V_{probe} to the probe to measure the current I_{probe} in two basic ways, and each has its disadvantages [56]. In Fig. 2.1.1, the probe is connected through a vacuum feedthrough to a voltage source (bias supply) and then to the ground through a termination resistor R. The voltage across R is recorded by a digitizer to measure the probe current. This arrangement has the advantage that the resistor and the digitizer are grounded, and therefore the method is not subject to suspicious pickup of noises. The disadvantage is that the bias supply is floating. When the capacitance between the probe and the ground is so large that the AC signals would be short-circuited to the ground, and the measurement would have a poor frequency response. Furthermore, the voltage source can act as an antenna and become susceptible to RF noises.

Second way is to terminate the bias supply to the ground and insert the resistor between the probe and the

bias supply. This method can avoid RF noises, but the voltage across the resistor has to be measured by a differential amplifier or some other floating device. In order to measure the plasma potential with a Langmuir probe, we often terminate the probe with a high impedance, such as the 1 MΩ input resistance of the digitizer. This is called a floating probe. The value of R has to be high enough so that the current I drawn from the plasma is small and the effect on the plasma is negligible. The value of R is chosen so that $I_{is}R$ should be much greater than T_e [V], or $R \gg T_e/I_{is}$. The large value of R leads to a poor frequency response, because the RC time constant due to R and the stray capacitance C deteriorates high frequency signals [57].

2.2 Spectral analysis

Spectral analysis is a basic way to analyze time series data. To examine the presence of periodicity of data, Fast Fourier Transform (FFT) is often used [58]. In plasma research, spectral analysis is one of the most effective methods to quantify the statistical properties of fluctuations and the resultant transport. Here, we will describe the spectral analysis method. In addition, the methods to determine the wavenumber $k_\parallel$ and $k_\perp$ distributions and the correlation lengths are described. FFT decomposes a data array into corresponding sinusoidal waves by Fourier transform.

$$X(f) = \int_{-\infty}^{\infty} x(t)e^{-i2\pi ft}\mathrm{d}t, \tag{2.2.1}$$

where $X(f)$ is the Fourier series coefficient, (i.e., the amplitude of the sinusoidal wave) for frequency f. The power spectrum defined in the equation below, indicates energies (as a function of f) distributed to the waves. The power spectrum is written as

$$P(f) = \lim_{T\to\infty}\left\langle \frac{1}{T}X(f)X^*(f) \right\rangle. \tag{2.2.2}$$

Here, angle brackets $\langle\rangle$ indicate an ensemble average and T is the time window of the sampled data.

In order to quantify correlation of two data sets, a cross spectrum is often used. This is defined as

$$S_{xy}(\omega) = \left\langle \frac{2\pi}{T}X^*(\omega)Y(\omega) \right\rangle. \tag{2.2.3}$$

From the cross spectrum, coherence and cross phase can be calculated. The coherence is a value that can be used to examine the relationship between two signals $x(t)$ and $y(t)$, and it is defined as

$$C_{xy}(\omega) = \frac{|S_{xy}(\omega)^2|}{S_{xx}(\omega)S_{yy}(\omega)}. \tag{2.2.4}$$

The values of coherence C_{xy} are always in the range $0 < C_{xy} < 1$, and if $x(t)$ and $y(t)$ are completely correlated, $C_{xy} = 1$. Using the real and imaginary components of the cross spectrum, cross phase, the phase difference between X and Y can be calculated from

$$\theta_{xy} = \tan^{-1}\left(\frac{\Im S_{xy}(\omega)}{\Re S_{xy}(\omega)}\right). \tag{2.2.5}$$

2.2.1 Spatio-temporal statistics

When fluctuations are invoked by a mechanism described by a linear partial differential equation, each of its independent solution has a certain wavenumber and a frequency. Therefore, the wavenumber becomes a function of frequency, that is the dispersion relation $k(\omega)$. In plasma turbulence, however, the power spectrum of fluctuations tends to become broad, and the power should be expressed by a spectral distribution $S(k,\omega)$. For a given angular frequency ω and a given wavenumber range k to $k + \Delta k$, $S(k,\omega)\Delta k$ represents the fractional power of the turbulence. It should be noted that, in this paper, the angular frequency ω is discretized, and the frequency resolution (or range) $\Delta\omega$ does not appear in our formulation. When some fluctuating value $\phi(x,t)$ in plasma satisfies a dispersion relation $k(\omega)$, the spectral density takes the form

$$S(k,\omega) = S(\omega)\delta[k - k(\omega)]. \tag{2.2.6}$$

When the wavenumber spectrum is normalized by the total power $S(\omega)$ for a given (discretized) ω, this corresponds to the probability function $s(k, \omega)$ defined as

$$s(k, \omega)\Delta k = S(k, \omega)\Delta k / S(\omega). \tag{2.2.7}$$

For the given ω, $s(k, \omega)\Delta k$ represents the probability being in the range k to $k + \Delta k$. The average wavenumber $\bar{k}$ is written as

$$\bar{k}(\omega) = \int dk \, k \, s(k, \omega). \tag{2.2.8}$$

Let us take an (ensemble averaged) cross phase $S_{xy}^{j}(\omega)$ indexed by j. Here x and y are signals obtained at different locations separated by distance Δx. Then we can calculate a nominal wavenumber k_f^j written by

$$k_f^j = \theta_{XY}^j / \Delta x = \tan^{-1}\left(\frac{\Re S_{xy}^j(\omega)}{\Im S_{xy}^j(\omega)}\right)/\Delta x, \tag{2.2.9}$$

and the calculated k_f^j is a sample local wavenumber for the cross spectrum indexed by j. When we perform the measurements and the calculations many times, we may obtain different wavenumbers. Here we assume that obtained each wavenumber is a sample of the parent population described by a probability distribution function $s(k, f)$. By accumulating the sample wavenumbers k_f^j, we can speculate the parent population $s(k, \omega)$. A speculated probability distribution (i.e., power spectrum) $S_L(k, f)$, is computed by depositing the two point averaged power at the wavenumber k_f^j calculated by Eq. (2.2.9). Then $S_L(k, f)$ is calculated as

$$S_L(k, f) = \sum_j \frac{1}{2}(X_f^{*,j} X_f^j + Y_f^{*,j} Y_f^j)\delta(k_f^j - k). \tag{2.2.10}$$

Hereafter, we use frequency f instead of the angular frequency ω $(= 2\pi f)$. The actual $S(k, \omega)$ can be approximated by $S_L(k, f)$ when the spatial scale of amplitude and wavenumber variation is much longer than the local wavelength $(2\pi/\bar{k})$, and the maximum wavenumber must be smaller than the maximum phase difference $k_{max} < 2\pi/\Delta x$ [59].

Since the particles can move almost freely along a magnetic field line, the spatial perturbations tend to be perpendicular to the field line. As a result, fluctuations would normally have a very long wavelength and a very long correlation length along the field line, while the perpendicular lengths are short. Therefore, we must deal with the parallel wavenumber $k_{\parallel}$, the perpendicular wavenumber $k_{\perp}$ and the radial wavenumber k_r differently. Hereafter, the perpendicular wavenumber is split into k_r, which is perpendicular to a flux surface, and $k_{\perp}$, which lies on the surface.

The parallel wavenumber $k_{\parallel}$ of plasma along a field line is much smaller than the perpendicular wavenumber $k_{\perp}$. Thus, we have to know the magnetic field lines accurately to obtain the correct $k_{\parallel}$. When the two probe electrodes are placed on the same field line, $k_{\parallel}$ is calculated by,

$$k_{\parallel}^j = \Delta\theta_{XY}^j / \Delta x, \tag{2.2.11}$$

$$\bar{k}_{\parallel}(f) = \int dk \, k_{\parallel} \, s(k, \omega) = \sum_j (X_f^{*,j} X_f^j + Y_f^{*,j} Y_f^j) k_f^j / \sum_l (X_f^{*,l} X_f^l + Y_f^{*,l} Y_f^l) \tag{2.2.12}$$

where θ_{XY}^j denotes the cross phase of the signals for the two electrodes separated by Δx along the field line.

Another method of obtaining $k_{\parallel}$ is to find the position where the correlation becomes maximal by moving the position of one of the electrodes, using the fact that the correlation length parallel to the magnetic field line is much longer than perpendicular one.

The estimated variance of wavenumber (i.e., spectral width) σ_k can be derived from cross coherence [60],

$$\sigma(\omega) = \left\langle (\bar{k} - k)^2 s(k, \omega) \right\rangle^{1/2} = \left\{2(1 - C_{xy}(\omega))\right\}^{1/2}/\Delta x. \tag{2.2.13}$$

The fundamental angular frequency (i.e., frequency resolution) is expressed as $\Delta\omega = \pi/T$, for a given time window of T. The number of time sample of the fluctuations for the time window is N, and the sampling interval $\delta t = T/N$ must be short enough so that the Nyquist frequency $\omega_N = \pi/\delta t$ becomes greater than the highest frequency of interest. Similarly, the probe separation Δx must be small enough so that $\pi\Delta x$ becomes greater than the highest wavenumber of interest.

Chapter 3

Experimental device

3.1 TST-2 spherical tokamak

The Tokyo Spherical Tokamak -2 (TST-2) device [61] was constructed at the University of Tokyo. TST-2 is now located at the Kashiwa Campus. The photograph of TST-2 is shown in Fig. 3.1.1. TST-2 has the following typical parameters for Ohmic discharges: major radius $R \leq 0.38$ m, minor radius a ≤ 0.25 m and aspect ratio $A = R/a \geq 1.5$. The aspect ratio is low enough, and the TST-2 device is classified as a spherical tokamak. 24 toroidal field (TF) coils, a 239 turn Ohmic (OH) heating center solenoid (CS) and 5 pairs of poloidal field (PF) coils are installed in TST-2 (Fig. 3.1.2). The TF coils generate a toroidal magnetic field $B_T \leq 0.3$ T. The PF coils are used to control the position and shape of plasma. For pre-ionization of gas, we use a magnetron (2.45 GHz / 5 kW). The discharges can be classified into the following four types: Ohmic discharges, the electron cyclotron heating (ECH) discharges, ECH + radio frequency (RF) heating and OH + RF heating discharges. In Ohmic discharges, plasma is heated by joule heating using the inductive electric field from the CS. Plasma current I_p of about 100 kA and discharge duration t_{pulse} of about 30 ms are typical values. In ECH discharges, a plasma is generated and sustained noninductively by ECH alone. Plasma current I_p of about 1 kA and discharge duration t_{pulse} of about 100 ms are typical. In ECH + RF discharges, a lower hybrid wave (200MHz) with the maximum power of 100kW is injected to ECH discharges and I_p reaches about 20 kA. In this study, Ohmic discharges are studied, because of the high plasma currents.
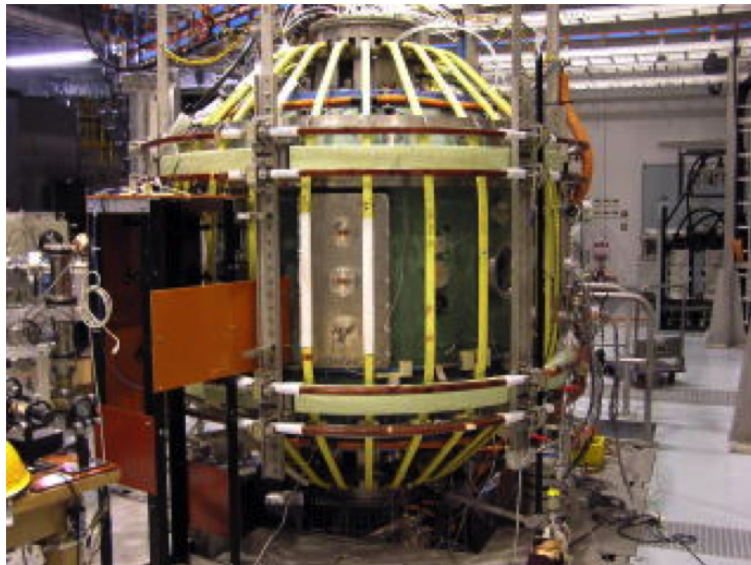
Figure 3.1.1: Photograph of TST-2.
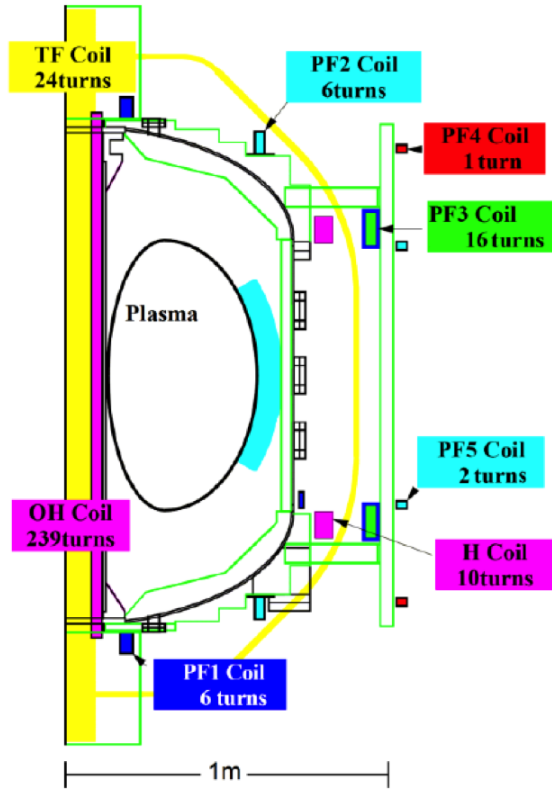
Figure 3.1.2: Schematic diagram of the coils on TST-2.

3.2 Heating

3.2.1 Electron cyclotron heating

The electrons follow a spiral path along a magnetic field line. The electron gyration frequency around the field line is called (electron) cyclotron frequency. When the electron cyclotron wave, which has the same frequency as the cyclotron frequency, is injected to the plasma, the energy of the wave is resonantly absorbed by the electrons. This process is called electron cyclotron heating (ECH). On TST-2, a magnetron (2.45 GHz / 5 kW) is used to inject the EC wave.

3.2.2 Radio frequency heating

Waves can propagate in plasma when they satisfy one of the dispersion relations. Energy absorption by plasma particles occurs when such waves reach a resonance layer. This process is called Radio Frequency (RF) heating. On TST-2, lower hybrid waves (200 MHz/400 kW) is available.

3.3 Diagnostics

3.3.1 Composite probe system

Figure 3.3.1 shows the head of the composite probe system and the typical assignments of the electrode usage in this experiment. This system is composed of Langmuir probe arrays and a 3 axis magnetic pickup coil. The Langmuir probe arrays consist of 8 electrodes made of molybdenum. Four of them are located at the front of the probe head, and can be used to measure the wavenumber of fluctuations. The diameters of these electrodes are 1 mm, and the heights are $1 \sim 1.5$ mm. The four electrodes are separated by about 10 mm. The detailed design drawing of this probe is shown in Appendix. These electrodes were used to measure the floating potential fluctuation $\tilde{V}_f$ when they are unbiased. The applied bias voltage for each electrode can be swept to obtain the V-I characteristics, and the electron density, the electron temperature and the plasma potential are calculated from

it. When we assume that the electron temperature fluctuation is negligible, the fluctuating floating potential $\tilde{V}_f$ represents the fluctuation of the plasma potential. One of the front four electrodes protrudes from the others by 10 mm and its foot is covered with a ceramic tube, and it is used to measure radial wavenumber. The usage of the four electrodes varies according to experiments. When the objective of the experiment is to measure the plasma flow, the other four electrodes located at the side of the probe are used to measure the ion saturation current, and the plasma flow is obtained by using the mach probe method, as described in Sec. 4.5. These electrodes can also be used for the measurement of floating potential and plasma potential fluctuations.

A 3-axis magnetic pickup coil is located inside the composite probe. The size of the pickup coil is 10 mm × 6 mm × 6 mm. We can measure poloidal, toroidal, and radial magnetic field fluctuations simultaneously. Figure 3.3.2 shows the photograph of the 3-axis pickup coil. The composite probe is covered with boron nitride sheath, which can endure the high heat flux and the bombardment of high energy plasma particles. The calibration of each coil is conducted using a helmholtz coil outside the vacuum vessel, and using a reference discharge without plasma. Cross talk among the pickup coil signals is up to ~ 2%, which is negligibly small. If there is some obstacle neighboring the electrodes, the measured floating potential could be affected significantly due to the shadowing effect of plasma flow [62]. To avoid the effect of the protruded electrodes on the other electrodes, the composite probe system is rotated using a rotary stage. By choosing the angle carefully, the arrangement of the electrodes is adjusted so that the protruded ceramic tube is not in the upstream side of the other electrodes. The probe system can also be moved poloidally using a bellows joint up to ±15°, so that we can scan the poloidal location of the probe system on shot by shot basis.

Figure 3.3.3 shows the probe tip geometry and the usage of the electrodes of the composite probe (probe 2) and the definitions of coordinates in the radial scanning experiments. E_θ, E_r were derived from the phase difference between V_{f1}, V_{f2} and V_{f3}.
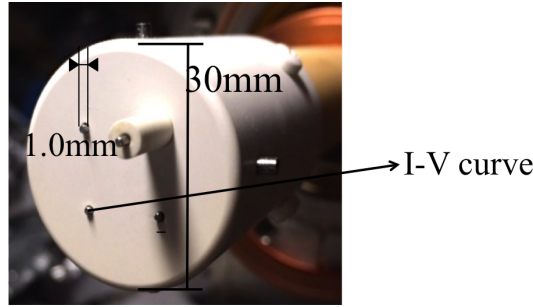
Figure 3.3.1: Photograph of the composite probe head and the electrode used to measure V-I curves.

3.3.2 Measurement of electron temperature fluctuation by fast sweep voltage method

As mentioned in Sec. 2.1.1, plasma potential V_p is often evaluated by V_f, neglecting the effect of temperature fluctuation. Thus, the local electric field fluctuation is usually evaluated by the difference between V_fs at two adjacent points separated by 10 mm [63], and more accurate estimation using V-I curves is limited so far [64]. The floating potential V_f is a function of the plasma potential V_p and the electron temperature T_e via

$$V_f = V_p - \alpha T_e, \qquad\qquad \alpha \equiv \log I_{es}/I_{is}. \qquad\qquad (3.3.1)$$

Here, I_{es} is the electron saturation current and I_{is} is the ion saturation current. Electron temperature fluctuations are usually considered to be negligible compared to the plasma potential fluctuation in a toroidally confined low temperature plasmas [65]. However, in high-beta plasmas like spherical tokamak (ST) plasmas, this assumption is not guaranteed, and may lead to an erroneous result. Therefore, we measured electron temperature fluctuation in the TST-2 edge plasma to investigate its influence on the potential fluctuation measurement by using the fast sweeping method developed in a preceding work [66][67]. In addition, we have tested the validity of the T_e measurement by comparing the V_f fluctuations measured by the fast sweeping method and that obtained by the standard method.
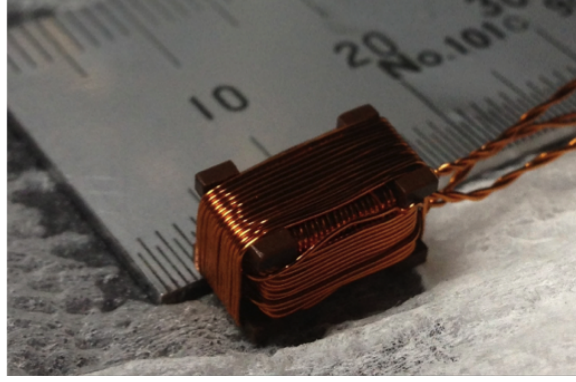
Figure 3.3.2: Photograph of the 3-axis pickup coil.
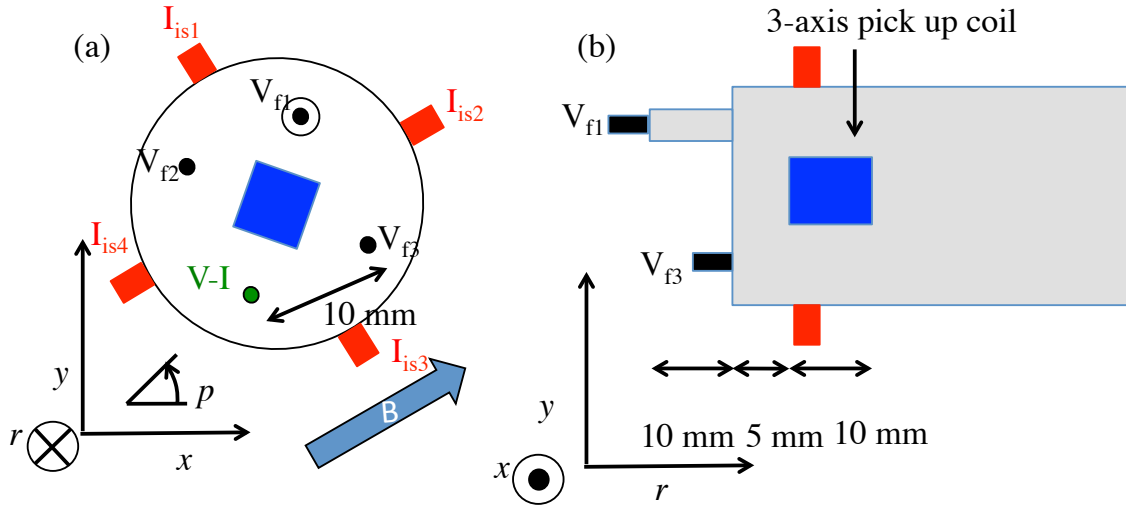
Figure 3.3.3: The probe geometry and the usage of electrodes of the composite probe (probe 2) and the definitions of coordinates. Head-on view of the probe head from the high field side to the low field side (a), and the sideview (b) are shown.

3.3.3 Distortion of characteristic curve by contamination

After a vacuum opening of TST-2, the V-I characteristic curve becomes distorted as shown in Fig. 3.3.4 (a). The slope of the ion saturation becomes negative, and the ion saturation current has a maximum at $V_f - 20 \sim V_f - 50$ V. I_{is} is fitted with light blue lines, and the exponential part of the V-I curve is fitted with red curves in Fig. 3.3.4, and the negative slope deteriorates the accuracy of measurements. There are two main possibilities to distort the V-I curve. One is the effect of contaminated surface adding a stray capacitance on the electrodes. The other is the effect of secondary electron emission from the electrode surface. Since the distortion in the V-I curve does not depend on the sweep frequency of the bias voltage, the former possibility is excluded, and the latter seems to be the dominant mechanism. Figure 3.3.4 (b) shows the data after about 100 discharges from the vacuum opening and the V-I characteristic curve becomes normal.

Since the sweeping frequency is relatively high, the effect of capacitive current due to the coaxial cables of the signal transmission line cannot be neglected. Therefore, the capacitive current is subtracted from the raw probe current. We estimate the capacitive current from the derivatives of the voltage data, and the estimated current is subtracted from the raw probe current. Due to the subtraction, the hysteresis of the V-I curves disappeared. Figure 3.3.5 (a) shows the comparison between the estimated capacitive current (red) and the raw probe current (black) without plasma production. Good agreement between the two waveforms is observed, and validity of the estimation and subtraction is confirmed. The subtraction with plasma is demonstrated in Fig. 3.3.5 (b), where the raw probe current (blue curve) and corrected current (red curve) are overplotted. The V-I curve shows almost no hysteresis after the subtraction, and the error in temperature due to the hysteresis
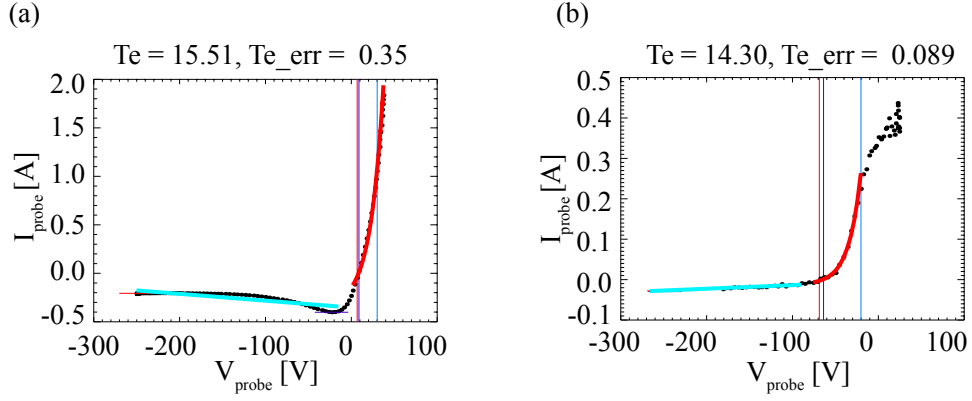
Figure 3.3.4: V-I characteristic curve acquired by a contaminated electrode after a vacuum opening of TST-2 (a) and that after about 100 discharges (b). I_{is} is fitted with light blue lines, and the exponential part of the V-I curves are fitted with red curves. The vertical light blue lines represent V_p, and the red lines represent V_f derived from fitted V-I characteristic.

becomes much smaller than those introduced by the discrete sampling (5 μsec in this case). The validity of the data is confirmed by comparing the time evolution of floating potential V_fs and that calculated from V-I curve (Fig. 3.3.6 (a)). A good agreement is observed and the difference between them is within the error bars. From the fitted curve on a V-I curve, electron temperature and its fluctuation are evaluated. The data used in the fitting are the region in the vicinity of the floating potential where the electron current collected from the plasma is smallest. Fluctuation amplitudes of T_e are about 10 eV, whereas the averaged T_e is 20 eV, and fitting errors of the electron temperature are less than 3%. The fluctuation level of T_e is about 50 %. On the contrary, the V_f fluctuation amplitude is 50 V, and if the value of α in Eq. (3.3.1) is taken to be 3, the fluctuation level of V_f due to $\tilde{T}_e$ becomes about 30 V. Thus, T_e fluctuation level can be more than half of that of V_f. This indicated that the plasma potential fluctuation should not be calculated only by the floating potential fluctuation. However, if the temperature fluctuations do not have wavenumbers comparable to those of space potential, their effect to electric field fluctuation is cancelled. Furthermore, if the fluctuations are not correlated the effect becomes smaller due to the square summation effect. Thus, the actual effect of the temperature fluctuation on the electric field measurements by using floating potentials is probably much smaller than 50 %.

The plasma potential is also evaluated from the inflection point of the V-I curve at the electron saturation current side. Figure 3.3.7 shows an example of V-I characteristic curve with a linear and a logarithmic scales. The inflection point is evaluated from the extrapolations of the electron saturation and the maxwellian electron retarding curve.

The coefficient α (used in Eq. (3.3.1)) was estimated to be 3.26. This does not contradict the recent study where $\alpha = 2.94$ [67] [68]. These experimental and analysis results indicate that full V-I curve can be used even when the bias voltage is swept very quickly.

Electron temperature fluctuations were measured by using the fast voltage sweeping method in the edge of the TST-2 spherical tokamak plasmas. The validity of fitting is evaluated by comparing V_fs acquired by V-I curve fitting and by high impedance resistor independently. The fluctuation level of T_e may not be negligible in evaluating the plasma potential fluctuation. The plasma potential fluctuation is also evaluated by the inflection point in the V-I curve. The coefficient α in $V_p = V_f + \alpha T_e$ derived from the V-I curve agrees with the values in the previous experimental and theoretical studies.
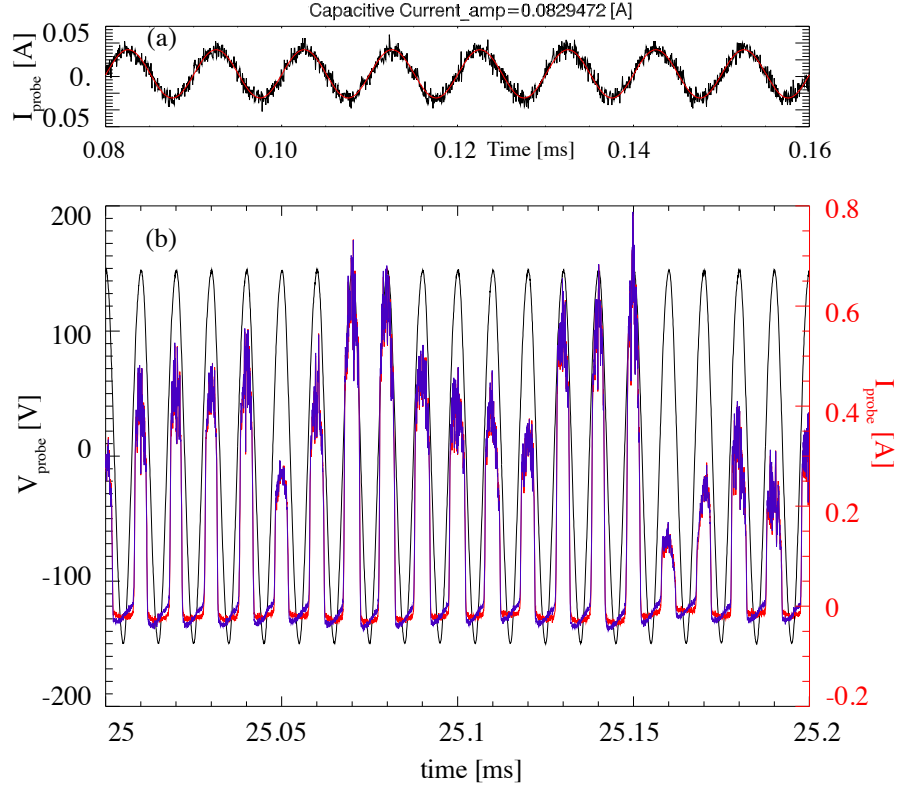
Figure 3.3.5: The raw (black) and the corrected (red) probe current without plasma (a), and the time evolutions with plasma (b). The swept bias voltage (black), raw probe current (blue) and corrected probe current (red) are shown in (b).
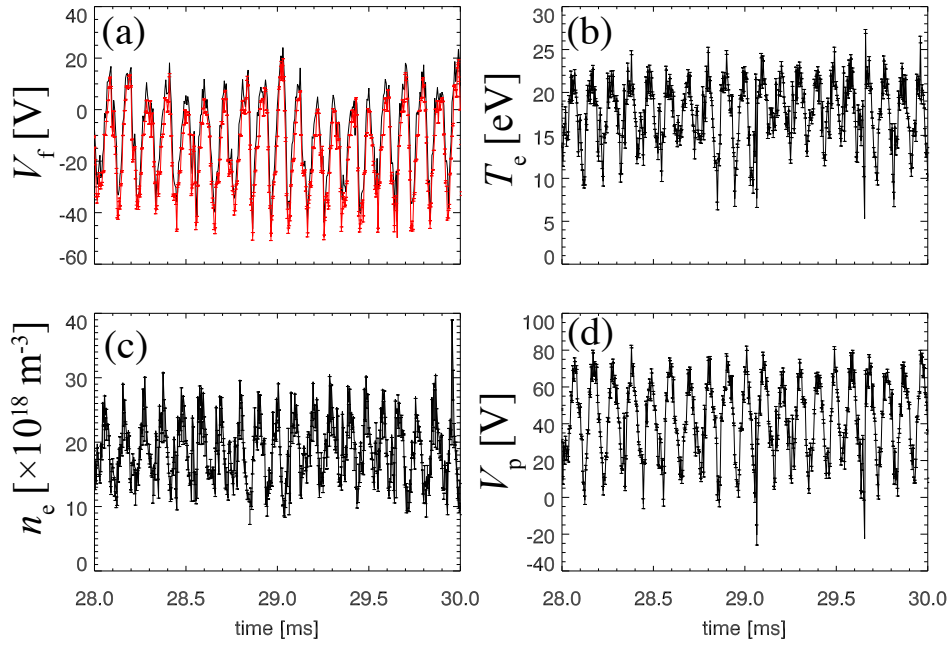
Figure 3.3.6: Waveforms of raw V_f (black) and V_f calculated from V-I curve (red) (a) and T_e(b), n_e (c), and V_p (d) calculated from the inflection point of the V-I curve.

30
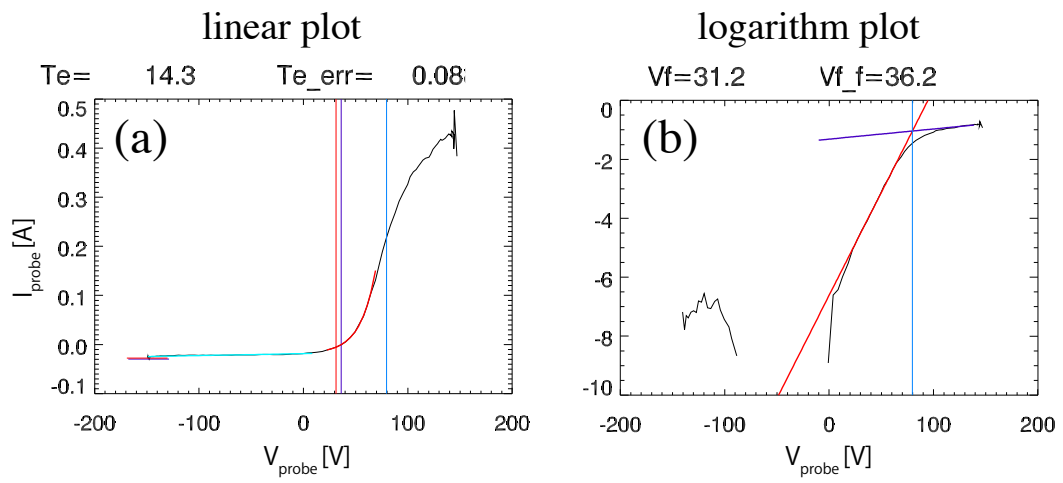
Figure 3.3.7: Example of V-I curve with a linear vertical scale (a) and with a logarithm vertical scale (b).

3.3.4 Upper and lower side probe systems

In order to cover a wide area in the outboard (weak field) side region, two additional Langmuir probe systems have been installed at the location 90° apart in toroidal angle from the composite probe (probe 2) as shown in Fig. 3.3.8. By choosing appropriate positions of the probes we can measure two spatial points on a same field line simultaneously. This is quite useful to study the features of turbulence along a field line.
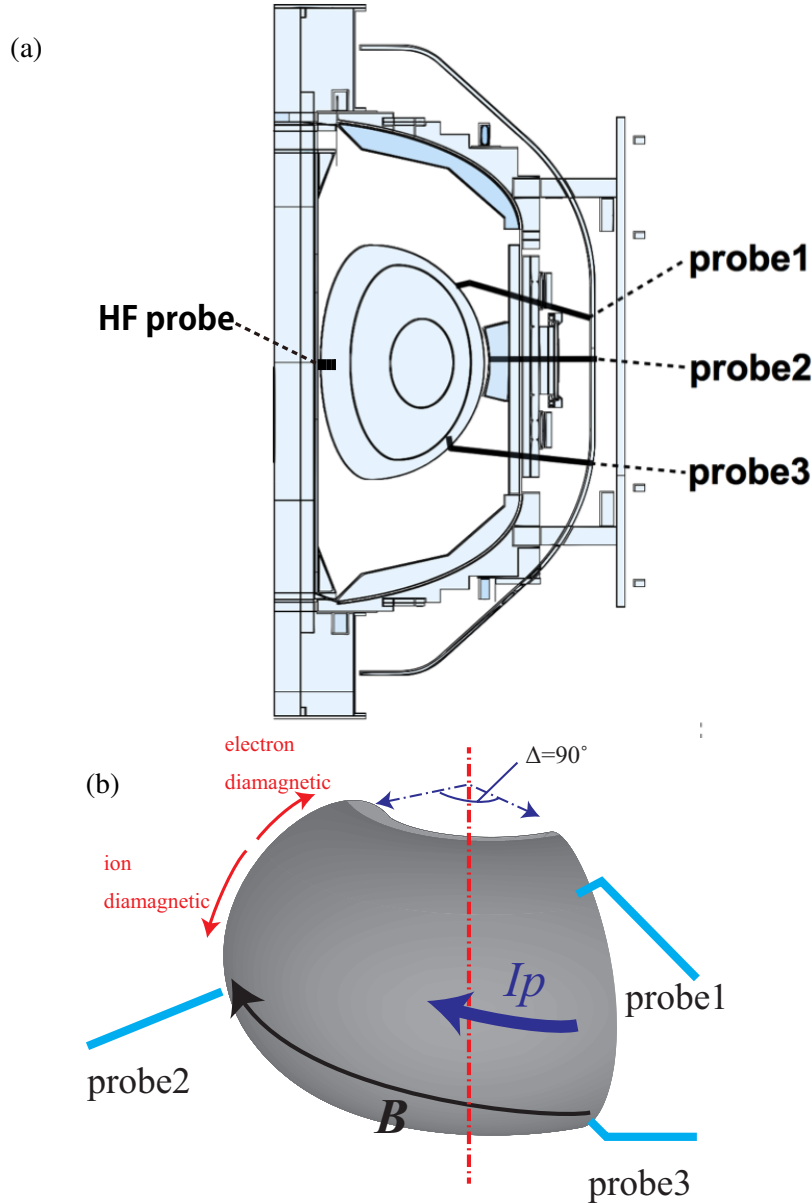
Figure 3.3.8: Locations of the probe systems in TST-2. Probe 1, probe 2 and probe 3 are movable radially and poloidally to measure two-dimensional profiles. The high field side probe (HF probe) is fixed at the inboard wall of the vacuum vessel. The arrangement of the probes projected on a poloidal cross section (a) and a schematic 3-D view of the probes (b) are shown. In this figure, probe 2 and probe 3 measure the points on a same field line. The composite probe is denoted as probe 2.

Figure 3.3.9 shows the Langmuir probe located at the upper side of the outboard of TST-2. Each of these probes has four cylindrical electrodes made of tungsten with diameters of 0.5-1.0 mm and heights of 1.5-2.0 mm. Three of the electrodes are devoted to floating potential and the remaining one is devoted to ion saturation current measurements. Each of these systems is used to confirm the reproducibility of discharges. They are also used to measure the (long range) correlation between the signals of these probes and the composite probe signal. The probe system at the upper side is called probe 1, and the other probe system at the lower side is called probe 3 in this experiment (Fig. 3.3.8).
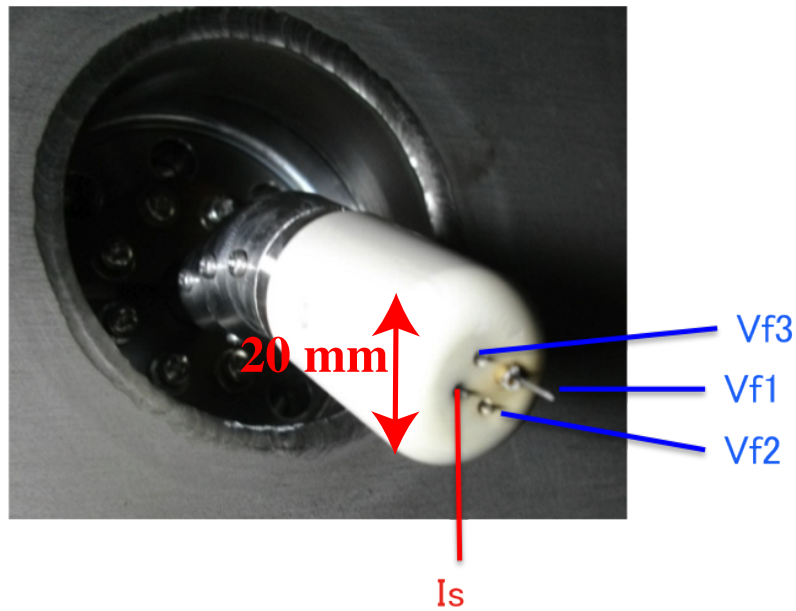
Figure 3.3.9: Enlarged photograph of probe1.

3.3.5 High field side probe

Figure 3.3.10 shows the Langmuir probe located at the midplane of the inboard (i.e., high field) side wall. It has one molybdenum electrode with a diameter of 2 mm, and the height is 5 mm. By comparing the signals measured by this probe and those measured by the outboard probes, we can study the inboard outboard asymmetry, which may be significant in ST plasmas.
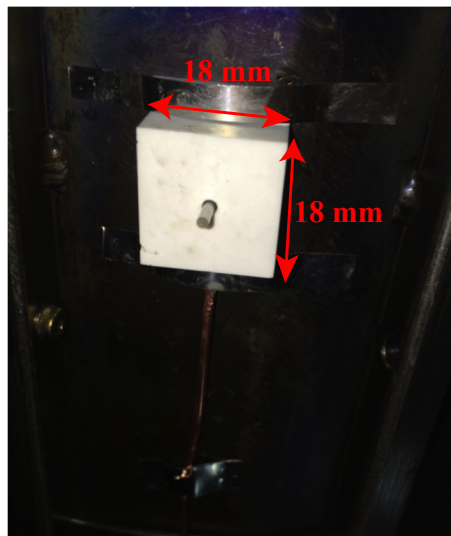
Figure 3.3.10: Enlarged photograph of the high field side probe.

Chapter 4

Experimental result

4.1 Device setup

Mainly three probe systems described in Chap. 3 were used in the experiments. The composite probe (probe 2) is located on the midplane, and can be moved in the radial and poloidal directions. Two other probe systems (probe 1 and probe 3) are used to check discharge reproducibility, and to see long distance correlation along a magnetic field line. There are 4 electrodes on the front surface. One electrode is used to obtain V-I characteristics by applying a sinusoidal voltage of -150 to +150 V at 100 kHz. We measure the probe current at the shunt resister and the voltage at the exit of the vacuum feedthrough by using an Analog-Digital Converter (ADC) (8861-50 manufactured by HIOKI E.E. corporation, Japan). The length of the cable is 1 m for both, and the noise is reduced by a cable drive technique. The ADC unit has 16 channels, and can measure a voltage up to 400 V. The maximum sampling rate is 20 MHz. The other electrodes are used to measure floating potentials (V_fs). Each V_f signal is terminated by a 1 M Ω input impedance of the ADC. The current and voltage waveforms of the V-I characteristic are directly sampled by isolated ADCs with a sampling rate of 20 MHz . The measurement timing delay between the current and the voltage signals is negligible.

We set the radial location of the composite probe at $R = 550 - 650\,\text{mm}$, while the outboard limiter is located at $R = 585\,\text{mm}$. We analyzed only the data when the plasma was bound by the outboard limiter, so that the ambiguity of the LCFS position (~ 585 mm) is minimized.

4.2 Discharge evolution

We selected the Ohmic discharges with high I_ps and long plasma durations to acquire stable fluctuations of various parameters.

Figure 4.2.1 shows typical waveforms of a discharge. I_p, line integral density n_eL, H_α emission, radiation signals measured by a photodiode (IRD, Absolute X-Ray Photodiode AXUV), soft X-ray emission measured by a surface barrier diode (SBD). Right figures show information on the shape and position of the plasma. R_{maxis} and Z_{maxis} are the radial and vertical positions of the magnetic axis. L_{gap} is the distance between the inboard limiter and the LCFS, and R_{gap} is the distance between the outboard limiter and the LCFS. R_{out} is the outboard radial position of the LCFS. B_T is ~ 0.2 T in the clockwise direction. I_p is 70 kA at 30 ms. At around 32 ms, strong spikes in the signals are observed and the plasma disrupted accompanying large bursts in H_α, AXUV and SBD signals. This event is called Internal Reconnection Event (IRE) relaxation phenomenon characterized by a collapse of the pressure and plasma current profiles.

Figure 4.2.2 shows the equilibrium configuration calculated by EFIT [69] for this discharge. The analysis timing is 30 msec, when I_p has a maximum value of 70 kA. We analyzed the time window around 27 ms $\sim$ 31 ms, in which the line integrated density, R_{out} and Z_{maxis} are roughly constant. At this timing, the LCFS was determined by the outboard limiter located at $R = 585$ mm. The red contour shows the shape of the LCFS. Profiles of pressure, diamagnetic term (FF' term), q and current density are also plotted.

Figure 4.2.3 shows the radial profiles of T_e, n_e, V_f and V_p in the edge region measured by the composite probe. Error bars in the figures indicate the rms fluctuation amplitude of each parameter. T_e shows roughly constant value of $\sim 20\,\text{eV}$ inside the LCFS to $R \sim 620$ mm, 35 mm outside the limiter, and decreases in the outer edge region. The fluctuation amplitude of T_e is also constant at $R < 620$ mm. On the other hand, n_e

monotonically decreases with R across the LCFS, and the fluctuation amplitude also decreases. V_f and V_p show constant values inside the LCFS, and increase almost monotonically toward $R = 640$ mm. This suggests the presence of radial electric field outside the LCFS. For V_f and V_p, we plotted data obtained by different methods. The good agreement in V_fs indicates the correctness of the measurements. The systematic deviation between V_ps is probably due to the large error in the determination of inflection point in V-I characteristics.

Figure 4.2.4 shows the time evolution of the power spectrum of $\tilde{V}_f$ at $R = 550$ mm. Two types of coherent fluctuation are observed during 27 ms ~ 31 ms. One is the peaked power at about 10 kHz and the other is that around 70 kHz. The former is accompanied by magnetic fluctuations and seems to be generated by MHD instabilities. It can be seen that the fluctuation levels do not change significantly during 27 ms ~ 31 ms, indicating that the time window is appropriate. Figure 4.2.5 shows the contour of the time derivative of poloidal magnetic signals dB_θ/dt measured by poloidal coil arrays fixed at the wall of the vacuum vessel. This shows that the MHD fluctuations of 10 kHz are large at the low field side, and the poloidal mode number is ~ 2. On the other hand, the sinusoidal pattern is not evident in the high field side, showing the characteristics of the ballooning type fluctuation [70], where the fluctuation amplitudes are large at the outboard region and small at the inboard region.

Figures 4.2.6 (a), (b) show the contour of power spectrum of V_f and I_{is}. An MHD peak at 10 kHz and a peak around ~ 70 kHz are observed around 590 mm, which is close to the LCFS position. Well outside of the LCFS, the power spectrum does not show distinct frequency other than the 10 kHz peak, and decays smoothly (Figs. 4.2.6 (c), (d)). The ion saturation current I_{is} also shows a similar profile. The power of the MHD fluctuation of V_f was distributed uniformly along R, while at the frequencies higher than 70 kHz the power outside the LCFS is one order of magnitude smaller than that inside the LCFS.

In TST-2, the magnetic fluctuation level is significant in Ohmic discharges. Figures 4.2.7 (a), (b) show the contour of power spectrum of B_r and B_p. B_r and B_p show similar spectra, and there is no specific peak other than 10 kHz in the magnetic fluctuations. Figure 4.2.7 (c) compares the spectra of V_f and B_r at $R = 590$ mm. The absence of the peak at ~ 70 kHz in B_r agrees with the characteristic of drift wave. Figure 4.2.8 shows the radial profile of the rms fluctuation levels of $\tilde{B}_r/B_T$, $\tilde{B}_p/B_T$ and $\tilde{B}_t/B_T$ at 10 kHz. Error bars in the figures indicate the shot by shot scatter of each parameters. The fluctuation levels are $\tilde{B}_r/B_T \sim 10^{-2}$, $\tilde{B}_T/B_T \sim 10^{-3}$, and these levels are one order greater than those of conventional tokamaks [71]. These levels are similar to those observed in RFP plasmas [72]. The fluctuation levels are distributed relatively uniformly across the LCFS, while those in conventional tokamaks decay outside the LCFS.
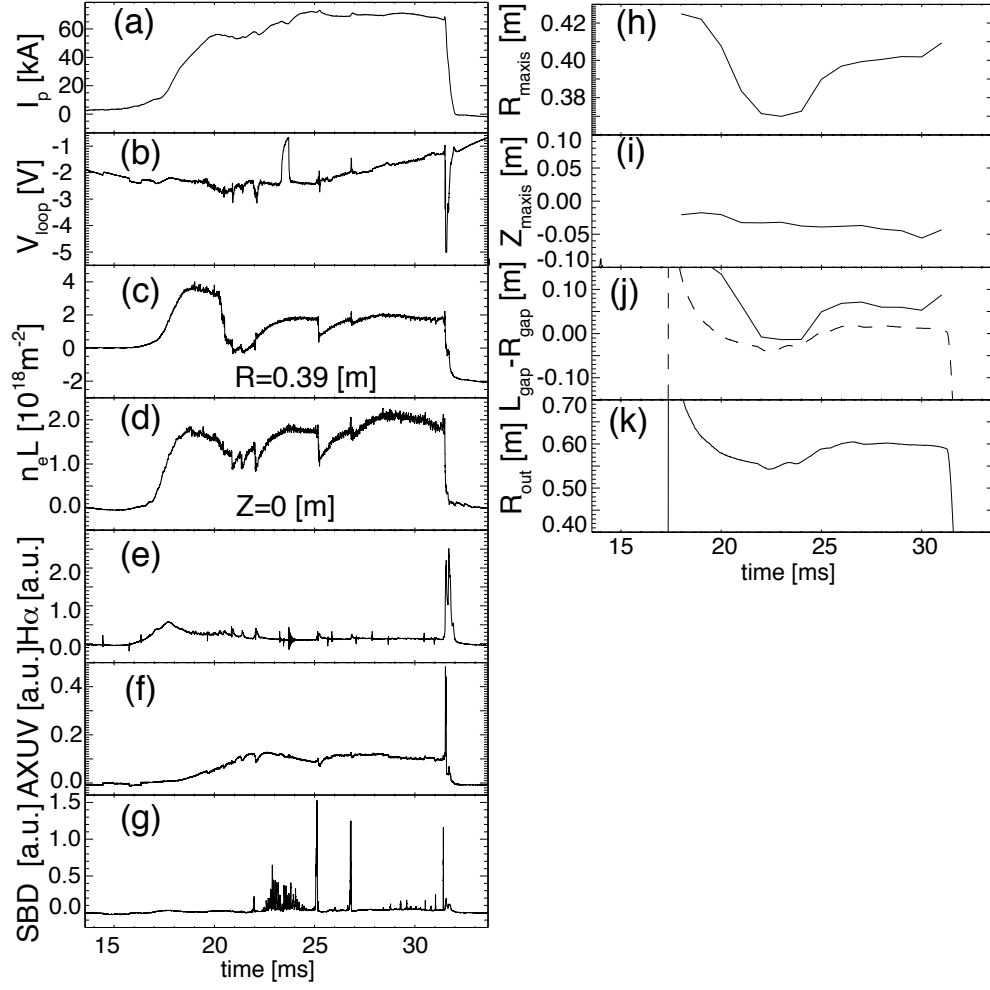
Figure 4.2.1: Waveforms of an Ohmic discharge. I_p (a), loop voltage V_{loop} (b), n_eL measured by interferometers (c) (d), H_α emission (e), AXUV signal (f), SBD signal (g), radial and vertical coordinates of the magnetic axis R_{maxis} (h) Z_{maxis} (i), radial distance between R_{out} and the outboard limiter R_{gap}, and radial distance between the LCFS and the inboard limiter (dashed curve) (j) and R_{out} (k) are plotted.

36
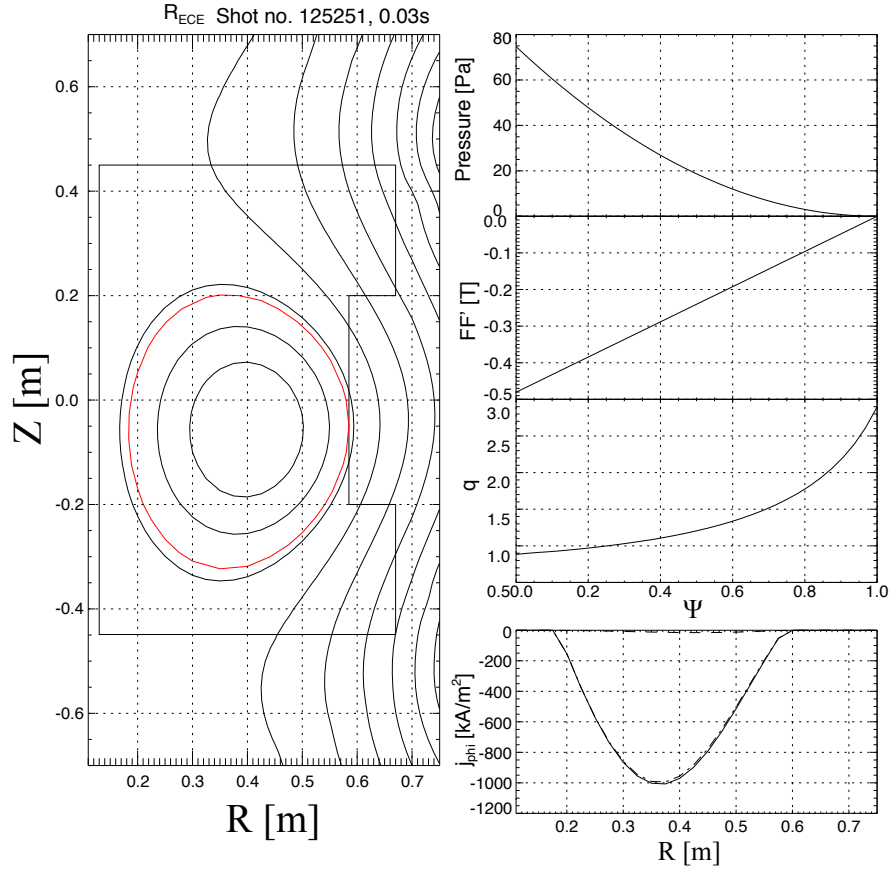
Figure 4.2.2: Typical equilibrium configuration calculated by EFIT. Analyzed timing is 30 msec, when I_p has a maximum value of 70 kA. Contours indicate the surfaces of poloidal flux function ψ, which represents the shape of the flux surfaces. The red contour indicates the last closed flux surface limited by the outboard limiter at $R = 585$ mm. Right figures show pressure, FF', q against the normalized flux function ψ. The right bottom figure shows the current density at the midplane as a function of R (i.e., major radius).
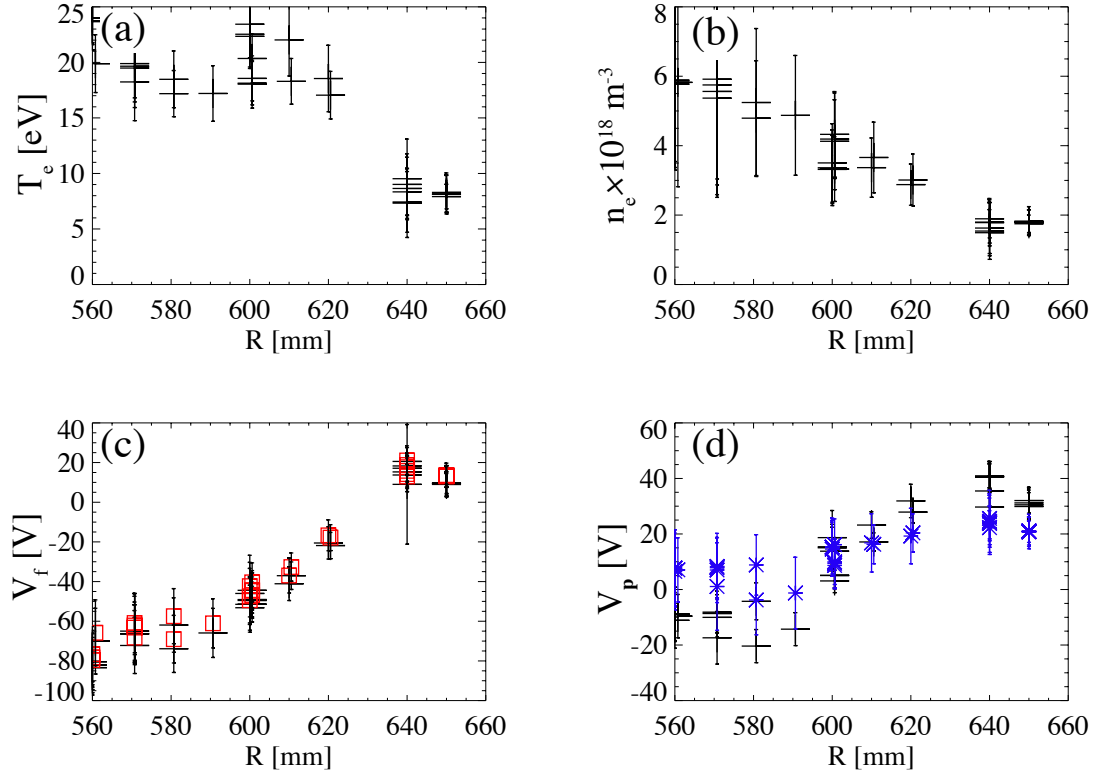
Figure 4.2.3: Radial profiles of T_e (a), n_e (b), V_f (c) and V_p (d) measured by the composite probe system. In (c), the black symbols are V_{f2} and the red symbols are V_fs derived from V-I curve. In (d), the black symbols are V_p derived from $V_f + 2.94T_e$ and the blue symbols are V_p derived from the inflection point of V-I curve.
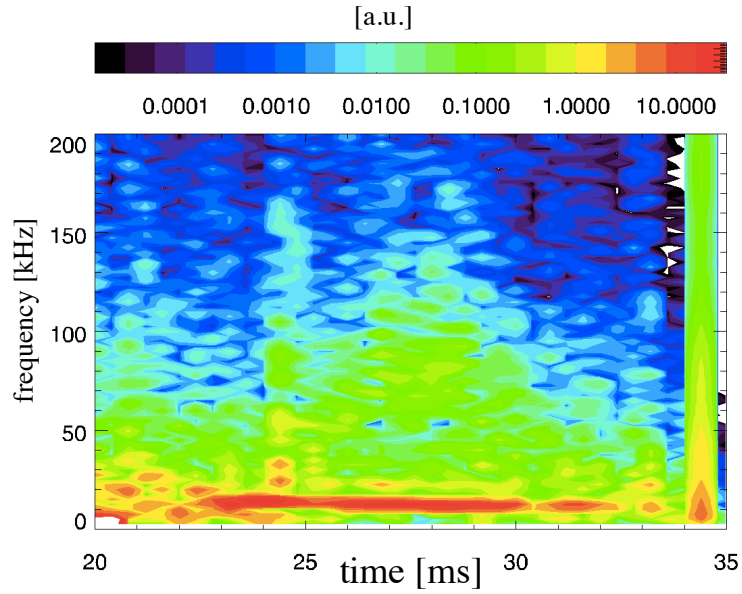
Figure 4.2.4: Time evolution of power spectrum of $\tilde{V}_f$ measured by the Langmuir probe located at $R = 550$ mm. Spectrum is calculated using FFT with a time window of 0.5 msec.
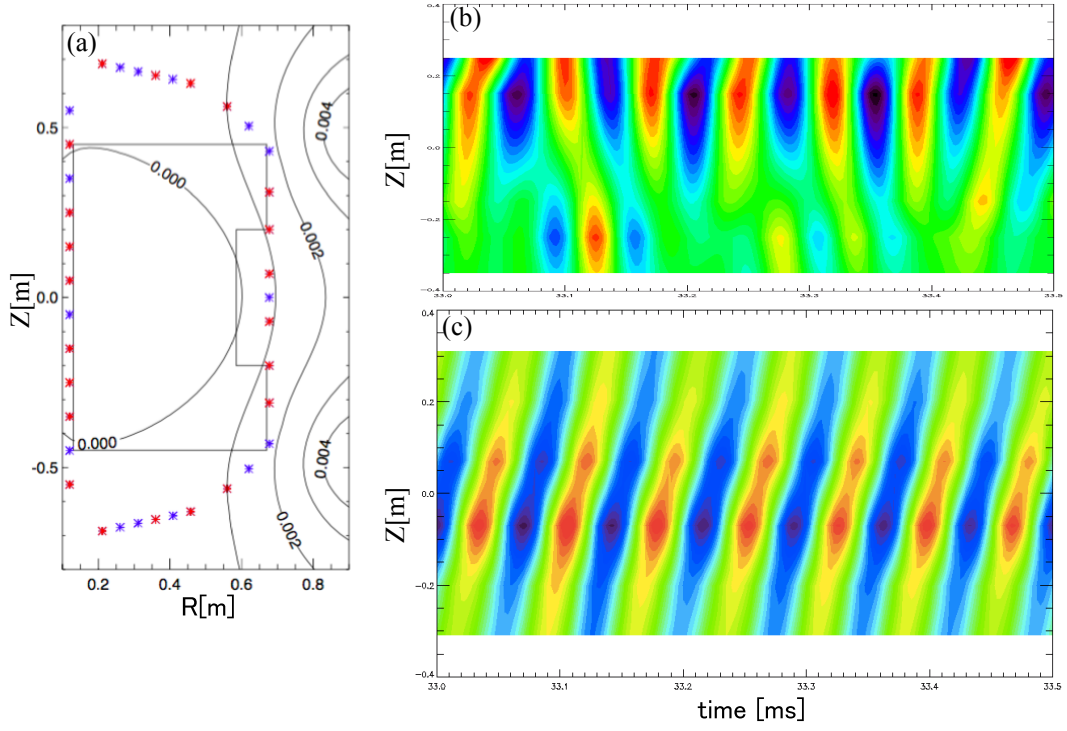
Figure 4.2.5: Locations of the magnetic pickup coils to measure the poloidal structures (a) and time evolution of the inboard (b) and the outboard (c) magnetic fluctuations.
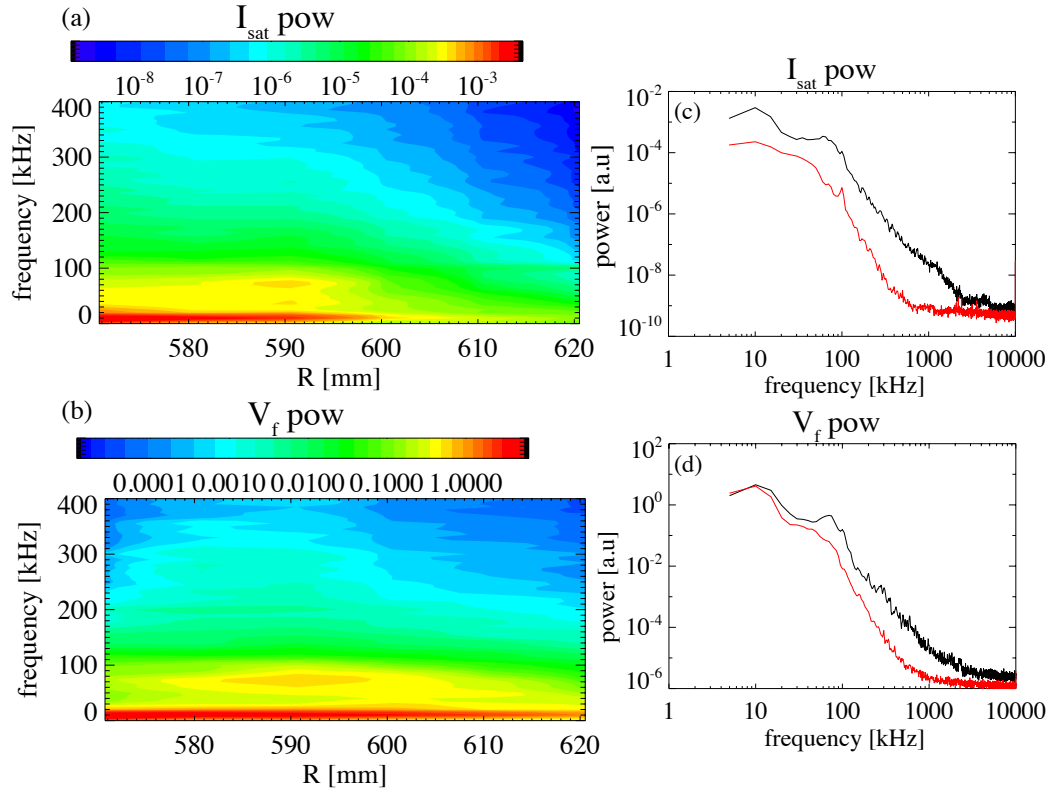
Figure 4.2.6: Color contour plot of the power spectra of I_{is} (a) and V_f (b). MHD components at around 10 kHz can be seen in the whole region, and a peak around 70 kHz is observed around $R = 590$ mm. Power spectra for I_{is} (c) and V_f (d) at $R = 590$ mm (black) and $R = 620$ mm (red) are also plotted.
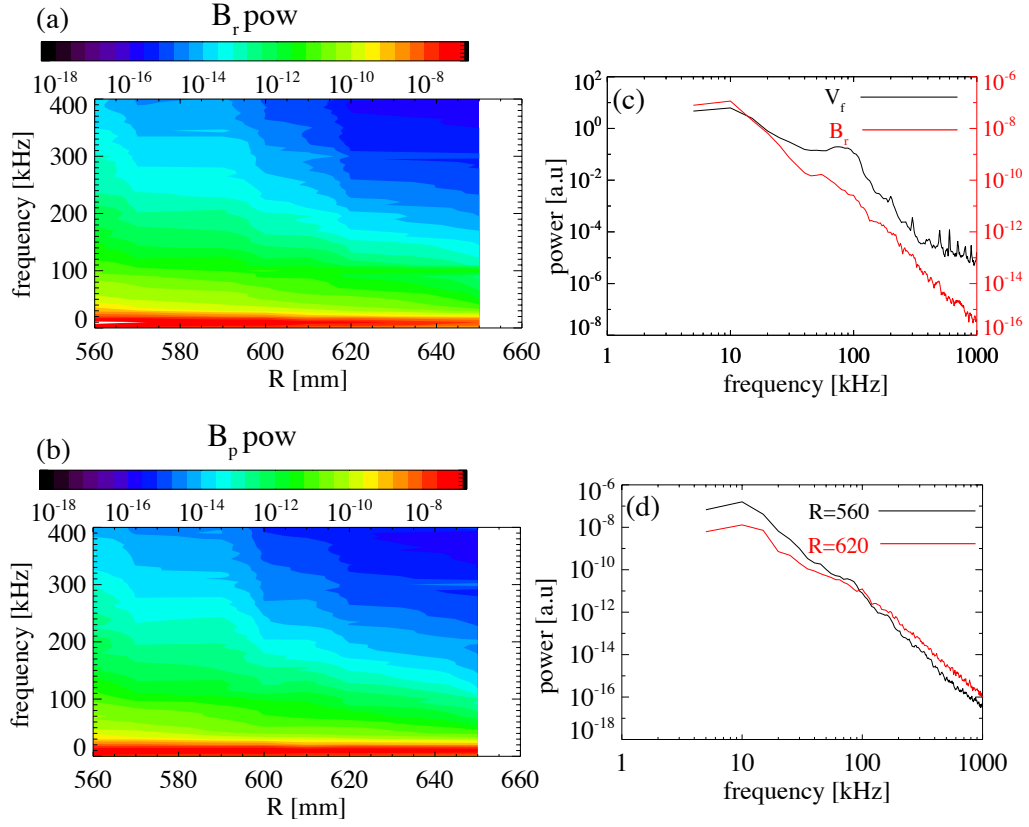
Figure 4.2.7: Color contour plot of power spectrum of $\tilde{B}_r$ (a) and $\tilde{B}_p$ (b). The magnetic fluctuation does not have specific peaks other than 10 kHz. Power spectra for $\tilde{V}_f$ (black) and $\tilde{B}_r$ (red) at $R = 590$ mm (c) and those for $\tilde{B}_r$ at $R = 560$ mm (black) and $R = 620$ mm (red) (d) are also plotted.
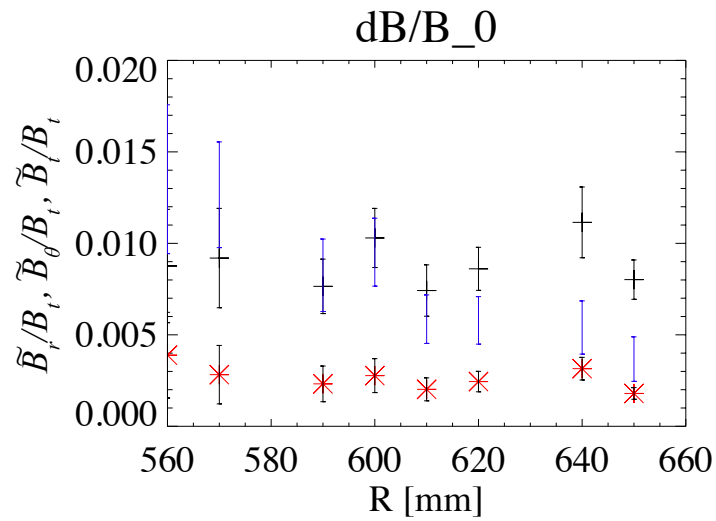
Figure 4.2.8: Radial profiles of the normalized fluctuation amplitudes $\tilde{B}_r/B_t$ (black), $\tilde{B}_\theta/B_t$ (blue) and $\tilde{B}_t/B_t$ (red) for the frequencies around 10 kHz.

4.3 Two dimensional turbulence measurement

Since the parallel correlation length is very long (as shown later), the spatial structure of the turbulence can be approximated by a 2D structure with coordinates poloidal and radial. The electric field, which is an important quantity in the electrostatic transport, is the gradient of the plasma potential. Since the distances between the probe electrodes are sufficiently short, the gradient can be approximated by the difference of measured potentials at different positions. Figure 4.3.1 shows an example of the phase difference between V_{f2} and V_{f3} when the composite probe is rotated in the poloidal-toroidal plane. The phase difference at 100 kHz shows a clear sinusoidal curve. This result implies that there is no systematic time delay peculiar to each electrode. When the probe is inserted to the plasma with the angle perpendicular to the flux surface, the poloidal electric field fluctuation can be obtained as

$$\tilde{E}_\theta = -(V_{f2} - V_{f3})/d_{\theta 23} \,, \tag{4.3.1}$$

and the radial electric field as

$$\tilde{E}_r = -(V_{f1} - (V_{f2} + V_{f3})/2))/d_r - \tilde{E}_\theta \frac{d_{\theta 12} + d_{\theta 13}}{2d_r} \,, \tag{4.3.2}$$

where V_{f1} is the V_f signal from radially protruding electrode 1 (see Fig. 3.3.3), $d_{\theta 12}$ is poloidal distance between the electrodes 1 and 2, d_r is radial distance between electrode 1 and 2. The effect of temperature fluctuation to $\tilde{V}_f$ is neglected here. When the composite probe system is tilted against the plasma flux surface, Eqs. (4.3.1) and (4.3.2) are not accurate because the tip locations are not orthogonal with respect to the the flux surface, and some correction is needed.

As described in Sec. 2.2, the temporal and spatial structure of the turbulence can be represented by local $S(k, \omega)$. For a given k, the gradient can be obtained by multiplying k. When we want to obtain k-space averaged electric field for a given ω, we should calculate the average k for the ω. The relationship between the calculated cross phase and the wavenumbers k_r and $k_\perp$ are given by the equation.

$$\boldsymbol{k} \cdot (\boldsymbol{r}_1 - \boldsymbol{r}_2) = s_{12} \,, \qquad\qquad \boldsymbol{k} \cdot (\boldsymbol{r}_2 - \boldsymbol{r}_3) = s_{23} \,, \tag{4.3.3}$$

where s_{12} is the cross phase difference between V_{f1} and V_{f2}, s_{23} is that of V_{f2} and V_{f3}, and $\boldsymbol{r}$ is the location of each electrode. When $k_\parallel \ll k_r, k_\perp$, these equations are expressed as

$$\begin{pmatrix} s_{12} \\ s_{23} \end{pmatrix} = \begin{pmatrix} r_1 - r_2 & x_1 - x_2 & \theta_1 - \theta_2 \\ r_2 - r_3 & x_2 - x_3 & \theta_2 - \theta_3 \end{pmatrix} \begin{pmatrix} 1 & 0 \\ 0 & -\sin p \\ 0 & \cos p \end{pmatrix} \begin{pmatrix} k_r \\ k_\perp \end{pmatrix} \,, \tag{4.3.4}$$

where p is the pitch angle of the magnetic field in $x - \theta$ plane in Fig. 4.3.2.

The wavenumbers $k_r, k_\perp$ can be calculated by applying inverse matrix of the right hand side of the equation. The magnetic field pitch angle is $p \sim 20°$ around the LCFS at $R \sim 590$ mm. Figure 4.3.3 shows the wavenumber spectra of radial wavenumber k_r and poloidal wavenumber k_θ derived from the cross phase of V_fs. Here 200 ensembles are averaged. The dispersion relation clearly changes at 20 kHz. Phase velocity of k_θ is ~ 1000 m/s at the frequency less than 20 kHz, and ~ 4000 m/s at the frequencies higher than 20 kHz and both directions are in the electron diamagnetic direction. Blue lines are drawn to pass the phase velocity of $\omega/\bar{k}$ at 100 kHz, and red lines at 20 kHz, where $\bar{k}$ is the mean wavenumber. The linear dispersion relation is obscured at the frequencies higher than 150 kHz. The correlation length deduced from the broadening of k_θ spectrum at 100 kHz is $l_{cor} \sim 1/\sigma_k \sim 5$ cm. Figure 4.3.3 (a) and (c) show the radial wavenumber k_r spectrum. The average k_r polarity (i.e., direction) at $R = 560$ mm is the opposite of that at $R = 600$ mm at the frequencies higher than 20 kHz, while the change is not so clear at the frequencies less than 20 kHz. We define the MHD fluctuations as the fluctuations with frequencies less than 20 kHz, since the dispersion relation is clearly changed at 20 kHz as shown in Fig. 4.3.3.

Figure 4.3.4 shows the reconstructed wavenumber profile of the floating potential at 20 kHz and 100 kHz. The contour map is poloidally symmetric. This means that $\bar{k}_\theta$ is constant along the flux surface. Figure 4.3.5 shows the radial profiles of $\bar{k}_\perp$, $\bar{k}_\parallel$ and $\bar{k}_r$ at 10 kHz and 100 kHz. Here, $\bar{k}_\parallel$ is derived using signals of I_{is}, assuming structure of k is similar to those of V_f. $\bar{k}_\perp = -0.004 \pm 0.004$ mm^{-1}, $\bar{k}_\parallel = 0 \pm 0.04$ mm^{-1} and $\bar{k}_r = 0.005 \pm 0.005$ mm^{-1} at 10 kHz regardless of R. On the other hand, at 100 kHz, $\bar{k}_\perp = -0.04 \pm 0.01$ mm^{-1} at

$R < 620$ mm, while $\bar{k}_\perp = 0.03 \pm 0.01$ mm^{-1} at $R > 620$ mm. $\bar{k}_\parallel$ is much smaller than $\bar{k}_\perp$, $\bar{k}_\parallel = 0.01 \pm 0.01$ mm^{-1}. $\bar{k}_r$ varies continuously with R, decreasing from $\bar{k}_r = 0.01 \pm 0.01$ mm^{-1} at $R = 580$ mm to $\bar{k}_r = -0.02 \pm 0.01$ at $R = 620$ mm. These wavenumbers are calculated from the data V_f measured by the composite probe system. The $\pm$ ranges represent the widths of the wavenumber spectrum, which are derived from the coherence of each signal using the relation $\sigma(\omega) = \left\langle (\bar{k} - k)^2 s(k, \omega) \right\rangle^{1/2} = \left\{ 2(1 - C_{xy}(\omega)) \right\}^{1/2} / \Delta x$ in Eq. (2.2.13).
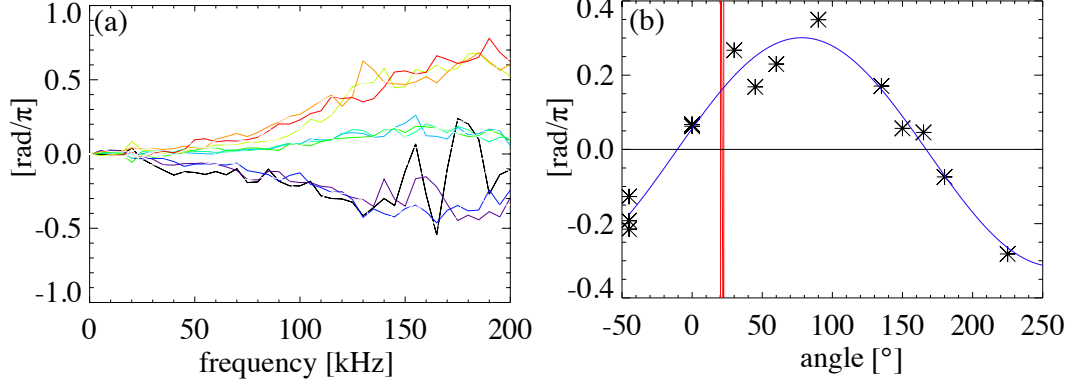
Figure 4.3.1: Cross phase between V_{f2} and V_{f3}. Different color curves in (a) represent the phases with different rotation angle of the composite probe. (b) shows the cross phase at 100 kHz as a function of the rotation angle. The red line shows the pitch angle of the magnetic field line.
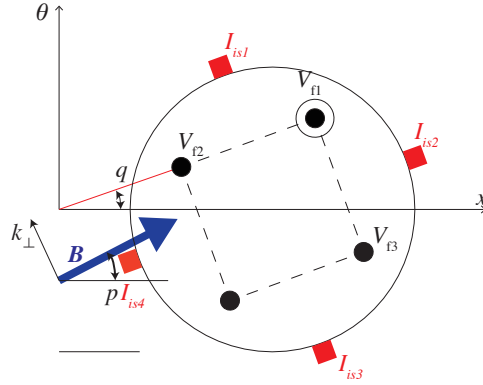
Figure 4.3.2: Schematic view of the coordinate and the locations of each electrode.
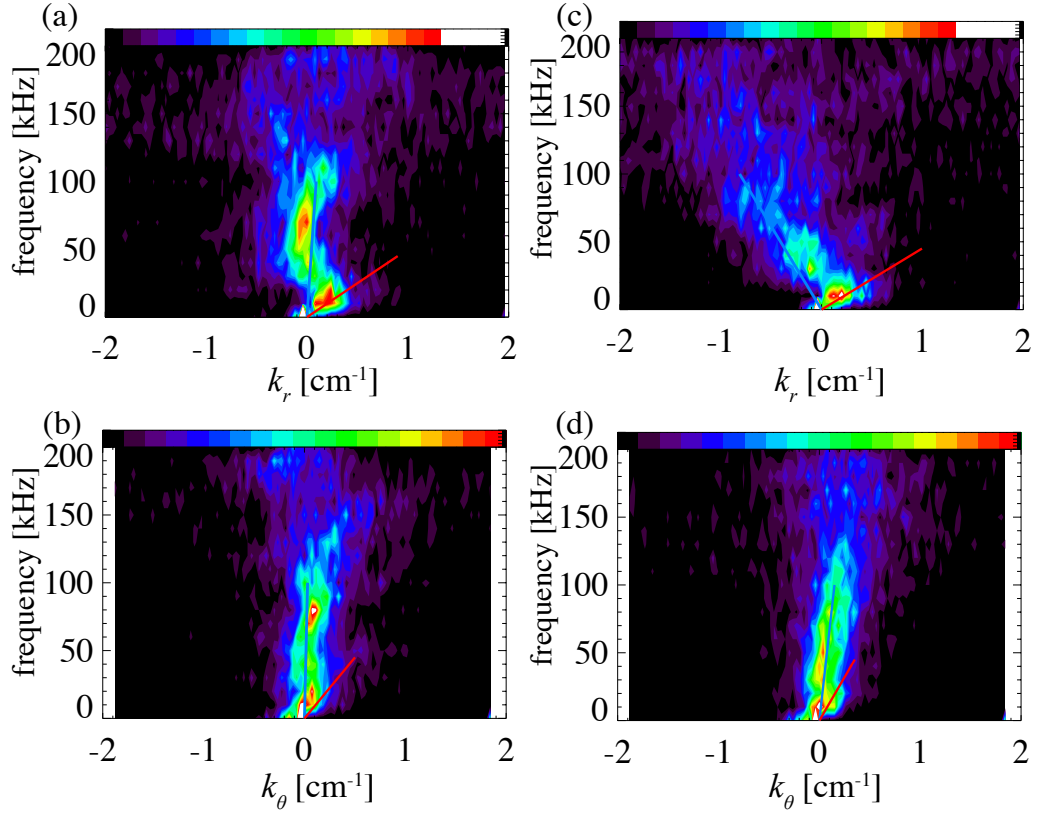
Figure 4.3.3: Wavenumber spectrum of k_r (a) and k_θ (b) at $R = 560$ mm and k_r (c) and k_θ (d) at $R = 600$ mm. These are derived from V_fs of the composite probe system. A clear difference between the dispersion relations up to 20 kHz and that above 20 kHz can be seen. Blue lines show the average phase velocity at 100 kHz and red lines show that at 20 kHz.
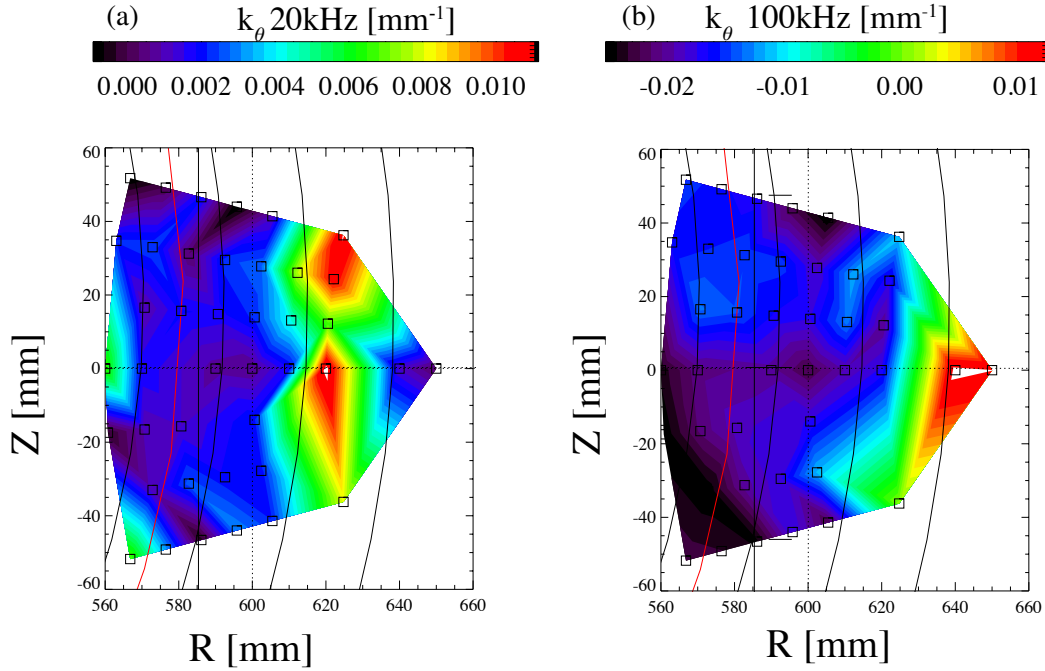
Figure 4.3.4: Ensemble averaged wavenumber $\bar{k}_\theta$ of plasma potential at 20 kHz (a) and 100 kHz (b) reconstructed from V_f fluctuation. The magnetic flux surfaces are shown in black curves and the LCFS is shown in red.
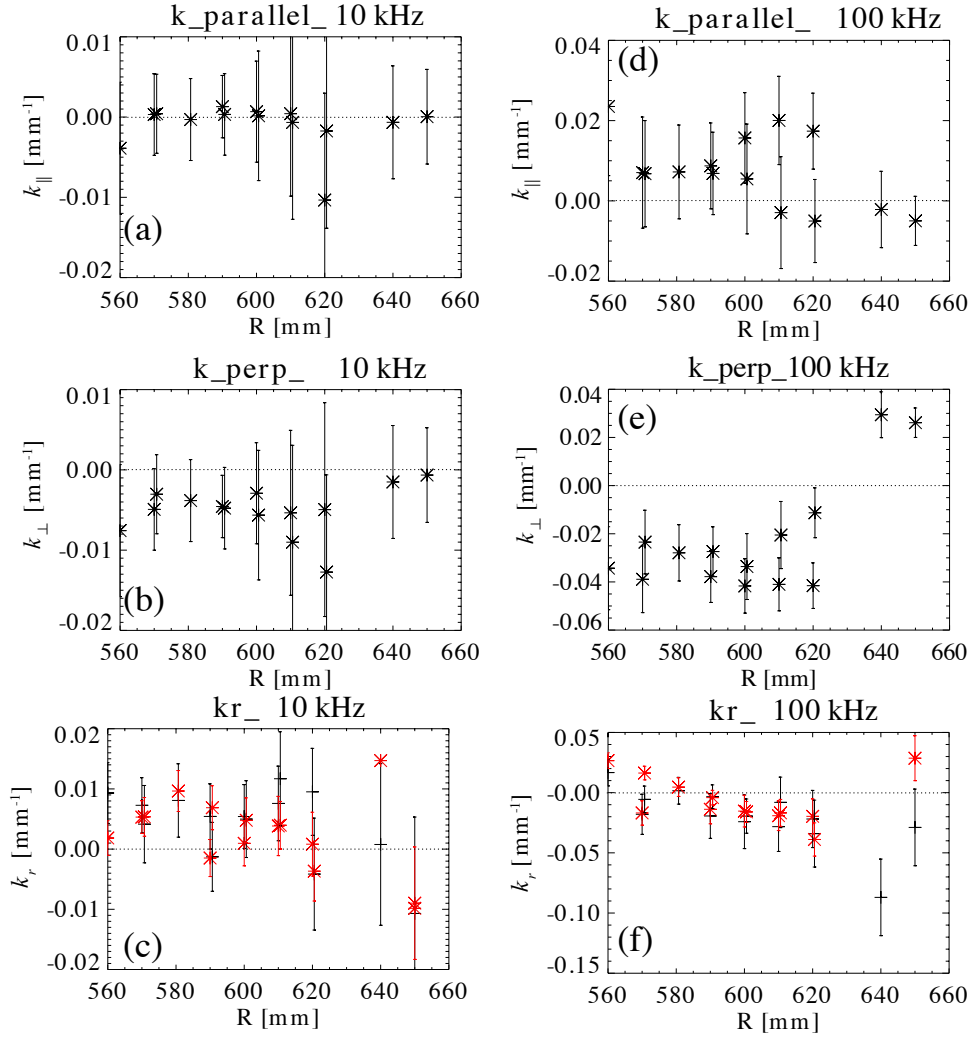
Figure 4.3.5: Radial profiles of wavenumber $\bar{k}_{\parallel}$ (a), $\bar{k}_{\perp}$ (b) and $\bar{k}_r$ (c) at 10 kHz calculated by the two point correlation, and $\bar{k}_{\parallel}$ (d), $\bar{k}_{\perp}$ (e) and $\bar{k}_r$ (f) at 100 kHz. In (c) and (f), the black symbols represent $\bar{k}_r$ derived from V_{f1} and V_{f2} and the red symbols represent those derived from V_{f1} and V_{f3}. The error bars represent shot by shot scatter of $\bar{k}$.

4.4 Turbulent transport

In this section, we calculate the radial electrostatic particle flux, which is believed to be the dominant particle transport route in conventional tokamaks. In evaluating the radial electrostatic particle transport due to edge turbulence, we need to estimate the local radial velocity given by $v_r = E_\theta/B$, where E_θ is given by the gradient of the static potential. In such a situation, the electrostatic particle flux is written as

$$\Gamma_r = \langle \tilde{n} \tilde{v}_r \rangle = \langle \tilde{n} \tilde{E}_\theta \rangle / B. \tag{4.4.1}$$

Thus, in order to evaluate the flux, the coherence and phase angle between the measured $\tilde{n}$ and $\tilde{E}_\theta$ must be accurate, in addition to the amplitudes $|\tilde{n}|$, $|\tilde{E}_\theta|$. Generally, these quantities are calculated from the data measured by three nearby electrodes, but the phase calculated from nearby electrodes are affected by the wavenumber structure. Thus, we need to compensate this effect.

Signals of I_{is} are used to evaluate $\tilde{n}$, $\tilde{n} = (\tilde{I}_{is1} + \tilde{I}_{is2} + \tilde{I}_{is3} + \tilde{I}_{is4})/2eA \times (\frac{k_B T_e}{m_i})^{-1/2}$ using Eq. (2.1.3). Since the locations of I_{is} measurements are radially different from E_θ measurements, the phase difference of $k_r \Delta_r$ is compensated, where Δ_r is the radial distance between the measurement points for I_{is}s and those for V_fs.

The Fourier transformed flux can be computed from the cross power between the density and electric fluctuations, using

$$\left\langle \tilde{n} \tilde{E}_\theta \right\rangle = \left\langle \tilde{n} i k_\theta \tilde{V}_f^* \right\rangle \delta\omega = \langle \tilde{n} \rangle \left\langle \tilde{V}_f \right\rangle \bar{k}_\theta \sin \theta_{\tilde{n}\tilde{V}_f} C_{\tilde{n}\tilde{V}_f} \delta\omega, \tag{4.4.2}$$

where $\theta_{\tilde{n}\tilde{V}_f}$ is the phase difference between $\tilde{n}$ and $\tilde{V}_f$, $C_{\tilde{n}\tilde{V}_f}$ is the cross coherence, $\delta\omega$ is the resolution of the frequency in Fourier transform. Figure 4.4.1 shows the profile of the particle flux Γ_r and each parameter in the equation. Error bars are derived from the shot by shot scatter of $\bar{k}_\theta$. The particle flux is outward over the entire frequency range, and dominated by the low frequency components less than 20 kHz due to the larger fluctuation amplitudes. The large cross phase between $\tilde{n}$ and $\tilde{V}_f$ also contributes to the large outward flux at the low frequencies, as shown in $\sin \theta_{\tilde{n}\tilde{V}_f}$ in Figs. 4.4.1 (a), (b) and (c). However, around $R = 580$ mm, transport at ~ 80 kHz increases. This corresponds to the power spectrum peak at 80 kHz around $R = 580$ mm, observed in Fig. 4.2.6. The total particle flux shows a decreasing trend with radius, as shown in Fig. 4.4.2. This is because the $\tilde{n}$ and $\tilde{V}_f$ fluctuation amplitudes also decrease with increasing radius.

We can estimate the radial diffusion coefficient from the particle flux and the density profile. The diffusion coefficient is defined as

$$D_r = -\Gamma_r \frac{1}{dn/dx}. \tag{4.4.3}$$

Using the obtained values, the coefficient is $D_r = 5 \times 10^{20}/(10^{18}/(2 \times 10^{-2})) = 10 \, \mathrm{m^2 s^{-1}}$ at $R = 560$ mm. On the other hand, $D_{Bohm} = kT_e/16\,eB = 10 \, \mathrm{m^2\,s^{-1}}$, where $T_e = 20$ eV and $B = 0.12$ T, and $D_{cl} = \frac{m_e kT_e}{e^2 B^2} \nu_{ei} = 3.7 \times 10^{-3} \, \mathrm{m^2\,s^{-1}}$. Since T_e is roughly constant in the region $560 \, \mathrm{mm} < R < 620 \, \mathrm{mm}$, D_{Bohm} should be proportional to R, while experimental D_r (Eq. (4.4.3)) is decreasing monotonically against R, unlike D_{Bohm}.
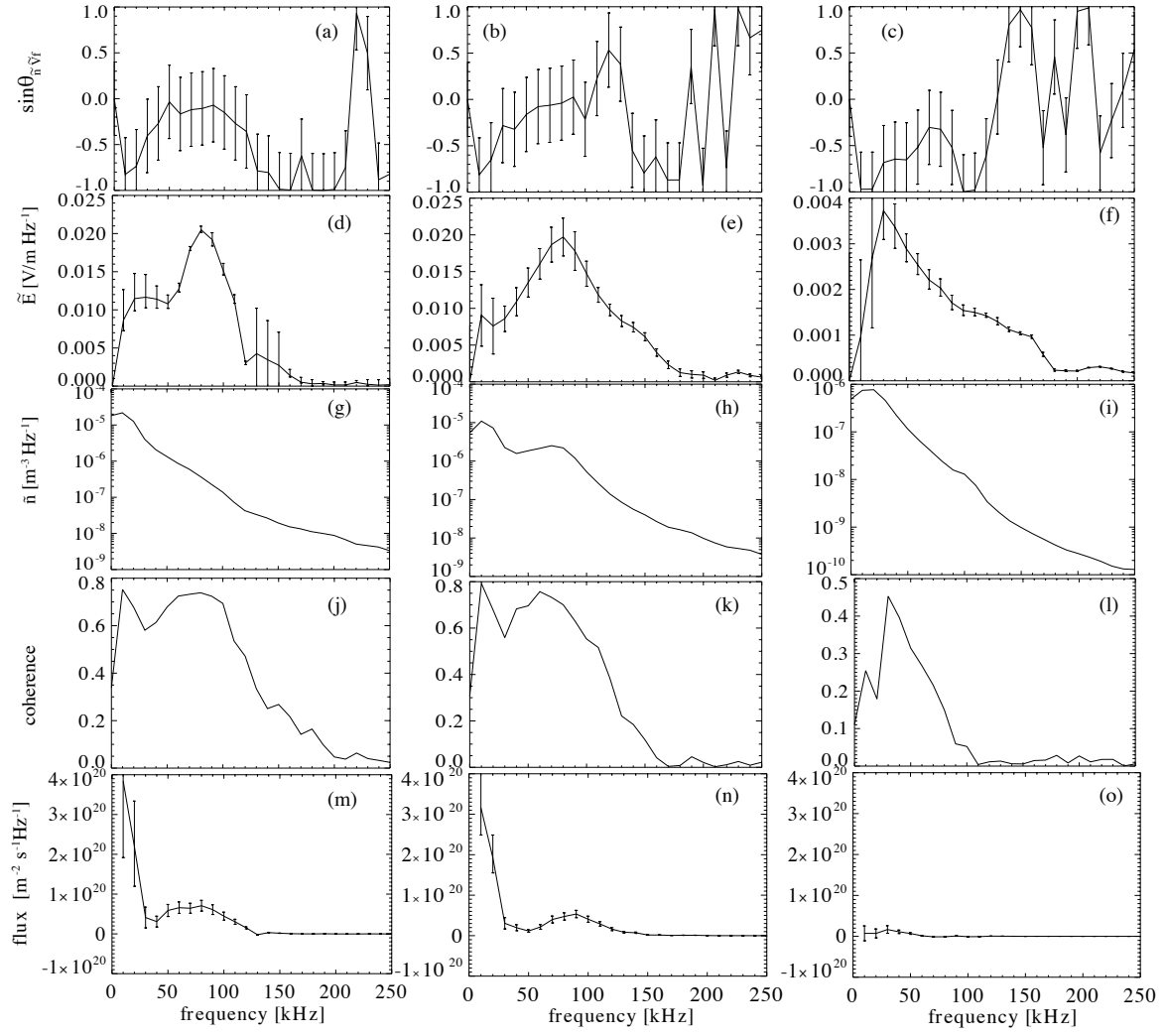
Figure 4.4.1: Frequency dependence of $\sin(\theta_{\tilde{n}\tilde{V}_{\mathrm{f}}})$ (a), (b), (c), $|\tilde{E}|$ (d), (e), (f), $|\tilde{n}|$ (g), (h), (i), coherence between $\tilde{E}$ and $\tilde{n}$ (j), (k), (l) and particle flux (m), (n), (o) at $R = 560$ mm (left), $R=580$ mm (middle) and $R=650$ mm (right). Error bars are derived from standard deviations of each value in multiple shots.

46
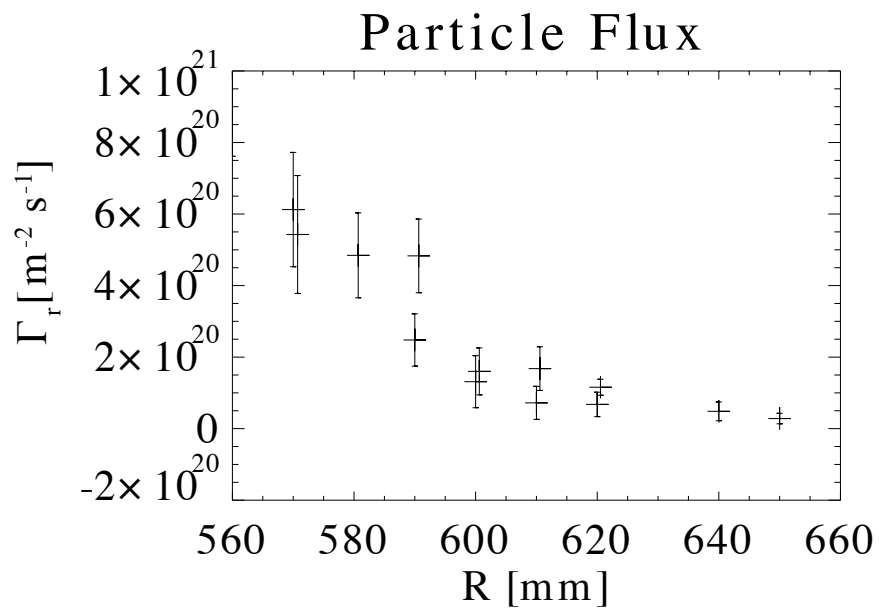
Figure 4.4.2: Electrostatic particle flux Γ_r as a function of radius.

4.5 Measurement of plasma flow

As mentioned in Sec. 3.3.1, we can measure the flow of plasma by using the signals of ion saturation current I_{is} measured by the electrodes located at the side of the composite probe. When the plasma flow is divided by material into the upstream and downstream regions, the upstream I_{is} becomes greater than that in the downstream side. The following shows the relationship between the ion saturation current and the plasma flow velocity [73].

$$M_i = \frac{u_d}{C_s} = \frac{u_d}{\sqrt{k_B(Z_i T_e / m_i)}}, \quad \frac{j_{up}}{j_{down}} = \exp(M_i / M_c), \tag{4.5.1}$$

where M_i is ion mach number, the ratio between plasma flow velocity u_d and ion sound speed C_s. j_{up} and j_{down} represent the ion saturation currents measured by the electrodes at the upstream and downstream sides of the plasma flow. Figure 4.5.1 shows the time averaged profile of the poloidal flow and the toroidal flow.

Because the electrodes of the mach probe are separated by 20 mm, each electrode measures slightly different location from the center of the probe head. When the radial gradient of the density at the plasma edge is large, this difference cannot be ignored. We corrected this effect by interpolating the density at the location of the center of the front surface of the composite probe system.
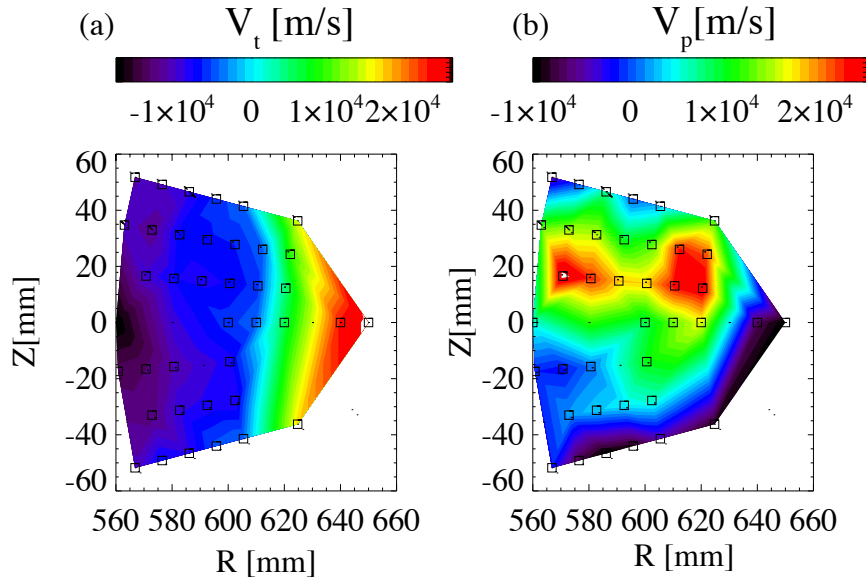
Figure 4.5.1: 2D profile of the toroidal flow (a) and the poloidal flow (b) measured by the mach probes of the composite probe.

4.6 Results from the high field side probe

As we mentioned in Sec.3.3.5, we installed a Langmuir probe at the high field side wall, as shown in Fig. 3.3.10. Figure 4.6.1 shows V_f of the composite probe system (located at the low field side) and that of the high field side (HFS) probe. At ~ 30 ms, we moved the plasma inward so that the electrode of HFS probe becomes located on the same flux surface as the electrodes of the composite probe system. The power spectrum of the data obtained by the HFS is about one order of magnitude smaller than that obtained by the composite probe located at the low field side (LFS) (Fig. 4.6.1 (b)). The cross coherence is less than 0.2 (Fig. 4.6.1 (c)). The smaller HFS amplitude seems to be consistent with the nature of HFS good curvature region, where instabilities tend to be suppressed [74]. Since the magnetic field line connection length between the HFS and the LFS regions is very long, the poor coherence is reasonable. The finite phase difference between the HFS and the LFS indicates the time delay due to the propagation of the fluctuation (FIg. 4.6.1 (d)). This also supports the assumption that the magnetic field line connecting the HFS and the LFS is very long.
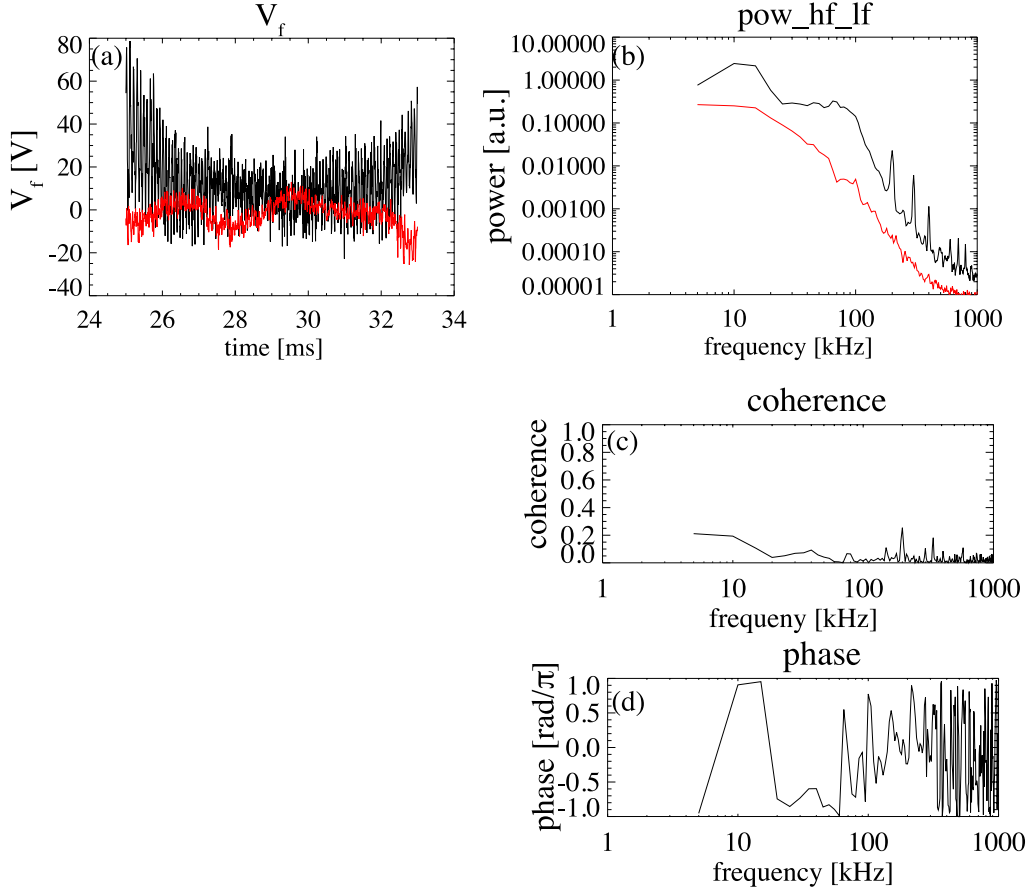
Figure 4.6.1: Time evolutions of V_fs of the composite probe system (black) and the high field side probe (red) (a), power spectra of each signal (b), coherence (c) and cross phase (d) of the two signals.

4.7 Magnetic field fluctuation

Plasmas in the Ohmic discharges show coherent oscillation at 10 kHz in spatially wide region. Magnetic pickup coils at the wall (Fig. 4.2.5) show coherent structure at the low field side, and the poloidal mode number is approximately 2. The magnetic fluctuations have a long correlation length along the field line.

Figure 4.7.1 shows the correlation between the signals of the poloidal pickup coil array and the center pickup coil of the array. We calculated the poloidal correlation lengths by fitting a correlation profile with exponential dependences and gaussian dependences (Fig. 4.7.1 and Figs. 4.7.2 (b), (c)). The poloidal and toroidal correlation lengths l_{pol} l_t are defined by fitting the following functions

$$
\begin{cases}
\exp\left(-\dfrac{\sqrt{(r-r_0)^2+(z-z_0)^2}}{l_{pol}}\right) & \text{(exponential fitting)} \\[2ex]
\exp\left(-\dfrac{(r-r_0)^2+(z-z_0)^2}{l_{pol}^2}\right) & \text{(gaussian fitting)},
\end{cases}
\tag{4.7.1}
$$

$$
\begin{cases}
\exp\left(-\dfrac{\delta l_t}{l_t}\right) & \text{(exponential fitting)} \\[2ex]
\exp\left(-\dfrac{\delta l_t}{l_t}\right)^2 & \text{(gaussian fitting)},
\end{cases}
\tag{4.7.2}
$$

where r_0, z_0 represent the location of the reference pick up coil and δl_t is the toroidal distance between the central pickup coil and each pickup coil. At 10 kHz, the toroidal correlation length l_t has the maximum of about 5 m, which is about 20 times longer than that at 100 kHz. Poloidal correlation length l_{pol} is 3.5 m at 10 kHz, and less than 0.05 m at 100 kHz (Fig. 4.7.3). RR diffusion coefficient D_{st} can be estimated by using the correlation length and $\tilde{B}_r/B_t$ shown in Fig. 4.2.8. The step size is $\Delta r = \tilde{B}_r/B_T \times l_\parallel = 6 \times 10^{-2}$ m, and the time interval is $\tau \sim 10^{-4}$ sec (Eq.(1.8.15)). Here, τ is taken as $\tau = l_\parallel/v_{T_i}$, considering particle flux is

determined by movements of ion. The calculated diffusion coefficient is $D_{st} = 10\,\mathrm{m^2 s^{-1}}$. This is comparable to the electrostatic diffusion coefficient D_r and D_{Bohm} evaluated in Sec. 4.4. It should be noted that D_{st} is estimated on the assumption that magnetic fluctuations are fully stochastic, thus the actual value can be smaller.
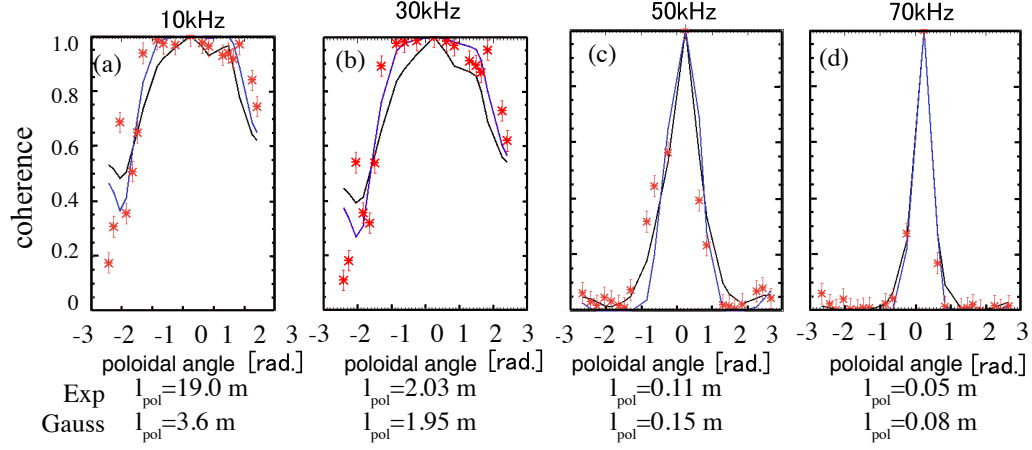
Figure 4.7.1: Coherence of poloidal pickup coil array signals as a function of poloidal angle distance. Coherences at 10 - 70 kHz are shown. Black and blue curves represent fittings to exponential and gaussian functions, respectively.
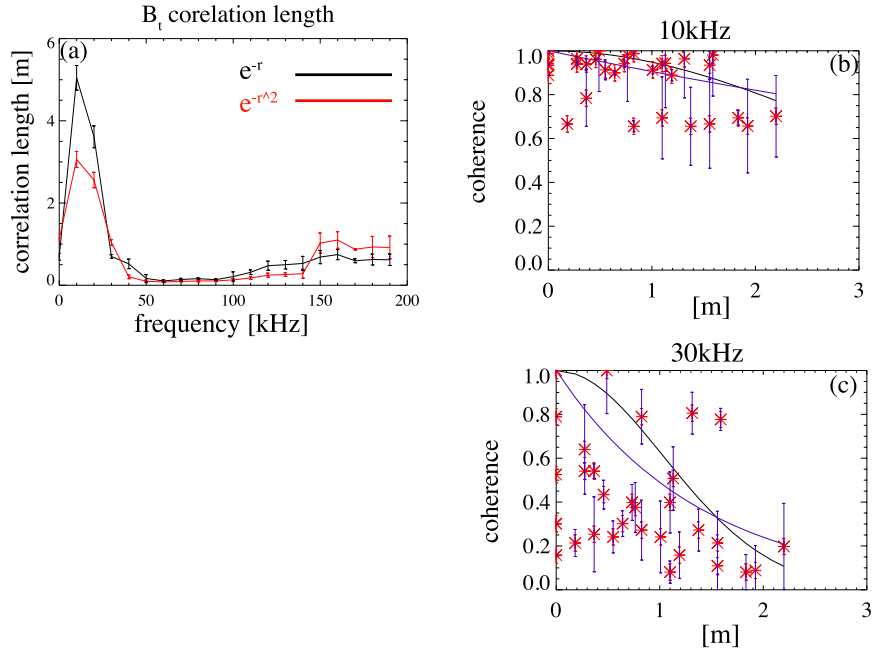
Figure 4.7.2: Toroidal correlation length of magnetic fluctuation signals vs frequency derived from the toroidal magnetic pickup array (a), and the correlation profile at 10 kHz (b) and 30 kHz (c). Black and red curves in (a) represent the results obtained by fitting to exponential and gaussian dependences, respectively. Black and purple curves in (b) and (c) represent the results obtained by fitting to exponential and gaussian dependences, respectively.
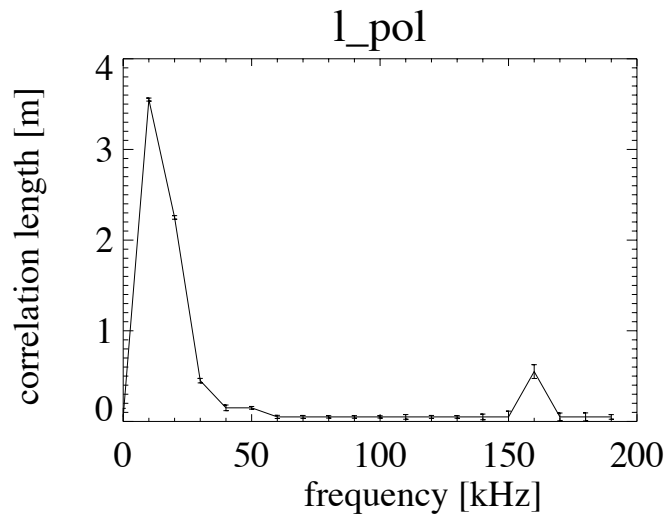
Figure 4.7.3: Poloidal correlation length of magnetic fluctuation signals vs frequency derived from the poloidal magnetic pickup coil array by using gaussian fitting.

51

4.8 Parallel correlation length

Since particles move freely and quickly along a magnetic field line, fluctuations along a field line tend to have a long correlation length and a long wavelength. Therefore, it is useful to take coordinates with respect to the local magnetic field direction. Furthermore, it is expected that the parallel correlation length is much longer than the perpendicular ones and parallel wavenumber is much smaller than the perpendicular ones. Figure 4.8.1 shows a camera image of the plasma when the composite probe system (probe 2) and probe 3 lie on the same magnetic field line. The bright spots near the center and the bottom represent the emissions from the composite probe system and probe 3. The bright curve passing the two spots represents the magnetic field line. When the bright curve is connecting the two probes, the correlation between the two probes becomes high. Figure 4.8.2 shows that V_fs are strongly correlated when the two probes are on the same magnetic field line. The cross spectrum of $\tilde{V}_f$s of the toroidally and poloidally separated two probes (probe 2 and probe 3) were calculated. In this experiment, the location of probe 2 was fixed at R=550 mm and Z=0 mm, and the location of probe 3 is scanned to find the location of maximum correlation. Figures 4.8.3 (a), (b) show the squared cross-coherence and cross-phase between the floating potential fluctuations. At other various locations of probe 3, the coherence is high (~ 0.7) at 10 kHz, but less than 0.2 in other frequencies. Figure 4.8.3 (c) shows the poloidal profile of squared cross-coherence of $\tilde{V}_f$s at 60 kHz measured with probe 2 and probe 3. The peaked profile of the squared cross-coherence suggests that these two probes are connected by the same magnetic field line when the coherence shows a maximum.
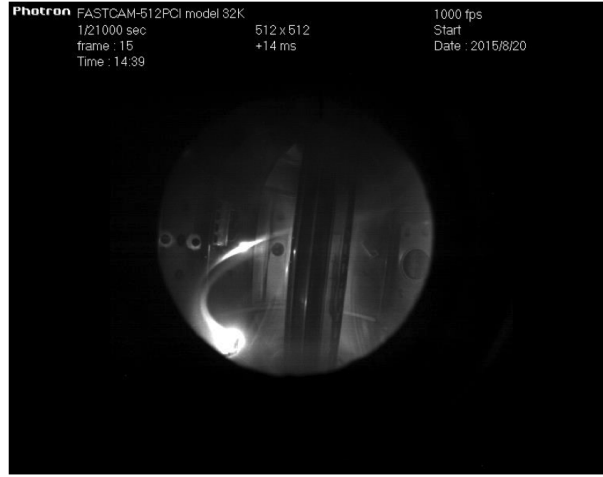
Figure 4.8.1: Visible CCD camera image of the plasma. The bright spots near the center and the bottom represent the emissions from the composite probe system and the probe 3. The bright curve passing the two spots represents the magnetic field line.

4.8.1 Reconstruction of the spatial structure of parallel correlation

Figure 4.8.4 (a) shows the magnetic field line in $R - Z$ plane reconstructed from the signals measured by the 3 axis magnetic pickup coil. Equations

$$\mathrm{d}R = \mathrm{d}B_r/B_\phi \times \mathrm{d}\phi, \ \mathrm{d}Z = \mathrm{d}B_z/B_\phi \times \mathrm{d}\phi, \tag{4.8.1}$$

are solved for the reconstruction. Figure 4.8.4 (b) shows the trace (Poincare plot) of the line starting from probe 2 during the time period of 28 - 28.1 ms. As shown in Fig. 4.8.4 (b), the trajectory of the field line makes a circular motion with a diameter of ~ 3 cm in the plane (i.e., poloidal cross section). This motion would induce the same motion of the spatial structure of the turbulence which is elongated along the magnetic field line.

Here, we formulate the trajectory of the field line and prove that the linear relationship $\mathrm{d}R = \mathrm{d}B_r/B_\phi \times \mathrm{d}\phi, \ \mathrm{d}Z = \mathrm{d}B_z/B_\phi \times \mathrm{d}\phi$ are satisfied under a certain condition. In the following we adopt coordinates perpendicular (denoted by subscript $\perp$) and radial (denoted by subscript r) instead of Z and R. The perpendicular and
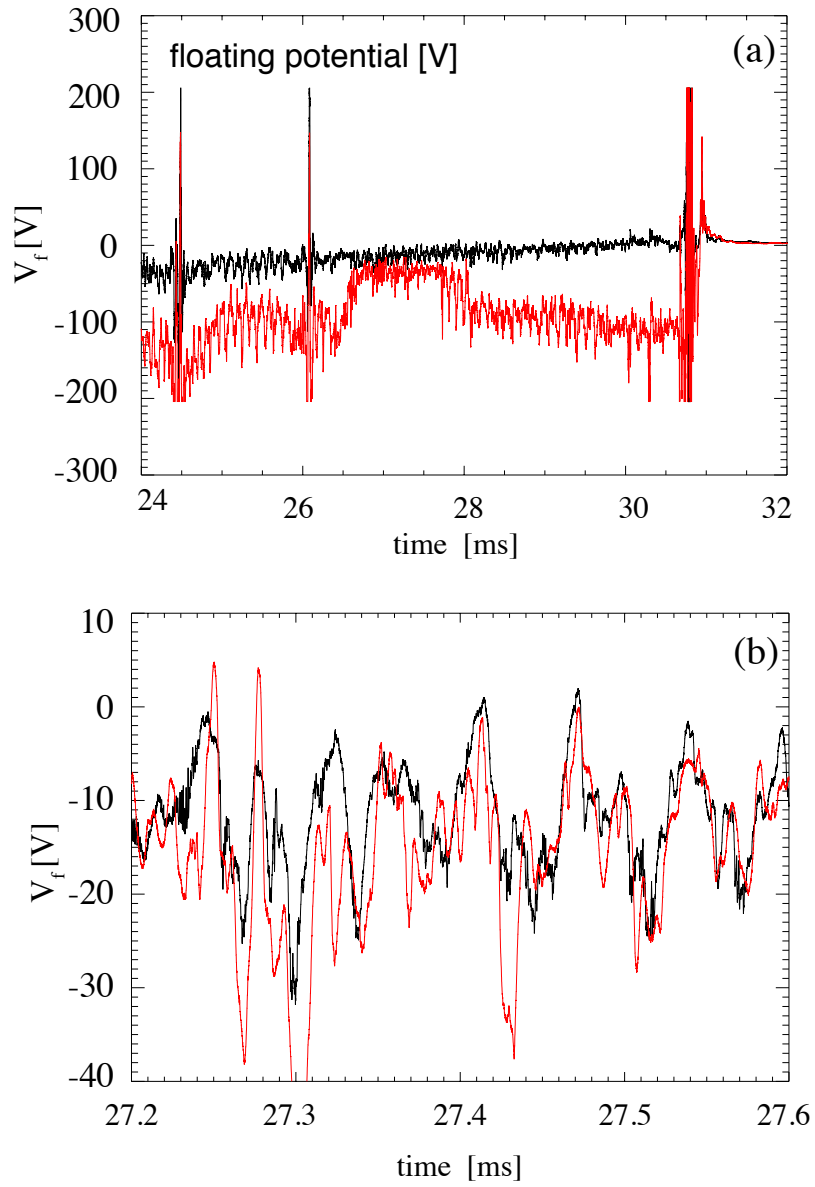
Figure 4.8.2: Time evolutions of V_fs measured by probe 2 (black) and probe 3 (red) (a). Expanded view (27.2 - 27.6 ms) of (a) is shown in (b).
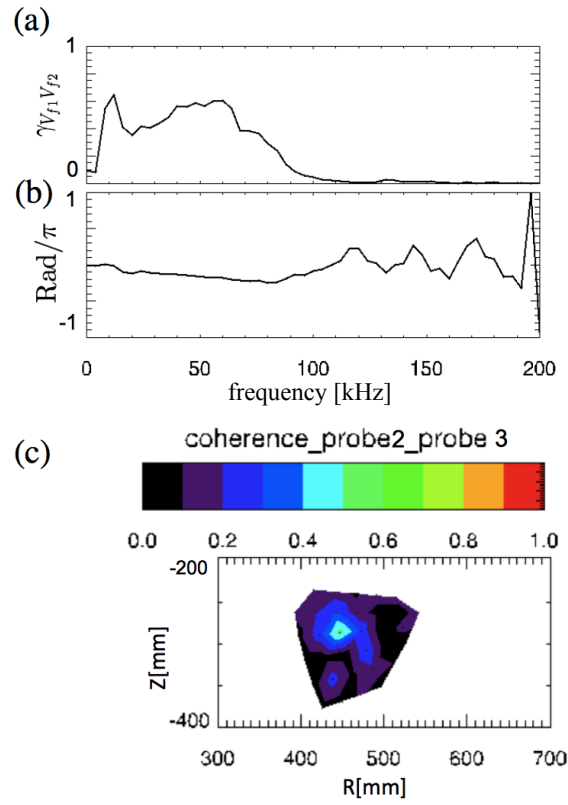
Figure 4.8.3: Squared coherence (a) and phase (b) of $\tilde{V}_f$s measured with probe2 and probe3, and 2-D profile of the squared cross-coherence in $R - Z$ plane at 60 kHz (c). The profile was obtained by scanning the locations of probe 3 under the condition that the location of probe 2 is fixed at $R = 550$ mm.

the radial displacements of the field line trajectory are expressed by

$$\begin{pmatrix} \delta l_\perp \\ \delta l_r \end{pmatrix} = \begin{pmatrix} \int_0^{l_\parallel} \frac{\delta B_\perp}{B_0} dl_\parallel \\ \int_0^{l_\parallel} \frac{\delta B_r}{B_0} dl_\parallel \end{pmatrix}. \tag{4.8.2}$$

Assuming that the magnetic fluctuations are represented by a single mode with a poloidal and a toroidal mode numbers m and n, magnetic fluctuations (i.e., $\delta B_\perp$ δB_r) are proportional to $e^{i(m\theta-n\phi)}$. Then Eq. (4.8.2) is rewritten as

$$\begin{pmatrix} \delta l_\perp \\ \delta l_r \end{pmatrix} = \begin{pmatrix} \int_0^{l_\parallel} \frac{\tilde{B}_\perp}{B_0} e^{i(m\theta-n\phi)} dl_\parallel \\ \int_0^{l_\parallel} \frac{\tilde{B}_r}{B_0} e^{i(m\theta-n\phi)} dl_\parallel \end{pmatrix}, \tag{4.8.3}$$

where $\delta B_\perp$, δB_r are $\tilde{B}_\perp e^{i(m\theta-n\phi)}$ and $\tilde{B}_r e^{i(m\theta-n\phi)}$. The integral part of the equation becomes

$$\int_0^{l_\parallel} e^{i(m\theta-n\phi)} dl_\parallel = \int_0^{l_\parallel} e^{i\vec{k}\cdot\vec{l}} dl = \int_0^{l_\parallel} e^{ik_\parallel l_\parallel} dl_\parallel = e^{i(m\theta_0-n\phi_0)} \frac{e^{ik_\parallel l_\parallel}-1}{k_\parallel}. \tag{4.8.4}$$

Here we assume that $\delta B \ll B_0$ and the integral path is taken along the non-perturbed path. When $k_\parallel l_\parallel \ll 1$,

$$\begin{pmatrix} \delta l_\perp \\ \delta l_r \end{pmatrix} \approx \begin{pmatrix} \frac{B_\perp}{B_0} l_\parallel \\ \frac{B_r}{B_0} l_\parallel \end{pmatrix}. \tag{4.8.5}$$

Thus, the condition $k_\parallel l_\parallel \ll 1$ must be satisfied to use the linear relationship.

Before analyzing the data of probe 2 and 3, here, we derive $k_\parallel$ using only the signals of probe 2 to show that the above condition is well satisfied. In order to derive $k_\parallel$ more accurately than using a single shot with fixed electrodes, we used the data with multiple shots with different angles of the electrodes against the magnetic field line. Figure 4.8.5 shows the phase difference between the two electrodes at the MHD frequency of 10 kHz as a function of the rotation angle of the composite probe system. This figure shows that the phase difference between the two electrodes is almost 0 at 10 kHz, when the electrodes are aligned along the field line. This indicates $\bar{k}$ of MHD fluctuation is almost perpendicular to the magnetic field at $\sim$ 10 kHz, and these data imply $\bar{k}_\parallel = 0.2 \pm 0.6$ m^{-1} at $R = 580$ mm, and $k_\parallel = 0.1 \pm 0.1$ m^{-1} at $R = 570$ mm. This satisfies the condition of $k_\parallel l_\parallel \ll 1$ for the present combination (probe 2 and probe 3 with $l_\parallel \sim 1$ m). Figure 4.8.6 shows the frequency dependences of $\bar{k}_\perp$ and $\bar{k}_\parallel$, which are obtained by the above mentioned method.

If the wave structure is completely frozen to the magnetic field line, it can be considered that the correlation distribution in $R-Z$ plane is oscillating with a magnetic field line. As shown in Fig. 4.8.7, this oscillation is observed as the oscillation of the phase and coherence. Figure 4.8.8 illustrates the situation, where the structure of the correlation $C(\omega, dR, dZ, l_\parallel)$ is oscillating along with the magnetic field line.

When the wavenumber spectrum of the turbulence $S(\omega, \mathbf{k})$ is independent in each direction of $\mathbf{k}$, it can be decomposed as

$$S(\mathbf{k}) = S_\omega(k_\parallel) \times S_\omega(k_\perp) \times S_\omega(k_r). \tag{4.8.6}$$

In addition, we assume that each component is expressed with a gaussian distribution,

$$S_\omega \propto \exp\left(-\frac{(k-\bar{k})^2}{\Delta k^2}\right). \tag{4.8.7}$$

Then cross spectrum can be expressed by the spectrum using Wiener-Khinchin theorem, and in the present case, it becomes

$$C_\omega(x) = \int_{-\infty}^{\infty} \exp\left(-\frac{(k-\bar{k})^2}{\Delta k^2}\right) e^{ikx} dk \propto \exp\left(-\frac{\Delta k^2 x^2}{4}\right) e^{i\bar{k}x}. \tag{4.8.8}$$

Thus, the two dimensional cross spectrum in $R-Z$ plane is

$$C_\omega(dR, dZ) \propto \exp\left(-\frac{\Delta k_r^2 dR^2}{4}\right) \times \exp\left(-\frac{\Delta k_\perp^2 dZ^2}{4}\right). \tag{4.8.9}$$
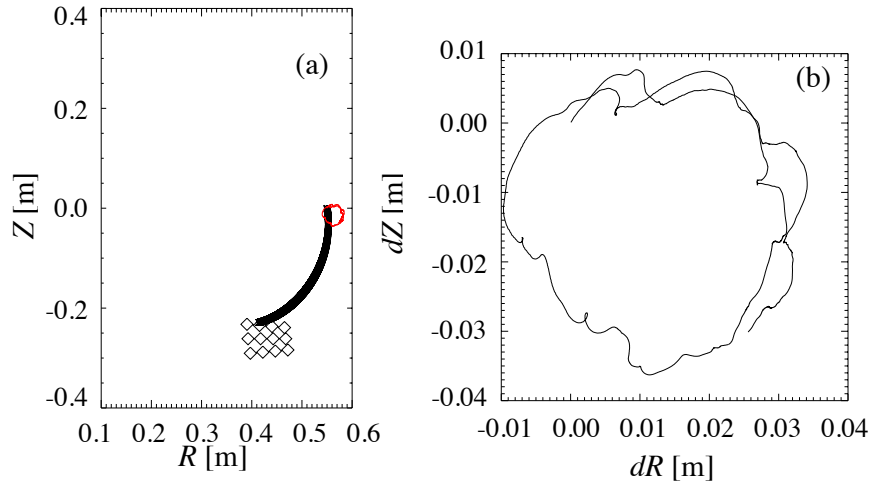
Figure 4.8.4: Magnetic field line reconstructed from $dR = dB_r/B_\phi \times d\phi, dZ = dB_z/B_\phi \times d\phi$. (a) shows the field line projected on $R-Z$ plane, and (b) shows the trace (Poincare plot) of the line on the plane of probe 3 starting from probe 2 during the time period of 28 - 28.1 ms.

Thus, the correlation length in $R-Z$ plane becomes $l_r = \frac{2}{\Delta k_r}$, $l_\perp = \frac{2}{\Delta k_\perp}$. When the structure fluctuates along with the magnetic field line, this fluctuation can be detected as the fluctuation of coherence. When we take a sufficiently short time window and calculate the coherence, we will obtain a single point of Eq. 4.8.9 for the corresponding set of (dR, dZ). Thus, the 2D structure $C_\omega(dR, dZ)$ can be reconstructed by mapping the time evolution of coherence into corresponding magnetic field location in R-Z plane.

Figure 4.8.9 shows the time evolution of poloidal and radial magnetic fluctuations expressed by dR and dZ and the mapping to the R-Z plane. In the reconstruction, we divided the signals of V_fs into 0.02 ms time windows during 26 ms to 30 ms, and mapped the coherence into the reconstructed magnetic field location. Then the R-Z plane is gridded by 5 mm, and the signals (i.e., cross spectra) in the same gridded area are ensemble averaged. Figure 4.8.10 shows the schematic illustration of the coherence reconstruction procedures. Each circle in Fig. 4.8.10 (a) corresponds to each divided signal in Fig. 4.8.10 (b), and signals in the same grid are used for ensemble averaging to derive a cross spectrum in Eq. 2.2.3. Thus, the cross spectrum of each grid becomes

$$S_{ij}(\omega) = \frac{1}{N_{ij}} \sum_{\substack{x_i < x < x_{i+1} \\ y_j < y < y_{j+1}}} \tilde{V}_{f2,x,y}(\omega)\tilde{V}^*_{f3,x,y}(\omega), \tag{4.8.10}$$

where $\tilde{V}_{f,x,y}$ is the Fourier transformed floating potential when the reconstructed field line is located at x and y in the R-Z plane. N_{ij} is the number of the ensembles in each grid. N_{ij} can be different, so that the statistical errors can also be different, but depends on the grid. Note that the we adopt frequency domain-space domain expression with coordinates (ω, dR, dZ) instead of fully Fourier transformed coordinates. Therefore S in Eq. (4.8.10) is a complex number (i.e., cross spectrum) having amplitude (i.e., cross coherence) and phase (i.e., cross phase) information, which are shown in later.

The maps were made for five discharges, and the maps are merged so that the peaks of the maps have the same relative coordinate (i.e., $dR = 0$, $dZ = 0$) with respect to the field line. Figure 4.8.11 shows the number of ensembles for each location, and the errors get greater when the ensemble number is small. The grids with less than 10 ensembles are excluded as unreliable. Figure 4.8.12 shows the reconstructed map of cross coherence.

Assuming that the turbulence with the frequency above that of the MHD fluctuation is frozen to the magnetic field line, the reconstructed profile of coherence between probe 2 and probe 3 is fitted with a Gaussian function as shown in Fig. 4.8.13. Decay lengths at 50 kHz are $\delta R = 30$ mm and $\delta Z = 12$ mm. These lengths agree roughly with the correlation length derived from the dispersion relation of $1/\sigma_{k_\theta} \sim 50$ mm in Fig. 4.3.3. This supports the assumption that the turbulent structure is frozen on a magnetic field line, and the (parallel) axis of its spatial structure is tilted when the field line is tilted by the MHD fluctuation. At the peak, the coherence has the maximum of 0.7, and the phase difference is less than 0.1π rad up to 100 kHz.
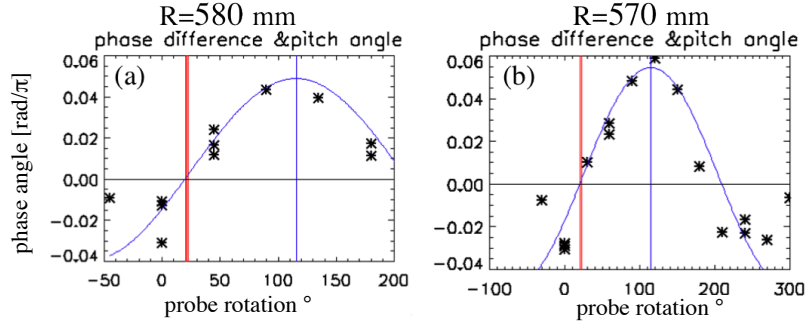
Figure 4.8.5: Phase differences between the two electrodes in the composite probe (probe 2) at the MHD frequency of 10 kHz (black asterisks) as a function of the angle between the field line and (the line passing through) the two electrodes at $R = 580$ mm (a), 570 mm (b). Fitted curves are shown in blue and the red vertical lines indicate the pitch angle, where the two electrodes are aligned along the field line.

Figure 4.8.14 shows the reconstructed maps of phase differences of V_fs between probe 2 and probe 3. From these measurements, we can estimate the parallel wavenumber $k_\parallel$ and correlation length $l_{cor\parallel}$ in addition to the two point correlation method used in Sec 4.3. The location of the maximum coherence is considered to be the closest location to the magnetic field line, because the location has the smallest phase difference as shown in Fig. 4.8.14. The phase difference $\Delta\theta_{peak} < 0.1\pi$ rad at 100 kHz corresponds to $|k_{\parallel 100}| < 10^{-4}$ mm^{-1} and parallel velocity $|v_\parallel| > 10^6$ m/s . Note that the Alfven speed is approximately $v_A \sim 10^8$ m/s, the electron thermal speed is $v_{th,e} \sim 2 \times 10^6$ m/s, and ion thermal speed is $v_{th,i} \sim 4 \times 10^4$ m/s. When $k_\parallel l_\parallel$ is negligible, the structure of the phase reflects $k_\perp$ (see Fig. 4.8.14). A velocity much slower than the Alfven velocity and much faster than the ion thermal velocity is consistent with the standard drift wave picture, where the electrostatic charge separation due to the different behaviors of electrons and ions is important. A velocity comparable to the electron thermal velocity is consistent with that the Maxwell's relation (i.e., strong in-phase correlation between density and potential fluctuations) is not satisfied. These comparisons imply that the observed parallel velocity $|v_\parallel| > 10^6$ m/s is consistent with the drift wave picture.

The correlation drop along the field line has the information on the parallel correlation length. At 50 kHz, correlation peak has 0.7 and drops below 0.1 at 200 kHz. At 50 kHz, $\sigma_k = \sqrt{\langle (k - \bar{k})^2 S(k,\omega) \rangle} = 0.9$ m^{-1} and the correlation length becomes1 $1/\sigma_k = 1.1$ m. Here, σ_k is derived from the the relation $\sigma(\omega) = \langle (\bar{k} - k)^2 s(k,\omega) \rangle^{1/2} = \{ 2(1 - C_{xy}(\omega)) \}^{1/2} /\Delta x$ (Eq. (2.2.13)).

Figure 4.8.15 (a) shows the enlarged view of the phase difference at 50 kHz shown in Fig. 4.8.14 (a). In Fig. 4.8.15 (b) we used this phase difference to calculate the wavenumbers $k_r \sim 0.01$ mm^{-1} and $k_\perp \sim -0.01$ mm^{-1}. Figures 4.8.15 (c) and (d) show k_r and $k_\perp$ spectra derived from V_fs in probe 2. The peak wavenumbers in Figs. 4.8.15 (c) and (d) are $k_r \sim 0.01$ mm^{-1}, $k_\perp \sim -0.01$ mm^{-1}, which agree with those shown in Fig. 4.8.15 (b). Figures 4.8.15 (c) and (d) show the widths $\sigma_{k_r} \sim \sigma_{k_\perp} \sim 0.05$ mm^{-1}. This leads to the correlation lengths of $1/\sigma_{k_r} = 1/\sigma_{k_\perp} = 20$ mm. These lengths roughly agree with the decay lengths shown in Fig. 4.8.13.
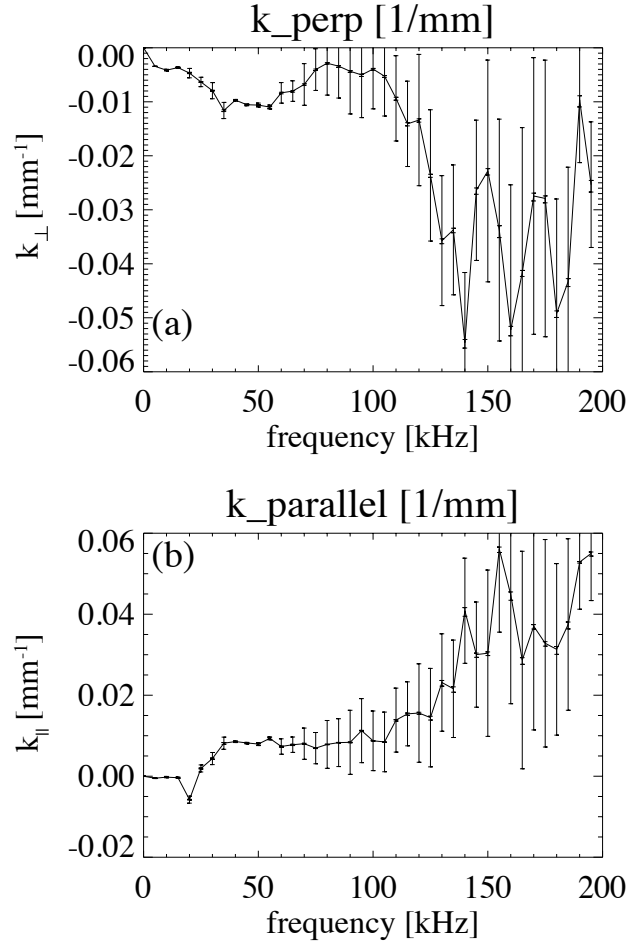
Figure 4.8.6: The frequency dependence of wavenumbers $k_\perp$ and $k_\parallel$ at $R = 570$ mm. Here wavenumbers are derived from the fitting curves in Fig. 4.8.5.
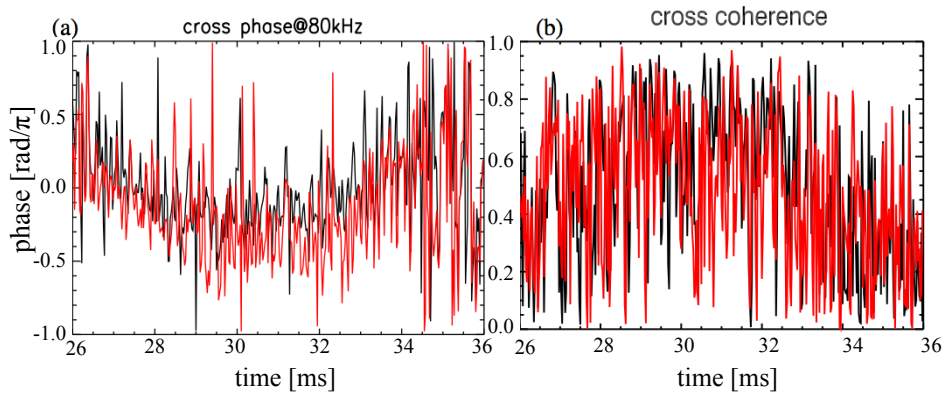
Figure 4.8.7: Time evolutions of cross-coherence (a) and cross-phase (b) of $\tilde{V}_f$s measured by probe 2 and probe 3 at 80 kHz. Black curves show the case when an electrode in probe 2 and probe 3 is analyzed and the red curves show the case when another electrode, which is poloidally 5 mm apart from the first electrode in probe 2, is analyzed.
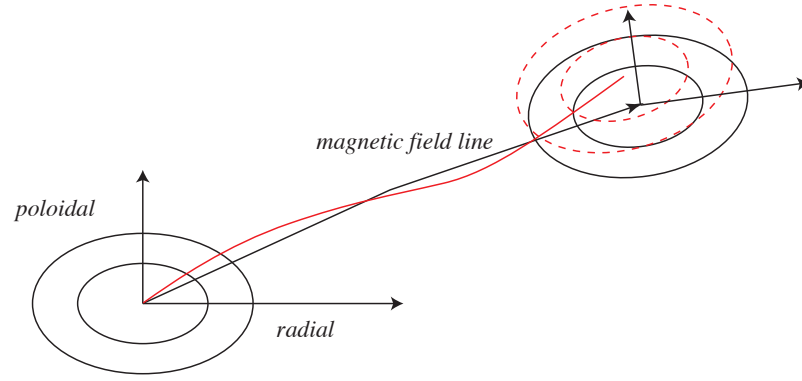
Figure 4.8.8: Schematic view of the contours of correlation $C(dR, dZ)$ at two poloidal cross sections.
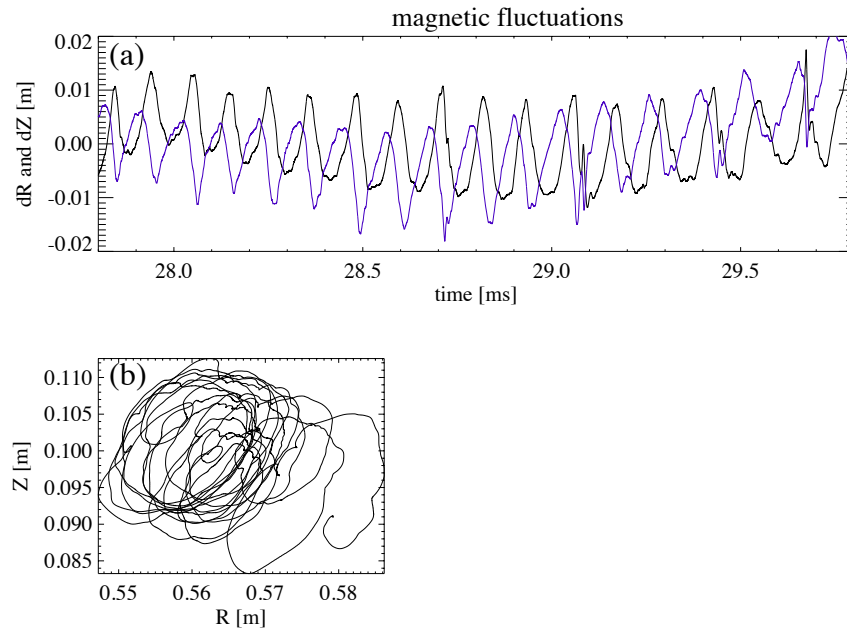
Figure 4.8.9: Time evolutions of poloidal (black) and radial (purple) magnetic fluctuations measured by the composite probe system (a) and the trajectory in R-Z plane (b). Here, R and Z is calculated by Eq. (4.8.1).
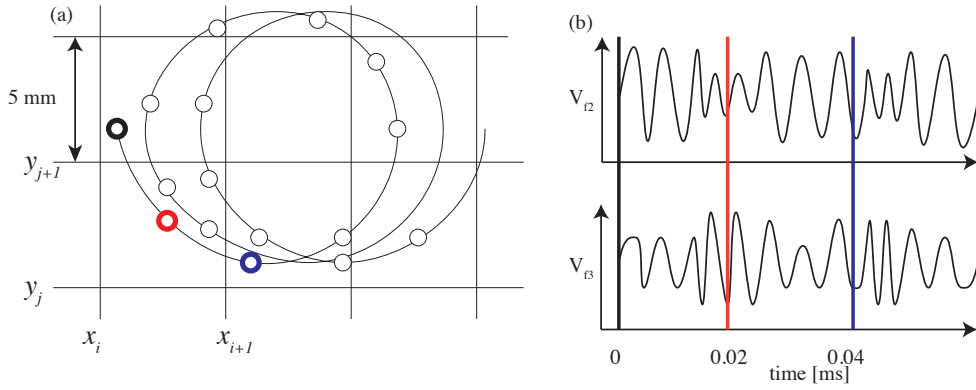
Figure 4.8.10: Schematic view of the mapping of the long range correlation of probe 2 and probe3. The reconstructed magnetic field line is shown in a solid curve in (a). Each open circle has an analysis results derived from the 0.02 ms time window shown in (b). The same colors in both figures represent the correspondence between the data. The data in the same grid are ensemble averaged to calculate the correlation.
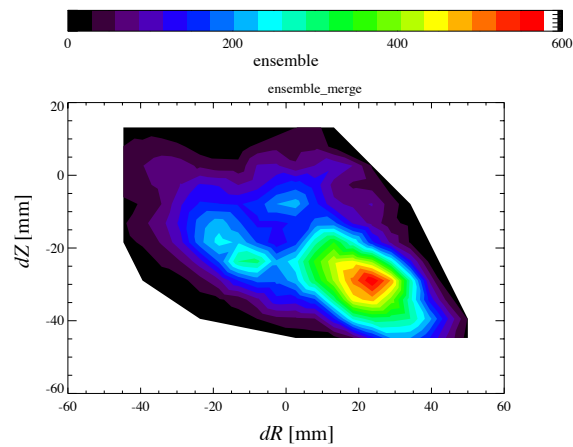
Figure 4.8.11: 2D-map (in dR-dZ plane) of the number of ensemble N_{ij} for each location.
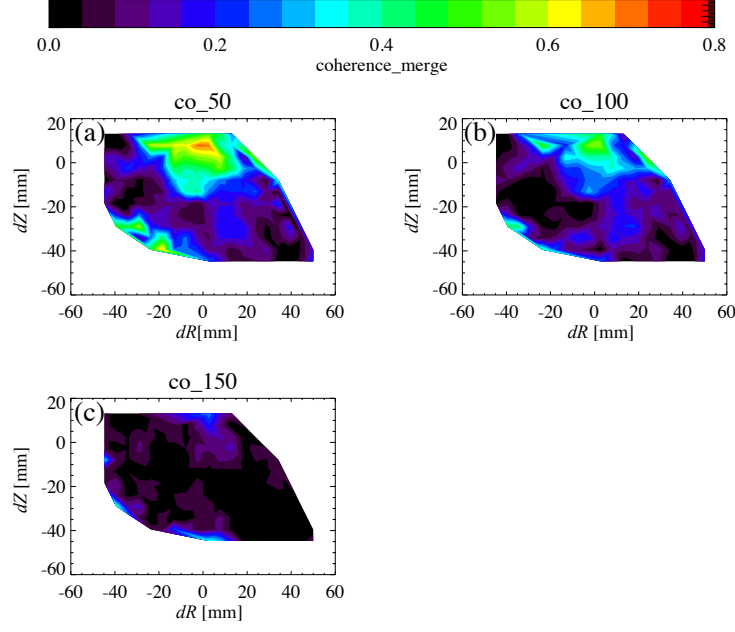
Figure 4.8.12: 2D-map (in *dR-dZ* plane) of the cross-coherence of $V_f s$ measured by probe 2 and probe 3. Maps for 50 kHz (a), 100 kHz (b), 150 kHz (c) are plotted.
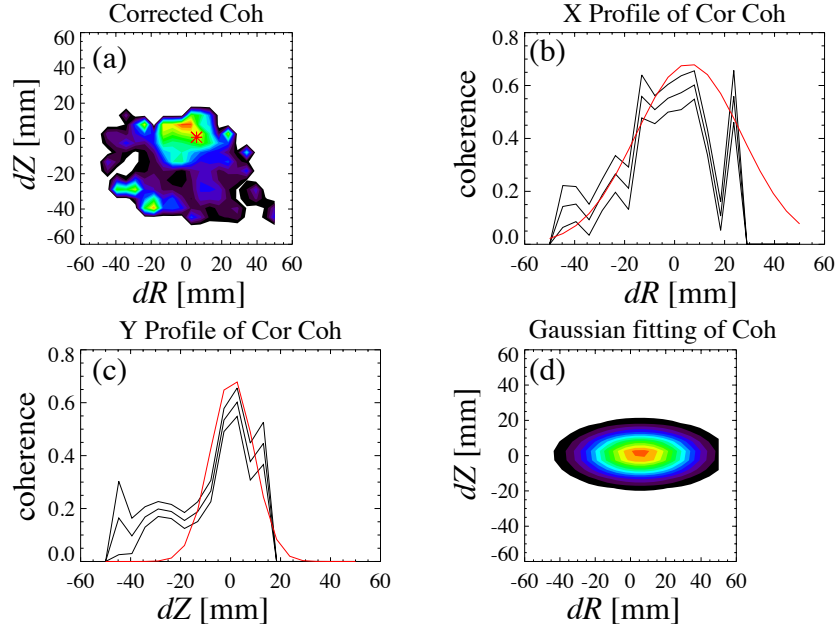
Figure 4.8.13: 2D-map (in *dR-dZ* plane) of the coherence of $V_f s$ at 50 kHz (a), and cutaways along *dR* (b) and *dZ* (c) with Gaussian fitting curves (red). The 2D-map of the gaussian fitting curve (d) is also shown. $1/e$ widths of the Gaussian functions are $\delta R = 30$ mm and $\delta Z = 12$ mm.
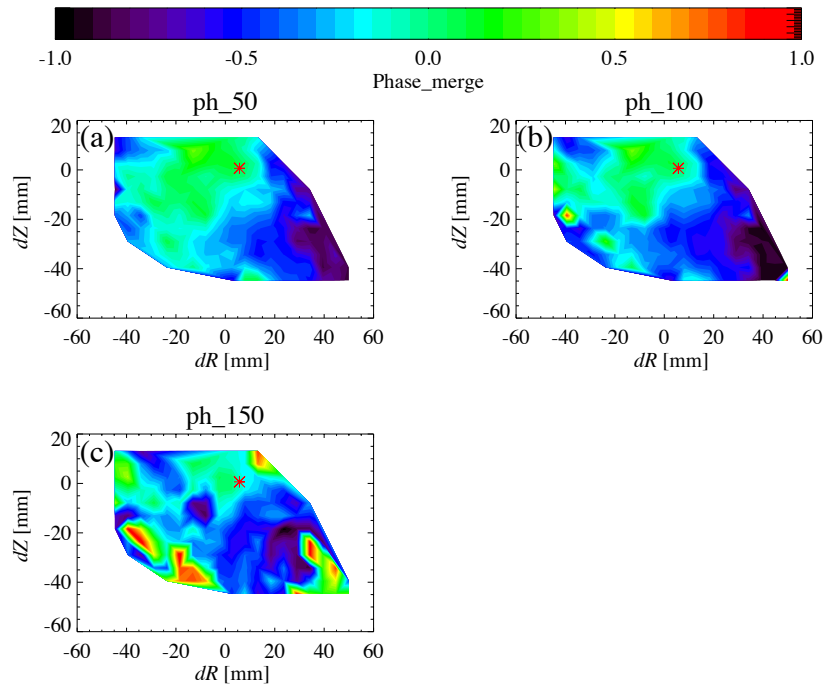
Figure 4.8.14: Comparison of phase differences of $V_\mathrm{f}s$ measured by probe 2 and probe 3. 2D maps for 50 kHz (a), 100 kHz (b), 150 kHz (c) are plotted. Red asterisks indicate the location of the highest correlation.
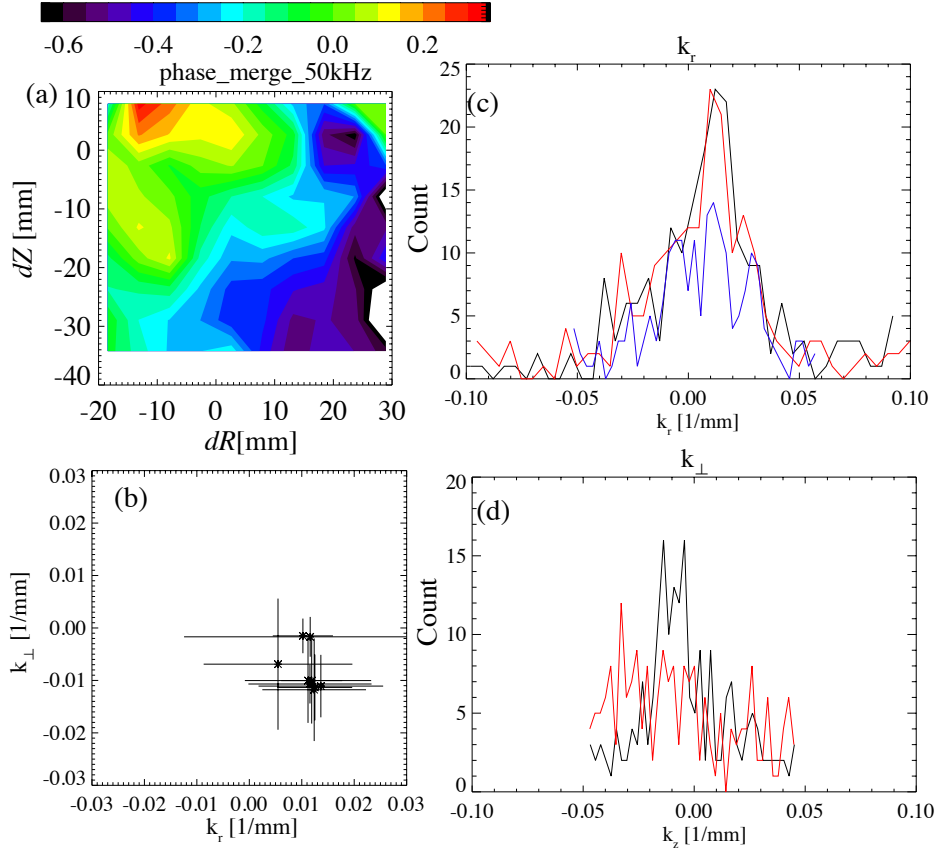
Figure 4.8.15: Enlarged view of Fig. 4.8.14 (i.e., the cross-phase at 50 kHz) (a), wavenumbers k_r and $k_\perp$ derived from linear fitting of the long distance correlation (b) and wavenumber spectra of k_r (c) and $k_\perp$ (d) derived from the two point correlation of electrodes in probe 2. $k_\perp$s and k_rs calculated by both methods roughly agreed. Each symbol in (b) represents the linear fitting of each coordinate in (a), and each error bar corresponds to the standard deviation of each linear fitting. The black, red and blue curves in (c) represent k_rs derived from V_{f1} and V_{f2}, from V_{f1} and V_{f3}, from V_{f1} and V_f at the side electrode. The black and red curves represent $k_\perp$s derived from V_{f2} and V_{f3}, and from V_fs at the side electrodes.

4.9 Summary of the analysis results

In this section, we summarize the analysis results. We have investigated the structure of edge plasma turbulence of TST-2 using Langmuir probes, and magnetic coils. The large amplitude fluctuations of V_f, T_e, n_e and B are observed at 10 kHz. The amplitude of magnetic field fluctuation is $\tilde{B}_r/B_T = 10^{-2}$. The fluctuation up to 20 kHz shows a dispersion relation clearly different from that at higher frequencies, and we call this MHD type fluctuation. Figures 4.3.5, 4.8.6 show $k_\parallel$ of MHD type fluctuation is very small compared to $k_\perp$, showing $|k_\parallel| < 10^{-4}$ mm^{-1} and $k_\perp = -0.004 \pm 0.001$ mm^{-1}. The following table (Table 4.9.1) shows the obtained parameters of $k_\perp$, $k_\parallel$, k_r, $\sigma_{k_\perp}$, $\sigma_{k_\parallel}$ and σ_{k_r} at 10 kHz and 100 kHz at $R = 560$ mm.

	$k_\perp$	$k_\parallel$	k_r	$\sigma_{k_\perp}$	$\sigma_{k_\parallel}$	σ_{k_r}
10 kHz	-0.004 mm^{-1}	0 mm^{-1}	0.005 mm^{-1}	0.004 mm^{-1}	0.004 mm^{-1}	0.005 mm^{-1}
100 kHz	-0.04 mm^{-1}	0.01 mm^{-1}	0.01mm^{-1}	0.01mm^{-1}	0.01mm^{-1}	0.01mm^{-1}

Table 4.9.1: $k_\perp$, $k_\parallel$, k_r, $\sigma_{k_\perp}$, $\sigma_{k_\parallel}$ and σ_{k_r} at 10 kHz and 100 kHz at $R = 560$ mm.

Electrostatic particle flux Γ_r is evaluated from $\langle \delta n \delta E_\theta \rangle / B$. Γ_r is dominated by MHD type fluctuation, and the calculated diffusion coefficient is 10 m^{2}s^{-1} at $R = 560$ mm. This value is comparable to D_{Bohm}.

The toroidal correlation length of MHD fluctuation is about 5 m and the poloidal correlation length is 3.5 m. RR diffusion coefficient is evaluated as $D_{st} = 10$ m^{2}s^{-1}.

The cross coherence of $\tilde{V}_f$s of the two probes separated by about 1 m along a field line shows a high correlation of 0.7. Both correlation and cross phase oscillate at 10 kHz, and amplitude modulation of $\tilde{V}_f$ indicates that turbulence structure is frozen to the magnetic field line and oscillates in the poloidal cross section with the MHD fluctuation. We reconstructed the spatial structure of turbulence by tracing the trajectory of the field line. The profile of the coherence at 50 kHz shows decay lengths $\delta R = 30$ mm and $\delta Z = 12$ mm. These roughly agree with the result of $\sigma_{k\perp} \sim \sigma_{kr} \sim 0.05$ mm^{-1}, which are the spectral widths of wavenumber at 50 kHz estimated by two point correlation analysis.

4.10 Discussion

In order to understand the characteristics of edge turbulence in TST-2, we will discuss the following five issues.

Section 4.10.1. Comparison between TST-2 and other devices : Since TST-2 has a strong MHD fluctuation at 0-20 kHz, edge turbulence characteristics are different from those in conventional tokamaks. However, it also has similarities in the fluctuation at the frequency range of 20-150 kHz. We will compare the structures of turbulence in different devices.

Section 4.10.2. Radial profile of fluctuation : The radial profile of edge turbulence in TST-2 is summarized here. The reason why the turbulence levels of $\tilde{T}_e/T_e$, $\tilde{n}_e/n_e$, $e\tilde{V}_p/k_BT_e$ and $\tilde{B}_r/B_T$ are different from those in conventional tokamaks is discussed.

Section 4.10.3. Particle flux : The radial particle transport due to edge turbulence is evaluated here.

Section 4.10.4. Derivation of $k_\parallel$, $l_\parallel$ and $v_\parallel$: $k_\parallel$, $l_\parallel$ and $v_\parallel$ are obtained by three different ways in TST-2. Advantages and disadvantages of each method are presented.

Section 4.10.5. Mode structure of MHD fluctuation : A global MHD fluctuation with poloidal mode number $m \sim 2$ and toroidal mode number $n \sim 1$ is observed in TST-2. The peeling ballooning mode is the most probable candidate for the fluctuation, and the reason is presented here.

Here, sections 4.10.1. -4.10.4. are related to the four objectives presented in section 1.10. The second objective: clarification of the spatial dependence of turbulence, is separated into several parts, that is radial profile (section 4.10.2) and mode structure (section 4.10.4).

4.10.1 Comparison between TST-2 and other devices

In this section, we will compare the difference of the edge turbulence characteristics between conventional tokamaks, STs, and RFP devices. In conventional tokamaks, drift waves play major part in density and potential fluctuations at the plasma edge [14]. Typical radial profiles of edge turbulence are shown in Fig. 1.9.1. In TST-2, the relative plasma potential fluctuation, density and magnetic fluctuation levels inside the LCFS are much greater than those in conventional tokamaks.

Several experiments in conventional tokamaks show that there are clear differences in the features of turbulence between those inside the LCFS and those in far SOL region. One of the clear differences is the poloidal phase velocity of fluctuation. In conventional tokamaks, the phase velocity generally changes its sign from the electron diamagnetic drift direction inside the LCFS to the ion diamagnetic drift direction in the SOL [28]. This trend is also observed in RFP plasmas, which have larger magnetic fluctuations at the edge [75]. This change reflects the Doppler shift profile affected by the velocity shear layer just inside the LCFS [29]. In linear theories, drift waves can be divided into two different modes. One is the ion temperature gradient mode (ITG), which propagates in the ion diamagnetic direction with drift velocity $v_{di} = T_i/eB_TL_n$, and the other is electron temperature gradient mode (ETG), which propagates in the electron diamagnetic direction with drift velocity $v_{de} = T_e/eB_TL_n$, where L_n is the density gradient at the plasma edge. Unfortunately, it is not obvious which mode is dominant in tokamak plasmas, since fluctuation does not necessarily follow the dispersion relation of each mode. Some simulations suggest the ion temperature gradient mode plays major role in turbulent transport inside the LCFS [4].

In TST-2, the experimental dispersion relation of potential fluctuation can be divided in two parts as shown in Fig. 4.3.3. One is the fluctuation at the frequency range of $0 \sim 20$ kHz, and the other is the fluctuation at $20 \sim 150$ kHz. The low frequency part can be considered as MHD type fluctuation, since the coherence between magnetic fluctuation and floating potential is high, and the poloidal wavenumber is small.

The fluctuation at $20 \sim 150$ kHz shows a phase velocity of about 4000 m/s inside the LCFS in the electron diamagnetic direction, and propagates in the ion diamagnetic direction in the far SOL region as shown in Fig. 4.3.5 (e). This profile is consistent with the drift wave profile in conventional tokamaks. Thus, the fluctuations at $20 \sim 150$ kHz are probably the drift wave turbulence. The flow velocity derived from $E \times B$ flow is $\frac{E_r}{B_T} \sim 6000$ m/s inside the LCFS. The phase velocity of $\tilde{V}_f$ is 4000 m/s, and the electron drift velocity is $v_{de} \sim -1500$ m/s. These values satisfy the condition of

$$\frac{E_r}{B_T} + v_{de} \sim v_{ph}, \tag{4.10.1}$$

where v_{ph} is the phase velocity of the fluctuation in the laboratory frame. Thus, Doppler shift of the ETG mode by the flow shear can account for the phase velocity inside the LCFS.

The parameters of edge plasma inside the LCFS in TST-2 is summarized as follows.

Magnetic field	0.12 T
Electron temperature	20 eV
Electron density	$6 \times 10^{19} \mathrm{m}^{-3}$
Gradient scale length	0.1 m
Drift velocity v_{de} in static frame	-1500 m/s
Wavenumber $k_{\perp}$	2-20 m^{-1}
E_r/B_T	6000 m/s
V_p from mach probe	10000 m/s
V_t from mach probe	-10000 m/s
Phase velocity at 0-20 kHz	1000 m/s
Phase velocity at 20-100 kHz	4000 m/s

Table 4.10.1: The parameters of edge plasma inside the LCFS in TST-2.

When we assume that the plasma mean flow driven by $\boldsymbol{E} \times \boldsymbol{B}$ causes Doppler shift of the fluctuation, the relation between the frequency of fluctuation in laboratory frame ω_L, the frequency of fluctuation in stationary frame ω_0 and the mean flow becomes as follows using the variables in Table 4.10.1.

$$(\omega_L - \omega_0)/k_{\perp} = V_p \cos \alpha + V_t \sin \alpha, \qquad (4.10.2)$$

where the toroidal rotational velocity V_t is the order of ~ -10000 m/s as shown in Fig. 4.5.1 (a), the poloidal phase velocity is also $V_p \sim 10000$ m/s and α is the magnetic field angle of $\sim 20°$. $k_{\parallel}$ is approximated as 0. The right hand side becomes ~ 6000 m/s here, and this is consistent with $\boldsymbol{E} \times \boldsymbol{B}$ velocity of E_r/B_T. When ω_0 is taken as the ETG mode drift wave, $\omega_0/k_{\perp} = v_{de}$ and $\omega_L/k_{\perp}$ becomes the phase velocity at 20-100 kHz, and the left hand side becomes ~ 5500 m/s. Therefore, the Doppler shift is considered to be caused by perpendicular flow measured by the mach probe.

In TST-2, the edge turbulence at 0-20 kHz does not change the propagation direction. Since the MHD fluctuation has a long correlation lengths, it is a global mode. Therefore, it is reasonable that the global structure (i.e., large scale structure) tends to show a rigid body rotation.

4.10.2 Radial profile of fluctuation

Figure 4.10.1 shows the radial distribution of the relative rms fluctuation levels for electron temperature $\tilde{T}_e/T_e$, density $\tilde{n}_e/n_e$, potential $e\tilde{V}_\mathrm{p}/kT_e$ and radial magnetic field $\tilde{B}_r/B_T$ in TST-2. Solid curves are the fitted cubic functions obtained by a least square method. In the calculation we include only the frequency components from 0.5 kHz (which is limited by the time window of 2 ms) to 200 kHz (which is the upper limit in the $\tilde{T}_e$ and $\tilde{n}_e$ measurements using V-I curves). $e\tilde{V}_\mathrm{p}/kT_e$ is huge at the far SOL region (~ 650 mm). The Boltzmann relationship is roughly satisfied inside the LCFS ($\tilde{n}_e/n_e = e\tilde{V}_\mathrm{p}/k_BT_e$). However, the fluctuation levels of potential rise significantly in the far edge region ($R > 600$ mm). The profile of $\tilde{n}_e/n_e$ has a similar radial shape as that of of $\tilde{B}_r/B_T$, but its level is much smaller than $\tilde{n}_e/n_e$. $\tilde{T}_e/T_e$ profile shows smaller values than $\tilde{n}_e/n_e$ and $e\tilde{V}_\mathrm{p}/kT_e$ inside the LCFS, and its fluctuation level becomes comparable to $\tilde{n}_e/n_e$ outside the LCFS. The radial distribution of each parameter is quite different from that of conventional tokamaks (Fig. 1.9.1). $\tilde{n}_e/n_e$ increases from about 0.05 inside the LCFS to about 0.6 in the far SOL region in conventional tokamaks, whereas in TST-2, $\tilde{n}_e/n_e \sim 0.5$ inside the LCFS is observed. The large differences in the profiles and levels between those in TST-2 and conventional tokamaks can probably be attributed to the large MHD fluctuation in TST-2. Therefore, we should discuss the MHD fluctuations and the high frequency fluctuations (i.e., drift waves) separately. In the following firstly, we discuss the high frequency fluctuations. Secondly we discuss the MHD fluctuations.

In conventional tokamaks, $e\tilde{V}_\mathrm{p}/k_BT_e$ has a peak just inside the LCFS, while $\tilde{n}_e/n_e$ and $\tilde{T}_e/T_e$ are constantly increasing across LCFS as shown in Fig. 1.9.1. This peak of $\tilde{V}_\mathrm{p}$ in conventional tokamaks indicates that energy flux due to electrostatic fluctuation has a peak just inside the LCFS and decreases towards the plasma core. The fluctuation peak inside the LCFS arises from the steep gradient of pressure profile. The resultant large diffusion coefficient is due to small electron-ion mean free path which comes from the low edge temperature [76].
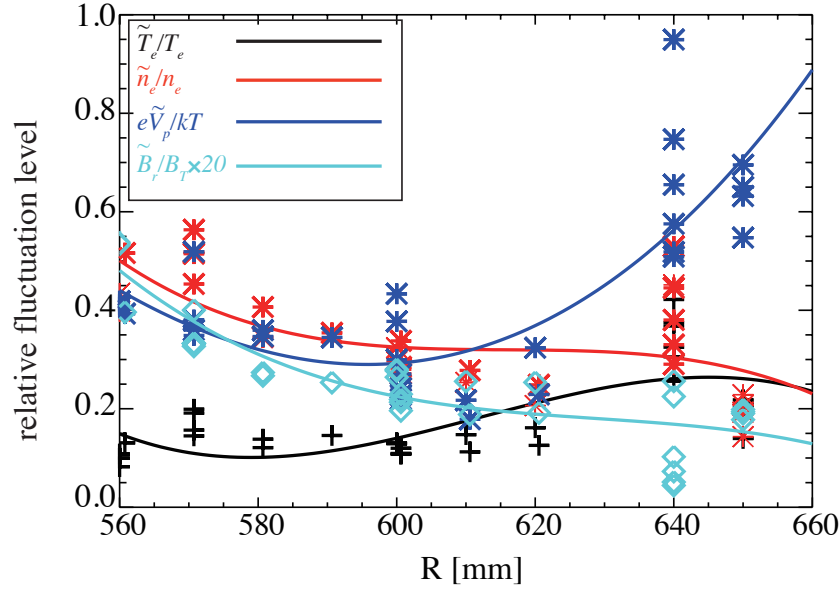
Figure 4.10.1: Relative fluctuation levels of density (red), potential (blue), temperature (black) and magnetic field (sky blue) in TST-2.

In TST-2, $\tilde{V}_f$ of 20-150 kHz has a peak around the LCFS, as shown in Fig. 4.10.2. Figure 4.10.2 shows the two dimensional power spectrum of $\tilde{V}_f$ and $\tilde{I}_{is}$ at the frequency of 20 kHz and 100 kHz. Both V_f and I_{is} monotonically decrease in radial direction at 20 kHz. However, the amplitude of $\tilde{V}_f$ at 100 kHz has its peak around the LCFS at $R = 585$ mm.

This peak is seen only in $\tilde{V}_f$ profile, and not observed in $\tilde{n}_e$ and $\tilde{B}_r$ profile. These features in TST-2 are similar to those in conventional tokamaks. The result supports the previous speculation that the fluctuation of 20-150 kHz in TST-2 is the drift wave type (Sec. 4.10.1).

In conventional tokamaks, $\tilde{T}_e/T_e$ and $\tilde{n}_e/n_e$ increase monotonically with the radius at the edge. In the far SOL region, density and temperature fluctuation levels increase due to the presence of a bursty phenomenon called a plasma blob [76]. A blob is an intermittent structure, spatially separated from the core plasma. It propagates across the SOL toward the outer wall, causing energy and particle fluxes. The plasma blob is considered to be one of the main causes of the density fluctuation outside the LCFS [77]. The increase of $\tilde{T}_e/T_e$ and $\tilde{n}_e/n_e$ is also observed in RFP devices, which has larger magnetic fluctuation levels than those of tokamaks. Difference is seen in the relative fluctuation levels. In RFP plasma, temperature fluctuation shows $\tilde{T}_e/T_e \sim 0.5\tilde{n}_e/n_e$, while $\tilde{T}_e/T_e \sim (0.3 - 0.4)\tilde{n}_e/n_e$ is satisfied in conventional tokamaks [78].

In TST-2, profile of $\tilde{T}_e/T_e$ increases monotonically like conventional tokamaks and RFPs. However, $\tilde{n}_e/n_e$ does not show an increasing trend. The reason can be interpreted as follows. In far SOL region at ~ 650 mm, the wall of the vacuum vessel is very close to the Langmuir probes. Thus, the structure of the vacuum vessel like limbs can block the plasma blob, and this effect reduces the amplitude of density fluctuation.

The relative amplitude of the magnetic field $\tilde{B}_r/B_T$ decreases monotonically in conventional tokamaks, and also in RFP plasmas, the relative amplitude of the magnetic field decreases constantly at the edge [72]. RFP plasmas have strong magnetic field fluctuations of $\tilde{B}_r/B_T \sim 10^{-2}$, and the power spectra of $\tilde{B}_r$ are concentrated in the frequency range below 20 kHz, indicating the presence of global fluctuation. This feature is similar to that of TST-2 , and consistent to the fact that the fluctuation of $\tilde{B}_r/B_T$ mainly consists of global MHD modes. Global MHD modes often form a region called a magnetic island, a closed field line region located around the corresponding resonant rational surface, where the safety factor becomes resonant (i.e., $q = m/n$) to the mode numbers m, n of the mode [79]. Figure 4.10.3 shows the phase differences between $\tilde{B}_r$ and $\tilde{n}_e$, $\tilde{B}_r$ and $\tilde{T}_e$ and $\tilde{B}_r$ and $\tilde{B}_\theta$ at $R = 560$ mm. When the fluctuation is an ideal MHD mode, the fluctuation is caused by (a rotation of) a deformed flux surface and the parameters which are constant on a flux surface should show in-phase fluctuations. Note that B_r is a derivative (i.e. inclination) of the flux surface, and it should show a 90°
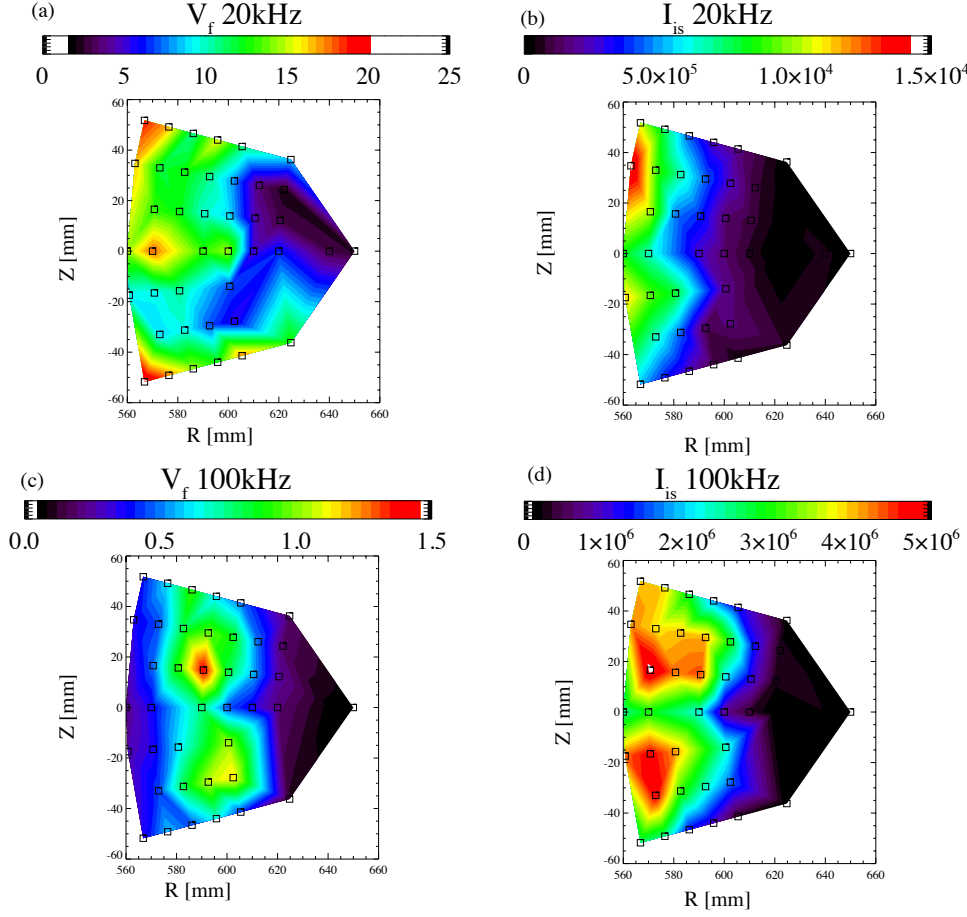
Figure 4.10.2: Two dimensional power spectra of V_f (a) and I_{is} (b) at 20 kHz (top) and 100 kHz (bottom).

degree phase difference from other parameters. As shown in Fig. 4.10.3, $\tilde{B}_\theta$, $\tilde{T}_e$ and $\tilde{n}_e$ are shifted by almost 90°, respectively. These results suggest that the MHD fluctuations are dominated by ideal MHD modes. Above 20 kHz, the phase of $\tilde{n}_e$ and $\tilde{T}_e$ starts to decrease, suggesting that the fluctuations are different from the ideal MHD mode. In contrast, $\tilde{B}_\theta$ and $\tilde{B}_r$ shows the same phase relation up to 60 kHz, indicating that the magnetic fluctuations are mainly due to the ideal MHD mode. It should be noted that a pure ideal MHD mode does not induce transport, thus the other modes or waves, such as resistive MHD mode and drift waves, are mixed and play important roles even in the frequency range < 20 kHz (see Sec. 4.10.3).

4.10.3 Particle flux

The radial electrostatic particle transport due to edge turbulence is usually evaluated from edge turbulence measurements by assuming that the local radial drift velocity is given by $v_r = E_\theta/B_T$, so that

$$\Gamma_r = \langle \tilde{n}\tilde{v}_r \rangle = \langle \tilde{n}\tilde{E}_\theta \rangle / B_T .$$ (4.10.3)

Normally, the particle transport has a peak just inside the LCFS and decreases radially like potential fluctuation. In conventional tokamaks, it is confirmed that electrostatic turbulent flux could explain the whole radial transport [80]. In the far SOL region, some experiments suggest that intermittent plasma blob propagation is responsible for some part of the particle transport, but this effect is negligible inside the LCFS [29]. Despite the large amplitude magnetic field fluctuations in RFP plasmas, the radial energy and particle transports are mainly caused by electrostatic fluctuations [78]. This leads to the expectation that the electrostatic fluctuations dominate the radial particle transport in TST-2.

In TST-2, the radial particle transport derived from electrostatic fluctuation is $6 \times 10^{20}\,\mathrm{m^{-2}s^{-1}}$, and it decreases constantly with the radius as shown in Fig. 4.4.2. This profile is similar to that of conventional tokamaks.
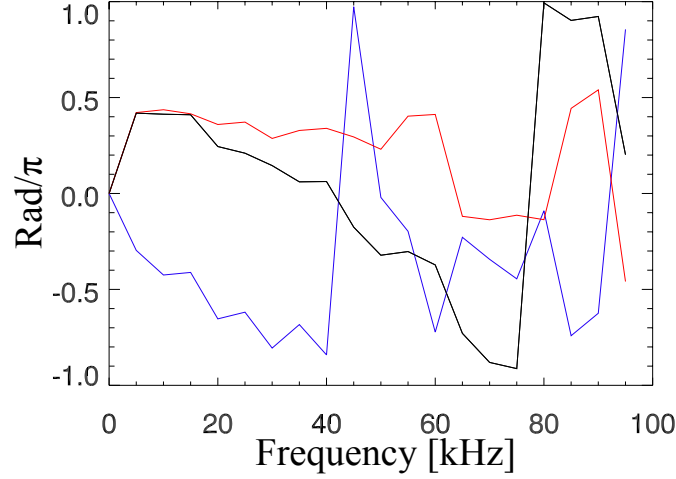
Figure 4.10.3: The phase difference between $\tilde{B}_r$ and $\tilde{n}_e$ (black), $\tilde{B}_r$ and $\tilde{T}_e$ (blue) and $\tilde{B}_r$ and $\tilde{B}_\theta$ (red) at $R = 560\,\text{mm}$.

The diffusion coefficient estimated from Γ_r is $10\,\text{m}^2\text{s}^{-1}$ at $R = 560$ mm. This value is comparative to D_{Bohm}. However, the total flux shows a decreasing trend with the radius. This is not consistent with $D_{Bohm} = kT_e/16eB$, because T_e is roughly constant in 560 mm $< R <$ 620 mm.

Figure 4.4.1 shows that the particle flux is dominated by the low frequency components less than 20 kHz. However, Fig 4.10.3 suggests that the fluctuation in the frequency range < 20 kHz is mainly composed of an ideal MHD mode, which does not induce transport by itself alone. This indicates that the other modes or waves, such as resistive MHD modes and drift waves, which induce transport are mixed with the ideal MHD mode. Here we would like to point out the possibility that the transport due to the other modes may be enhanced by the background large amplitude ideal MHD modes.

D_{Bohm} is a semi-empirical diffusion coefficient observed in the early plasma experiments [4]. This value is used as an indicator of diffusion for historical reason. Decrease of D_r compared to D_{Bohm} suggests that the radial transport caused by plasma turbulence is relatively suppressed with the increase of radius.

RR diffusion coefficient D_{st} is negligible in conventional tokamaks. Magnetic fluctuation levels in conventional tokamaks is $\tilde{B}_r/B_T \sim 10^{-4} - 10^{-5}$ inside the LCFS, and has only negligible effect on edge transport [71] [81]. However, it is confirmed that the amplitude of magnetic fluctuation becomes large with small safety factor $q(a)$ in the Tokapole II [82]. This is consistent with the strong magnetic fluctuation at the edge in TST-2, where $q(a)(\sim 2.5)$ is small at the edge. In TST-2, the diffusion coefficient derived from Rechester-Rosenbluth theory is the same order as the diffusion coefficient derived from the electrostatic radial transport. This is due to the large correlation length of the MHD fluctuation $l_\parallel$. The magnetic fluctuations in STs are not always large compared to those in conventional tokamaks. The strong magnetic field fluctuation of $\tilde{B}_r/B_T > 10^{-3}$ is only observed in PEGASUS in Table 1.9.1. The low edge temperatures in TST-2 and PEGASUS imply a high resistivity, which leads to resistive MHD instabilities [13]. As we will discuss in Sec. 4.10.5, peeling ballooning mode driven by $J_\parallel/B$ can be unstable in TST-2. Thus, the low edge temperature, the small safety factor and the high $J_\parallel/B$ are the candidate origins of the strong magnetic fluctuations in these STs.

4.10.4 Derivation of $k_\parallel$, $l_\parallel$ and $v_\parallel$

In this experiment, $k_\parallel$, $l_\parallel$ and $v_\parallel$ are derived in three different ways. One is from the two point correlation of electrodes at the same composite probe inserted at the low field side midplane. Another is from the correlation between two separate probes along a field line. The third one is the method using the correlation between the magnetic coil array fixed at the vacuum vessel wall and the magnetic coil inside the composite probe. The first method is highly reproducible in the experiments, since we don't need to place the multiple probes at proper locations, unlike other methods. However, this leads to larger errors in evaluating $k_\parallel$ and $l_\parallel$, since the distance between two electrodes in the composite probe is much smaller than $l_\parallel$. While $l_\parallel$ is thought to be the order of

meters, the distance between the electrodes of the composite probe is just ~ 10 mm. Thus, it is more preferable to use the correlation between the two probes separated by ~ 1 m.

The third method is also reproducible, but this method cannot measure $k_\parallel$ and $l_\parallel$ directly, since the magnetic coil array fixed at the vacuum vessel wall is far from the plasma, and we cannot put other probes and the magnetic coil array on the same field line.

The values obtained by each method are consistent. Both $k_\parallel$ obtained by the first and the second method show 0.01 mm^{-1} at 100 kHz. $k_\parallel$ cannot be obtained by the third method, since it is impossible to put two different coils on the same magnetic field line, and the phase difference between probes is highly sensitive to the location of the probe.

The parallel correlation length $l_\parallel$ obtained by the correlation between the two separate probes (probe 2 and probe 3) is ~ 2 m at 10 kHz, while $l_\parallel$ obtained by the magnetic coil array is ~ 5 m. This discrepancy is reasonable since the magnetic coil array is not placed on the same magnetic field line, and the magnetic field fluctuations are sensitive to the currents far from the coils.

At 100 kHz, $l_\parallel \sim 1$ m is calculated from the correlation between the two separate probes, while $l_\parallel$ obtained by the electrodes at the same probe is ~ 0.1 m and 0.2 m by the magnetic coil array. The latter short lengths can be interpreted by the contamination of the perpendicular components with short correlation length $l_\perp \sim 0.01$ m. The value obtained from the two separate probes is more reliable, since the contamination can be ruled out in the 2D-map of the coherence. Unlike MHD fluctuation where $l_\perp$ and $l_\parallel$ are comparable, small deviation from the magnetic field line leads to large errors of $l_\parallel$.

Connection length inside the LCFS, which is the length of a magnetic field to complete a poloidal turn, is $L_c = 2\pi R q$. In TST-2, $L_c \sim 10$ m just inside the LCFS. Thus, L_c is greater than $l_\parallel$s of both MHD and drift wave fluctuations. This implies that both fluctuations should not be expressed by a two-dimensional model, since fluctuations lost the information before magnetic field lines complete a poloidal turn. This fact indicates that the effect of the 3D turbulence structure needs to be included in the edge turbulence theories or numerical simulations.

The phase velocity along the field line $v_\parallel$ can only be evaluated by the two separate probes along the field line. This is because $v_\parallel > 10^6$ m/s is very large, and the phase difference of fluctuations between adjacent electrodes in the composite probe is too small to be detected. This value is obtained from the phase difference $\Delta\theta < 0.1\pi$ rad at 100 kHz between the two probes. Note that the Alfven speed is approximately $v_A \sim 10^8$ m/s, the electron thermal speed is $v_{th,e} \sim 2 \times 10^6$ m/s, and the ion thermal speed is $v_{th,i} \sim 4 \times 10^4$ m/s. Thus, there is a possibility that fluctuations propagate with Alfven wave speed or electron thermal speed along the field line.

Figure 4.8.13 shows that the radial decay length of the coherence map is $\delta R = 30$ mm and the poloidal decay length is $\delta Z = 12$ mm. Furthermore, Fig. 4.8.15 (c) and (d) show $\sigma_{k_r} \sim \sigma_{k_\perp} \sim 0.05$ mm^{-1}. This leads to the correlation lengths of $1/\sigma_{k_r} = 1/\sigma_{k_\perp} = 20$ mm. These values are different from the correlation lengths in conventional tokamaks: $L_{pol} \sim 0.5 - 5$ cm and a radial correlation length $L_{rad} \sim (0.5 - 1)L_{pol}$. However, the obtained poloidal decay length may be underestimated, because the whole profile of the coherence was not measured (Fig. 4.8.13 (c)), resulting a factor of 1-3 times shorter decay length. Thus, we should conclude that the perpendicular correlation lengths are not inconsistent with the previous results in conventional tokamaks.

The results in Sec. 4.8 indicate that $k_\parallel \sim 0$, and the drift wave structure oscillates with the MHD fluctuation, without changing the correlation length $l_\perp$ and l_r so much. Thus, the fluctuation of the drift wave is considered to be frozen to the MHD fluctuation, and the direct nonlinear contribution of the magnetic fluctuation to the turbulence seems to be small. If the fluctuations are completely frozen to the MHD fluctuation, the magnetic field fluctuation just deforms the geometry of the flux surface, and it does not generate additional (i.e., non linear) particle flux. Even if the fluctuations are frozen to the magnetic field lines, particles can diffuse through the RR diffusion process derived in Sec. 4.7. The actual particle transport due to RR diffusion can be smaller than the estimated value, when the magnetic structures are not fully stochastic. On the other hand, the phase difference between $\tilde{n}$ and $\tilde{V}_{\mathrm{f}}$ shows finite values of $-0.5\pi \sim -0.3\pi$ at the MHD frequencies. As a result, the electrostatic transport $\Gamma = \left\langle \tilde{n}\tilde{E}_\theta \right\rangle / B$ is dominated by the MHD fluctuations rather than the drift wave fluctuations.

4.10.5 Mode structure of MHD fluctuation

The small poloidal mode number $m \sim 2$ and toroidal mode number $n \sim 1$ suggest that large MHD activities observed at the edge in TST-2 are caused by a peeling ballooning mode.

A peeling ballooning mode is a type of instability localized in the edge, driven by pressure gradient ∇p and current density in the edge region and characterized by low toroidal mode number n [34]. Owing to its low toroidal field strength for a given plasma current I_p, a spherical tokamak naturally leads to high values of $J_{\parallel}/B$, which is the driving force of the instability [70]. The MHD fluctuation observed in PEGASUS, the spherical tokamak which has similar parameters to TST-2, is identified as a peeling ballooning mode [7]. The peeling ballooning mode becomes unstable at the edge of limited plasmas in a low aspect ratio tokamak under the conditions of high edge current density ($J_{edge} \sim 0.1\,\mathrm{MA/m^2}$), steep pressure gradient ($\nabla p \sim 600\,\mathrm{Pa/m}$) and low magnetic field ($B_T \sim 0.1\,\mathrm{T}$) [7]. This condition is satisfied in TST-2 where $J_{edge} \sim 0.3\,\mathrm{MA/m^2}$, $B_T \sim 0.1\,\mathrm{T}$ and $\nabla p \sim 500\,\mathrm{Pa/m}$ at the plasma edge [83]. Thus, it is quite natural to observe the same mode in TST-2. Since the peeling ballooning mode has a nature of ideal MHD mode and the observed mode is mainly an ideal MHD mode (Sec. 4.10.3), the large magnetic fluctuations in TST-2 is probably the peeling ballooning mode.

Chapter 5

Conclusion

In fusion plasma research, the study of anomalous transport induced by plasma turbulence is important for achieving fusion relevant high temperature and high density plasmas. Recent research on turbulence is mainly focused on the new paradigm of plasma turbulence in the view of suppressing the transport flux and obtaining optimized discharge conditions (e.g. high confinement mode called H-mode). In magnetically confined plasmas, various types of fluctuations are induced due to plasma instabilities. These fluctuations cause anomalous transport, and the plasma confinement is deteriorated as a result. In previous research of conventional tokamaks, these transports are thought to be caused mainly by drift waves driven by the pressure and temperature gradients, and the contribution of magnetic fluctuations is believed to be negligible. A spherical tokamak (ST) can confine high pressure plasma with a relatively weak magnetic field strength and is very attractive as a fusion reactor from an economic point of view. However, magnetic fluctuations could be large in ST plasmas, where the high pressure, the weak magnetic field strength (i.e. the low safety factor) and the large plasma current may enhance magnetic fluctuations through instabilities. At the edge region, we should also consider the effect of resistivities due to a relatively low temperature. When the magnetic fluctuations are strong, the field lines become stochastic and the transport along the field lines deteriorates the confinement. In addition, such stochastic field would affect the other intrinsic instabilities. Therefore, understanding the structure of magnetic fluctuations and their effects on plasma turbulence in an ST is important.

For edge turbulence measurements, Langmuir probes are very useful because it has a better spatial resolution compared with the other diagnostics, and they can measure a wide variety of plasma quantities. In order to measure the temporal and spatial structures of edge turbulence in TST-2, we have developed two types of probe. The composite probe system consists of four electrodes on the front surface, the other four electrodes on the side and a 3-axis magnetic pickup coil. The electrodes are used as Langmuir probes, and floating potential V_f, ion saturation current I_{is}, electron temperature T_e, electron density n_e and plasma flows V_t, V_θ can be measured. Several electrodes are used simultaneously to obtain wavenumbers and correlation lengths. In addition to the composite probe system, we also installed two sets of four-electrode Langmuir probe at a different toroidal location separated by about 1 m from the composite probe system. These are used mainly to obtain parallel wavenumbers and parallel correlation lengths along a field line.

The observed fluctuations can be classified into two types: (i) the MHD type fluctuation characterized by a global structure and low frequencies (< 20 kHz), and (ii) the drift wave like fluctuations characterized by a smaller spatial scale and higher frequencies (> 20 kHz). In the following we list the major results obtained for the two types of fluctuations.

The major analysis results for the MHD type fluctuations are as follows.

1. The discharges are characterized by large MHD type fluctuations with the levels of $\tilde{B}_r/B_T = 10^{-2}$ inside the LCFS, and the level is much larger than those in conventional tokamaks.

2. Large amplitude oscillations in T_e, n_e, V_p are observed at the MHD frequency.

3. The phase difference of $\tilde{B}_r$, $\tilde{n}_e$ and $\tilde{T}_e$ indicates that the magnetic fluctuations are mainly due to the ideal MHD mode. Comparison of plasma parameters of TST-2 and PEGASUS indicates that the mode is probably a peeling ballooning mode. An ideal MHD mode does not induce transport by itself, thus the other modes play important role in the frequency range < 20 kHz.

4. $k_\parallel$ is almost 0, while $k_\perp = -0.004$ mm^{-1}, $k_r = 0.005$ mm^{-1}. These are evaluated for the fluctuations of V_f.

The drift wave like fluctuations show the following characteristics.

1. $k_\parallel$ at 100 kHz is 0.01 mm^{-1}, while $k_\perp = -0.04$ mm^{-1} and $k_r = 0.01$ mm^{-1}. Although these values are evaluated for V_f, the same values are expected for n_e, because the coherence between V_f and n_e is high.

2. $k_\perp$ shows constant phase velocity of about 4000 m/s in the electron diamagnetic drift direction inside the LCFS, and it changes its sign in the far SOL.

3. The high coherence of $\tilde{V}_\mathrm{f}$s along a field line up to 100 kHz indicates that this high frequency turbulence is frozen to the magnetic field line and oscillates with the slow MHD fluctuation.

4. The spatial structure of long range fluctuation is reconstructed by tracing the trajectory of the field line. The profile of the coherence at 50 kHz shows decay lengths $\delta R = 30$ mm and $\delta Z = 12$ mm. These values roughly agree with the result of the wavenumber spectral width $\sigma_{k_r} \sim \sigma_{k_\perp} \sim 0.05$ mm^{-1} at 50 kHz.

The following shows the similarities and differences between the turbulence in TST-2 and that in conventional tokamak.

1. The features such as frequencies, amplitudes and the poloidal propagation direction of drift wave type fluctuations are quite similar to those in conventional tokamaks. In conventional tokamaks, the phase velocity generally changes its sign from the electron diamagnetic drift direction inside the LCFS to the ion diamagnetic drift direction in the SOL. This trend is also observed in TST-2 plasmas, which is considered to reflect the Doppler shift of the drift wave caused by the velocity shear layer.

2. Magnetic turbulence in conventional tokamaks is typically $\tilde{B}_r/B_T \sim 10^{-5} - 10^{-4}$, and has a negligible direct effect on edge transport. Unlike the conventional tokamaks, TST-2 (and PEGASUS) shows quite a large fluctuation level $\tilde{B}_r/B_T \sim 10^{-2}$. On the other hand, the level in NSTX seems to be $\tilde{B}_r/B_T \sim 10^{-3}$ and the confinement is comparable to conventional tokamaks. Further studies are required to identify the origin of the large MHD fluctuation level, and its effect on confinement. The low edge safety factor, the high resistivity and the large current density, which induces a peeling ballooning mode, may be related to the large MHD fluctuation level.

The diffusion coefficients estimated from the fluctuations show the following values.

1. The electrostatic particle flux is dominated by the MHD fluctuation components. However, the fluctuation in the frequency range < 20 kHz is mainly an ideal MHD mode, and it does not induce transport by itself. This indicates that the other modes and/or waves which induce transport are mixed with the ideal MHD mode. The total flux is $\Gamma_r = 5 \times 10^{20}$ m^{-2}s^{-1}. The estimated radial diffusion coefficient $D_r = 10$ m^{2}s^{-1}. This value is factor of 2 higher than that of NSTX.

2. The correlation length of MHD fluctuation along the field line is about 5 m, and the RR diffusion coefficient is also estimated as $D_{st} = 10$ m^{2}s^{-1}. This coefficient and the radial diffusion coefficient due to the electrostatic fluctuation are the same in order, owing to the long correlation length of the MHD fluctuations. However, actual value of particle transport due to the RR diffusion can be smaller than the estimated value, since the correlation length of the MHD fluctuations is long and resultant magnetic field may not be so stochastic.

We have revealed the following detailed structure of turbulence in ST plasmas for the first time.

1. The parallel correlation length for the MHD type fluctuations is $l_\parallel \sim 2$ m, the average parallel wavenumber $k_\parallel$ is less than 0.0001 mm^{-1}.

2. The parallel correlation length for the drift wave type fluctuations is $l_\parallel \sim 1$ m at 100 kHz and the length decreases with frequency. The average parallel wavenumber is 0.01 mm^{-1}, and parallel phase velocity is $|v_\parallel| > 10^6$ m/s.

3. The drift wave type fluctuations are frozen to the magnetic field line and oscillate with the MHD fluctuation.

In summary, we have revealed the temporal and spatial structure of the edge turbulence in ST plasmas. There are similarities and differences between the structures in TST-2 (and the other ST) plasmas and those in conventional tokamak plasmas. The most prominent difference is that the level of MHD type fluctuations. The two dimensional turbulence measurement revealed that at the fluctuation can be divided in two parts, MHD fluctuation at 0-20 kHz and drift wave like fluctuation (> 20 kHz). The potential fluctuation frozen to the magnetic field line is also observed. The parallel wavelength and correlation length inside the LCFS are measured for the first time in STs and the results would be useful to benchmark theoretical models on the edge turbulence. For example, the correlation lengths shorter than the connection length imply that we should taken into account 3D effect in addition to the toroidal effect. The results acquired in this thesis will be the first step towards the understanding of edge turbulence in ST plasmas.
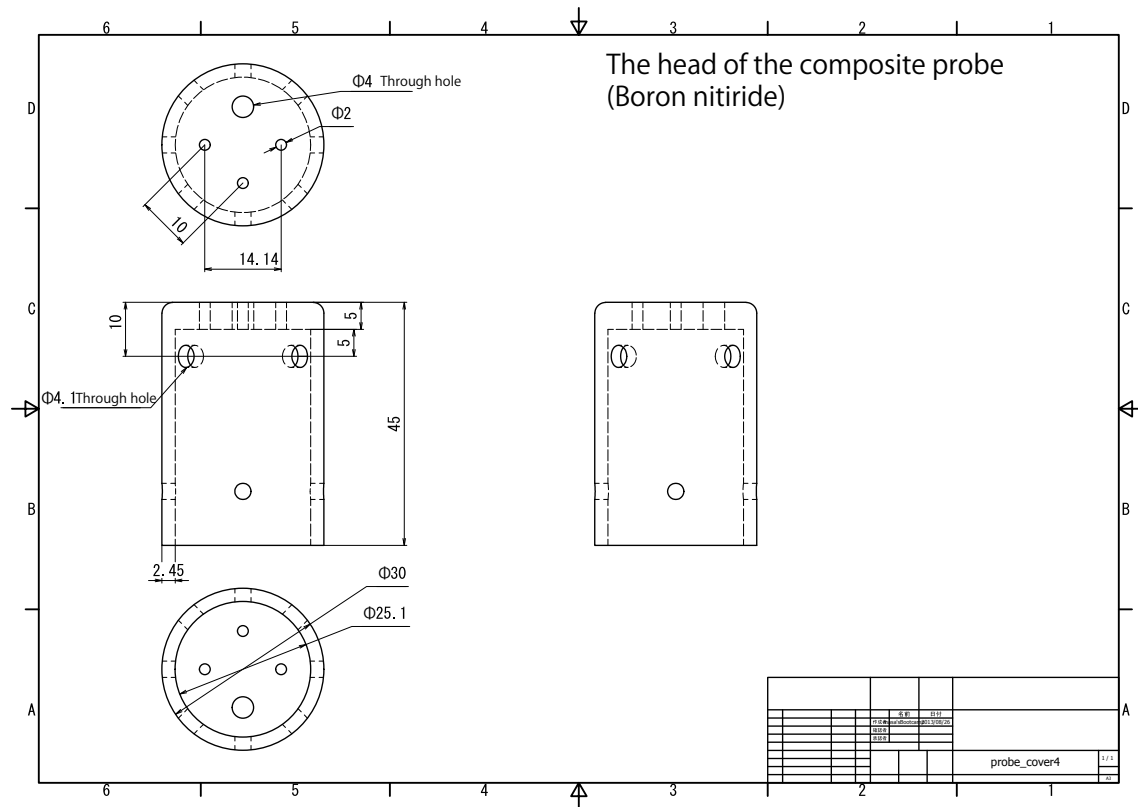
Appendix

The head of the composite probe
(Boron nitiride)

Φ4 Through hole
Φ2
10
14. 14

10
5
5
45
Φ4. 1Through hole
2. 45
Φ30
Φ25. 1

probe_cover4

Figure A1: The drawing of the the head of composite probe.

Acknowledgements

Bibliography

[1] K. Miyamoto, *Controlled Fusion and Plasma Physics*, Series in Plasma Physics and Fluid Dynamics, Oxford: Taylor & Francis (2006).

[2] Y. M. Peng and D. J. Strickler, "Features of spherical torus plasmas", Nuclear Fusion **26** (1986) 769.

[3] M. Greenwald, J. Terry, S. Wolfe, S. Ejima, M. Bell, S. Kaye and G. Neilson, "A new look at density limits in tokamaks", Nuclear Fusion **28** (1988) 2199.

[4] Y. Kishimoto, "Anomalous Transport", Journal of the Physical Society of Japan **12** (2000) 1280.

[5] A. Fujisawa, "A review of zonal flow experiments", Nuclear Fusion **49** (2009) 013001.

[6] G. R. Tynan, A. Fujisawa and G. McKee, "A review of experimental drift turbulence studies", Plasma Physics and Controlled Fusion **51** (2009) 113001.

[7] M. Bongard, R. Fonck, C. Hegna, A. Redd and D. Schlossberg, "Measurement of peeling mode edge current profile dynamics", Physical Review Letters **107** (2011) 035003.

[8] G. Y. Antar, G. Counsell, Y. Yu, B. Labombard and P. Devynck, "Universality of intermittent convective transport in the scrape-off layer of magnetically confined devices", Physics of Plasmas **10** (2003) 419.

[9] G. Antar, G. Counsell, J. Ahn, Y. Yang, M. Price, A. Tabasso and A. Kirk, "The poloidal distribution of turbulent fluctuations in the Mega-Ampère Spherical Tokamak", Physics of Plasmas **12** (2005) 032506.

[10] K. J. Zhao, T. Lan, J. Q. Dong, L. W. Yan, W. Y. Hong, C. X. Yu, A. D. Liu, J. Qian, J. Cheng, D. L. Yu, Q. W. Yang, X. T. Ding, Y. Liu and C. H. Pan, "Toroidal Symmetry of the Geodesic Acoustic Mode Zonal Flow in a Tokamak Plasma", Physical Review Letters **96** (2006) 255004.

[11] D. D'Ippolito, J. Myra and S. Zweben, "Convective transport by intermittent blob-filaments: Comparison of theory and experiment", Physics of Plasmas **18** (2011) 060501.

[12] E. Doyle, W. Houlberg, Y. Kamada, V. Mukhovatov, T. Osborne, A. Polevoi, G. Bateman, J. Connor, J. Cordey, T. Fujita, X. Garbet, T. Hahm, L. Horton, A. Hubbard, F. Imbeaux, F. Jenko, J. Kinsey, Y. Kishimoto, J. Li, T. Luce, Y. Martin, M. Ossipenko, V. Parail, A. Peeters, T. Rhodes, J. Rice, C. Roach, V. Rozhansky, F. Ryter, G. Saibene, R. Sartori, A. Sips, J. Snipes, M. Sugihara, E. Synakowski, H. Takenaga, T. Takizuka, K. Thomsen, M. Wade, H. Wilson, I. T. P. T. Group, I. C. Database, M. T. Group, I. Pedestal and E. T. Group, "Chapter 2: Plasma confinement and transport", Nuclear Fusion **47** (2007) S18.

[13] J. Wesson and D. Campbell, *Tokamaks*, International Series of Monographs on Physics, Oxford: OUP Oxford (2011).

[14] W. Horton, "Drift waves and transport", Reviews of Modern Physics **71** (1999) 735.

[15] J. Rost, L. Lin and M. Porkolab, "Development of a synthetic phase contrast imaging diagnostic", Physics of Plasmas **17** (2010) 062506.

[16] Y. K. Kuznetsov, I. C. Nascimento, C. Silva, H. Figueiredo, Z. d. O. Guimarães-Filho, I. L. Caldas, R. M. O. Galvão, J. H. F. Severo, D. L. Toufen, L. Ruchko *et al.*, "Long-distance correlations in TCABR biasing experiments", Nuclear Fusion **52** (2012) 063004.

[17] C. Lechte, S. Niedner and U. Stroth, "Comparison of turbulence measurements and simulations of the low-temperature plasma in the torsatron TJ-K", New Journal of Physics **4** (2002) 34.

[18] B. Kadomtsev and O. Pogutse, "Trapped particles in toroidal magnetic systems", Nuclear Fusion **11** (1971) 67.

[19] W. Horton Jr, R. Estes, H. Kwak and D.-I. Choi, "Toroidal mode coupling effects on drift wave stability", Physics of Fluids **21** (1978) 1366.

[20] S. I. Itoh and K. Itoh, "Confinement Characteristics Part II Theory and Modelling", Journal of Plasma and Fusion Research **67** (1992) 136.

[21] A. Rechester and M. Rosenbluth, "Electron heat transport in a Tokamak with destroyed magnetic surfaces", Physical Review Letters **40** (1978) 38.

[22] P. Diamond, S. Itoh, K. Itoh and T. Hahm, "Zonal flows in plasma — a review", Plasma Physics and Controlled Fusion **47** (2005) R35.

[23] S. Zweben, J. Boedo, O. Grulke, C. Hidalgo, B. LaBombard, R. Maqueda, P. Scarin and J. Terry, "Edge turbulence measurements in toroidal fusion devices", Plasma Physics and Controlled Fusion **49** (2007) S1.

[24] H. Thomsen, M. Endler, J. Bleuel, A. V. Chankin, S. K. Erents and G. F. Matthews, "Parallel correlation measurements in the scrape-off layer of the Joint European Torus", Physics of Plasmas **9** (2002) 1233.

[25] D. Brower, W. Peebles and N. Luhmann Jr, "The spectrum, spatial distribution and scaling of microturbulence in the TEXT tokamak", Nuclear Fusion **27** (1987) 2055.

[26] R. D. Bengtson, D. Winslow and D. Ross, "Fluctuation measurements with two separated probe arrays on the same flux tube", Contributions to Plasma Physics **38** (1998) 104.

[27] D. Winslow, R. D. Bengtson, B. Richards and A. Wootton, "Propagation of a disturbance created by a probe in electron collection", Physics of Plasmas **5** (1998) 752.

[28] R. Durst, R. Fonck, J. Kim, S. Paul, N. Bretz, C. Bush, Z. Chang and R. Hulse, "Observation of a localized transition from edge to core density turbulence in the TFTR tokamak", Physical Review Letters **71** (1993) 3135.

[29] C. P. Ritz, R. V. Bravenec, P. M. Schoch, R. D. Bengtson, J. A. Boedo, J. C. Forster, K. W. Gentle, Y. He, R. L. Hickok, Y. J. Kim, H. Lin, P. E. Phillips, T. L. Rhodes, W. L. Rowan, P. M. Valanju and A. J. Wootton, "Fluctuation-Induced Energy Flux in the Tokamak Edge", Physical Review Letters **62** (1989) 1844.

[30] R. J. Akers, J. W. Ahn, G. Y. Antar, L. C. Appel, D. Applegate, C. Brickley, C. Bunting, P. G. Carolan, C. D. Challis, N. J. Conway, G. F. Counsell, R. O. Dendy, B. Dudson, A. R. Field, A. Kirk, B. Lloyd, H. F. Meyer, A. W. Morris, A. Patel, C. M. Roach, V. Rohzansky, A. Sykes, D. Taylor, M. R. Tournianski, M. Valovic, H. R. Wilson, K. B. Axon, R. J. Buttery, D. Ciric, G. Cunningham, J. Dowling, M. R. Dunstan, S. J. Gee, M. P. Gryaznevich, P. Helander, D. L. Keeling, P. J. Knight, F. Lott, M. J. Loughlin, S. J. Manhood, R. Martin, G. J. McArdle, M. N. Price, K. Stammers, J. Storrs, M. J. Walsh, the MAST and N. Team, "Transport and confinement in the Mega Ampere Spherical Tokamak (MAST) plasma", Plasma Physics and Controlled Fusion **45** (2003) A175.

[31] J. D. Callen, "Drift-Wave Turbulence Effects on Magnetic Structure and Plasma Transport in Tokamaks", Physical Review Letters **39** (1977) 1540.

[32] M. Ono and R. Kaita, "Recent progress on spherical torus research", Physics of Plasmas **22** (2015) 040501.

[33] W. Tang, J. Connor and R. Hastie, "Kinetic-ballooning-mode theory in general geometry", Nuclear Fusion **20** (1980) 1439.

[34] P. Snyder, H. Wilson, J. Ferron, L. Lao, A. Leonard, T. Osborne, A. Turnbull, D. Mossessian, M. Murakami and X. Xu, "Edge localized modes and the pedestal: A model based on coupled peeling–ballooning modes", Physics of Plasmas **9** (2002) 2037.

[35] H. Tojo, "A study of magnetohydrodynamic events accompanying magnetic reconnection in spherical Tokamak plasmas", Ph.D. thesis, The University of Tokyo (2009).

[36] P. Tamain, A. Kirk, E. Nardon, B. Dudson, B. Hnat and the MAST team, "Edge turbulence and flows in the presence of resonant magnetic perturbations on MAST", Plasma Physics and Controlled Fusion **52** (2010) 075017.

[37] T. Edlington, R. Martin and T. Pinfold, "MAST magnetic diagnostics", Review of Scientific Instruments **72** (2001) 421.

[38] A. Sontag, S. Diem, R. Fonck, G. Garstka, E. Unterberg and T. Thorson, "Equilibrium properties at very low aspect ratio in the Pegasus toroidal experiment", Nuclear Fusion **48** (2008) 095006.

[39] W. H. Wang, Y. X. He, Z. Gao, L. Zeng, G. P. Zhang, L. F. Xie, X. Z. Yang, C. H. Feng, L. Wang, Q. Xiao and X. Y. Li, "Edge plasma electrostatic fluctuation and anomalous transport characteristics in the Sino-united spherical tokamak", Plasma Physics and Controlled Fusion **47** (2005) 1.

[40] M. Nagata, T. Kanki, N. Fukumoto and T. Uyama, "The internal magnetic field structures and current density profiles in the Helicity Injected Spherical Torus plasma driven by coaxial helicity injection", Physics of Plasmas **10** (2003) 2932.

[41] M. Bongard, K. Thome, J. Barr, M. Burke, R. Fonck, E. Hinson, A. Redd and D. Schlossberg, "Characterization of peeling modes in a low aspect ratio tokamak", Nuclear Fusion **54** (2014) 114008.

[42] A. Field, R. Akers, C. Michael, S. Saarelma, D. Dunai, Y. Ghim, P. Hill, B. McMillan and C. Roach, "Characterisation of ion-scale turbulence in MAST", EX/P7-01, 24th IAEA Fusion Energy Conference (2012).

[43] M. Nagata, T. Higashi, M. Ishihara, T. Hanao, K. Ito, K. Matumoto, Y. Kikuchi, N. Fukumoto and T. Kanki, "Flow and Magnetic Field Profiles in the HIST Spherical Torus Plasmas Sustained by Double Pulsing Coaxial Helicity Injection", ICC/1-1Rb, 24th IAEA Fusion Energy Conference (2012).

[44] D. Smith, S. Parker, W. Wan, Y. Chen, A. Diallo, B. Dudson, R. Fonck, W. Guttenfelder, G. McKee, S. Kaye, D. Thompson, R. Bell, B. LeBlanc and M. Podesta, "Measurements and simulations of low-wavenumber pedestal turbulence in the National Spherical Torus Experiment", Nuclear Fusion **53** (2013) 113029.

[45] S. Kaye, M. Bell, R. Bell, S. Bernabei, J. Bialek, T. Biewer, W. Blanchard, J. Boedo, C. Bush, M. Carter, W. Choe, N. Crocker, D. Darrow, W. Davis, L. Delgado-Aparicio, S. Diem, J. Ferron, A. Field, J. Foley, E. Fredrickson, D. Gates, T. Gibney, R. Harvey, R. Hatcher, W. Heidbrink, K. Hill, J. Hosea, T. Jarboe, D. Johnson, R. Kaita, C. Kessel, S. Kubota, H. Kugel, J. Lawson, B. LeBlanc, K. Lee, F. Levinton, R. Maingi, J. Manickam, R. Maqueda, R. Marsala, D. Mastrovito, T. Mau, S. Medley, J. Menard, H. Meyer, D. Mikkelsen, D. Mueller, T. Munsat, B. Nelson, C. Neumeyer, N. Nishino, M. Ono, H. Park, W. Park, S. Paul, T. Peebles, M. Peng, C. Phillips, A. Pigarov, R. Pinsker, A. Ram, S. Ramakrishnan, R. Raman, D. Rasmussen, M. Redi, M. Rensink, G. Rewoldt, J. Robinson, P. Roney, A. Roquemore, E. Ruskov, P. Ryan, S. Sabbagh, H. Schneider, C. Skinner, D. Smith, A. Sontag, V. Soukhanovskii, T. Stevenson, D. Stotler, B. Stratton, D. Stutman, D. Swain, E. Synakowski, Y. Takase, G. Taylor, K. Tritz, A. von Halle, M. Wade, R. White, J. Wilgen, M. Williams, J. Wilson, W. Zhu, S. Zweben, R. Akers, P. Beiersdorfer, R. Betti, T. Bigelow, M. Bitter, P. Bonoli, C. Bourdelle, C. Chang, J. Chrzanowski, C. Domier, L. Dudek, P. Efthimion, M. Finkenthal, E. Fredd, G. Fu, A. Glasser, R. Goldston, N. Greenough, L. Grisham, N. Gorelenkov, L. Guazzotto, R. Hawryluk, J. Hogan, W. Houlberg, D. Humphreys, F. Jaeger, M. Kalish, S. Krasheninnikov, L. Lao, J. Lawrence, J. Leuer, D. Liu, N. Luhmann, E. Mazzucato, G. Oliaro, D. Pacella, R. Parsells, M. Schaffer, I. Semenov, K. Shaing, M. Shapiro, K. Shinohara, P. Sichta, X. Tang, R. Vero, D. Walker and W. Wampler, "Progress towards high performance plasmas in the National Spherical Torus Experiment (NSTX)", Nuclear Fusion **45** (2005) S168.

[46] D. R. Smith, R. J. Fonck, G. R. McKee, D. S. Thompson, R. E. Bell, A. Diallo, W. Guttenfelder, S. M. Kaye, B. P. LeBlanc and M. Podesta, "Characterization and parametric dependencies of low wavenumber pedestal turbulence in the National Spherical Torus Experiment", Physics of Plasmas **20** (2013) 055903.

[47] Y. Liu, Y. Tan, O. Pan, R. Ke, W. Wang and Z. Gao, "Design and calibration of high-frequency magnetic probes for the SUNIST spherical tokamak", Review of Scientific Instruments **85** (2014) 11E802.

[48] V. Gusev, S. Aleksandrov and A. Barsukov, "Investigation of Beams and Waves Plasma Interaction in the Globus-M Spherical Tokamak", EXW/P7-08, 23rd IAEA Fusion Energy Conference (2010).

[49] H. Toyama, K. Hanada, H. Totsuka, E. Ishiyama, S. Shiraiwa, S. Duorah, I. Nakajima, M. Ushigome, N. Uetake, K. Tanji, N. Kasuya, Y. Nagashima, K. Yamagishi, A. Ejiri and Y. Takase, "COMPARATIVE STUDIES OF A SPHERICAL TOKAMAK AND A CONVENTIONAL TOKAMAK: MAGNETIC TURBULENCE-INDUCED TRANSPORT", IAEA-CN-69/EXP2/15, Yokohama: 17th IAEA Fusion Energy Conference (1998).

[50] W. Rowan, C. Klepper, C. P. Ritz, R. D. Bengtson, K. Gentle, P. Phillips, T. Rhodes, B. Richards and A. Wootton, "Global particle confinement in the Texas Experimental Tokamak", Nuclear Fusion **27** (1987) 1105.

[51] Y. Shikun, Y. Qingwei, D. Xuantong, C. Rengfang, D. Xuru, H. Keqiang, F. Bo, S. Jun, X. Shulan, C. Jianyong and W. Guangjun, "Edge conditions and turbulent fluctuations in the HL-1 tokamak", Journal of Nuclear Materials **176** (1990) 699.

[52] B. LaBombard, "An interpretation of fluctuation induced transport derived from electrostatic probe measurements", Physics of Plasmas **9** (2002) 1300.

[53] T. Uckan, C. Hidalgo, J. Bell, J. Harris, J. Dunlap, J. Wilgen, C. P. Ritz, T. Rhodes and A. Wootton, "Characteristics of edge plasma turbulence on the ATF torsatron", Physics of Fluids B **3** (1991) 1000.

[54] I. H. Hutchinson, "The connected presheath: One-dimensional models of neighboring objects in magnetized plasmas", Physics of Fluids B **3** (1991) 847.

[55] E. Calderon, C. Hidalgo, M. Pedrosa and C. Silva, "On the interpretation of fluctuation and E× B turbulent transport measured by Langmuir probes in fusion plasmas", Review of Scientific Instruments **75** (2004) 4293.

[56] F. F. Chen and J. P. Chang, *Lecture notes on principles of plasma processing*, Springer Science & Business Media (2012).

[57] H. Amemiya, M. Wada, H. Toyoda, K. Nakamura, A. Ando, K. Uehara, K. ichiro Oyama, O. Sakai and K. Tachibana, "Probe Measurements: Fundamentals to Advanced Applications", Journal of Plasma and Fusion Research **7** (2005) 482.

[58] Y. Tsuji, "2. Correlation and Spectral Analysis (Plasma Turbulence Analysis from the View Point of Fluid Turbulence)", Journal of Plasma and Fusion Research **85** (2009) 620.

[59] C. P. Ritz, E. J. Powers, T. L. Rhodes, R. D. Bengtson, K. W. Gentle, H. Lin, P. E. Phillips, A. J. Wootton, D. L. Brower, N. C. Luhmann, W. A. Peebles, P. M. Schoch and R. L. Hickok, "Advanced plasma fluctuation analysis techniques and their impact on fusion research", Review of Scientific Instruments **59** (1988) 1739.

[60] J. Beall, Y. Kim and E. Powers, "Estimation of wavenumber and frequency spectra using fixed probe pairs", Journal of Applied Physics **53** (1982) 3933.

[61] Y. Takase, A. Ejiri, N. Kasuya, T. Mashiko, S. Shiraiwa, L. Tozawa, T. Akiduki, H. Kasahara, Y. Nagashima, H. Nozato, H. Wada, H. Yamada, T. Yamada and K. Yamagishi, "Initial results from the TST-2 spherical tokamak", Nuclear Fusion **41** (2001) 1543.

[62] Y. Nagashima, S. Inagaki, K. Kamakaki, H. Arakawa, T. Yamada, S. Shinohara, Y. Kawai, M. Yagi, A. Fujisawa, S. I. Itoh, K. Itoh and Y. Takase, "Development of radially movable multichannel Reynolds stress probe system for a cylindrical laboratory plasma", Review of Scientific Instruments **82** (2011) 033503.

[63] S. Zweben, P. Liewer and R. Gould, "Edge plasma transport experiments in the Caltech Tokamak", Journal of Nuclear Materials **111** (1982) 39.

[64] H. Müller, J. Adamek, J. Horacek, C. Ionita, F. Mehlmann, V. Rohde, R. Schrittwieser and A. U. Team, "Towards Fast Measurement of the Electron Temperature in the SOL of ASDEX Upgrade Using Swept Langmuir Probes", Contributions to Plasma Physics **50** (2010) 847.

[65] N. Mahdizadeh, F. Greiner, M. Ramisch, U. Stroth, W. Guttenfelder, C. Lechte and K. Rahbarnia, "Comparison of Langmuir and emissive probes as diagnostics for turbulence studies in the low-temperature plasma of the torsatron TJ-K", Plasma Physics and Controlled Fusion **47** (2005) 569.

[66] M. Sonehara, Y. Nagashima, A. Ejiri, Y. Takase, H. Furui, N. Tsujii, T. Yamaguchi, T. Shinya, H. Togashi, K. Imamura, T. Inada, S. Tsuda, K. Nakamura, K. Takeuchi, H. Homma, S. Yajima, Y. Yoshida and K. Nakamura, "Measurement of Temperature Fluctuation in TST-2 Sprical Tokamak", 19PB-095, Niigata, Japan: Plasma conference 2014 (2014).

[67] Y. Nagashima, A. Ejiri, Y. Takase, M. Sonehara, H. Kakuda, T. Oosako, J. Hiratsuka, O. Watanabe, T. Yamaguchi, H. Kobayashi, T. Wakatsuki, T. Sakamoto, K. Hanashima, T. Ambo, R. Shino and S. Inagaki, "Evaluation of Edge Electron Temperature Fluctuation by the Use of Fast Voltage Scanning Method on TST-2", Plasma and Fusion Research **6** (2011) 2402036.

[68] F. F. Chen, J. D. Evans and D. Arnush, "A floating potential method for measuring ion density", Physics of Plasmas **9** (2002) 1449.

[69] M. Brix, N. Hawkes, A. Boboc, V. Drozdov, S. Sharapov, J.-E. Contributors *et al.*, "Accuracy of EFIT equilibrium reconstruction with internal diagnostic information at JET", Review of Scientific Instruments **79** (2008) 10F325.

[70] P. Snyder, H. Wilson and X. Xu, "Progress in the peeling-ballooning model of edge localized modes: Numerical studies of nonlinear dynamicsa)", Physics of Plasmas **12** (2005) 056115.

[71] J. Stöckel, J. Badalec, I. Duran, M. Hron, J. Horácek, K. Jakubka, L. Kryska, J. Petrzílka, F. Zácek, M. V. P. Heller, Z. A. Brazilio and I. L. Caldas, "Magnetic and electrostatic fluctuations in the CASTOR tokamak", Plasma Physics and Controlled Fusion **41** (1999) A577.

[72] G. Serianni, A. Murari, G. Fiksel, V. Antoni, M. Bagatin, D. Desideri, E. Martines and L. Tramontin, "Magnetic fluctuations and energy transport in RFX", Plasma Physics and Controlled Fusion **43** (2001) 919.

[73] A. Ando, "2.2 Plasma Flow Measurement -Probe Method-", Journal of Plasma and Fusion Research **83** (2007) 169.

[74] F. Chen, *An Indispensable Truth How Fusion Power Can Save the Planet*, New York: Springer (2011).

[75] V. Antoni, "Edge physics in reversed-field pinch and tokamak: similarities and differences", Plasma Physics and Controlled Fusion **39** (1997) B223.

[76] B. LaBombard, R. L. Boivin, M. Greenwald, J. Hughes, B. Lipschultz, D. Mossessian, C. S. Pitcher, J. L. Terry and S. J. Zweben, "Particle transport in the scrape-off layer and its relationship to discharge density limit in Alcator C-Mod", Physics of Plasmas **8** (2001) 2107.

[77] D. Rudakov, J. Boedo, R. Moyer, P. Stangeby, J. Watkins, D. Whyte, L. Zeng, N. Brooks, R. Doerner, T. Evans, M. Fenstermacher, M. Groth, E. Hollmann, S. Krasheninnikov, C. Lasnier, A. Leonard, M. Mahdavi, G. McKee, A. McLean, A. Pigarov, W. Wampler, G. Wang, W. West and C. Wong, "Far SOL transport and main wall plasma interaction in DIII-D", Nuclear Fusion **45** (2005) 1589.

[78] E. Martines, V. Antoni, D. Desideri, G. Serianni and L. Tramontin, "Energy flux driven by electrostatic turbulence in the RFX edge plasma", Nuclear Fusion **39** (1999) 581.

[79] G. Fiksel, R. D. Bengtson, M. Cekic, D. D. Hartog, S. C. Prager, P. Pribyl, J. Sarff, C. Sovinec, M. R. Stoneking, R. J. Taylor, P. W. Terry, G. R. Tynan and A. J. Wootton, "Measurement of magnetic fluctuation-induced heat transport in tokamaks and RFP", Plasma Physics and Controlled Fusion **38** (1996) A213.

[80] J. Boedo, "Edge turbulence and SOL transport in tokamaks", Journal of Nuclear Materials **390** (2009) 29.

[81] S. Zweben and R. Taylor, "Phenomenological comparison of magnetic and electrostatic fluctuations in the Macrotor tokamak", Nuclear Fusion **21** (1981) 193.

[82] D. Graessle, S. Prager and R. Dexter, "Q dependence of magnetic turbulence in a tokamak", Physics of Fluids B **3** (1991) 2626.

[83] H. Furui, Y. Nagashima, Y. Takase, A. Ejiri, H. Kakuda, M. Sonehara, T. Oosako, N. Tsujii, J. Hiratsuka, K. Imamura, T. Inada, K. Nakamura, A. Nakanishi, T. Shinya, H. Togashi, S. Tsuda, T. Wakatsuki and T. Yamaguchi, "Local current density measurement using a Rogowski probe in Tokyo Spherical Tokamak-2", Review of Scientific Instruments **85** (2014) 11D813.